ENERGY CONVERSION USING PHASE TRANSFORMATION IN MULTIFERROIC MATERIALS

A THESIS

SUBMITTED TO THE FACULTY OF THE GRADUATE SCHOOL

OF THE UNIVERSITY OF MINNESOTA

BY

YINTAO SONG

IN PARTIAL FULFILLMENT OF THE REQUIREMENTS

FOR THE DEGREE OF

DOCTOR OF PHILOSOPHY

RICHARD D. JAMES, ADVISOR

THOMAS W. SHIELD, CO-ADVISOR

August, 2013

Acknowledgements

Foremost, I would like to thank my advisor Professor Richard D. James for the continuous support of my Ph.D study. His patient, inspiration, enthusiasm and immense knowledge helped me every time when I was confused in research. He has been a perfect role model of a creative and rigorous researcher. I could not imaging a more joyful or fruitful Ph.D program without having him as the advisor.

I also would like to acknowledge my co-advisor Professor Thomas W. Shield for his professional advices and suggestions on my work throughout the past four years. I would like to thank Professor Chris Leighton for the productive collaboration on magnetic materials. I learned the fundamentals of materials science from two of his courses, without which I can never finish my work. My committee members, Professor Ellad B. Tadmor, Professor Ryan S. Eliott, and Professor Randall H. Victora have earned my gratitude for their helps on my preliminary and final exams, as well as the useful courses I have taken from them.

Last but not least, I would like to thank all the friends I have met while I was pursuing my Ph.D degree, including Yaniv Ganor, Yiming Wu, Xian Chen, Vijay Srivastava, Kanwal Bhatti, Amartya Banerjee, Vivekanand Dabade, Henrik van Lengerich and Xiaochuan Chai. Their kind help in both research and life are gratefully appreciated. I have to thank my old fried Chaoyang Guo, who has been always supportive during the past five years.

Dedication

To my parents

Song, Xiao-Lin (宋霄林) and *Sun, Chu-Xian* (孙初宪).

Abstract

The history of using first order phase transformations to convert heat into other forms of energy stretches back as far as the 1600's, when the first steam engine was invented. This method can be further applied to any first order phase transformation beyond the liquid-vapor systems. Multiferroic materials undergoing phase transformations, during which a ferroic property changes drastically, are promising candidates, especially in the small temperature difference regime. In this thesis I investigate the conversion from heat into electricity by this new method. A family of alloys undergoing martensitic phase transformation with a big change of magnetization is demonstrated to be capable of energy conversion. It is shown by construction of a demonstration that the proposed concept is feasible. Also the idea of using a temperature gradient for this new energy conversion method is examined. The analysis shows that it is possible to convert a temperature gradient to a temperature oscillation by automatically moving the specimen in two conservative force fields: gravity and magnetic field. Quasi-static and finite-time thermodynamic models are developed. Based on the models, the efficiency and power output of this new method is evaluated theoretically, and the directions of design improvement are proposed. The Clausius-Clapeyron relation (the effect of magnetic field on the transformation temperature) is found to be a key thermodynamic relation in this method. The utilization of other types of muliferroic phase-transforming materials is surveyed.

Contents

List of Tables

List of Figures

Chapter 1

Introduction

1.1 Background

Seeking for new methods of generating energy, in particular electricity, that are both renewable and eco-friendly is one of the most urgent environmental challenges for society in 21st century. The feasibility and performance of such methods depend on the energy sources to be utilized, such as nuclear reaction, wind or tidal waves. In all these non-fossil-fuel based energy sources, heat is the most common form of energy that is transferred, because of the following two facts. First, a great portion of energy sources is stored in the form of or is able to be transformed into heat. A nuclear plant, for example, makes use of the heat released during nuclear reactions to generate electricity. Biofuel and natural gas, two of the most promising alternative energy sources so far, use heat as an intermediate form of energy too. Furthermore, a great amount of heat on earth can be obtained from solar- or geothermal energy sources. For instance, the Solar Energy Generating Systems (SEGS) in California generates electricity at the power of 354 MW [1] from concentrated solar radiation. Its core energy conversion facility is a steam engine which converts heat

into electricity. Second, low grade waste heat is a significant and unavoidable by-product of any energy conversion using heat. In the US, 68% of energy, 26.6 quads (1 quad = 1.055×10^{18} J), are lost as waste heat during electricity production in the year 2011 [2]. Using the gasoline price of 4 US dollars per gallon, this amount of energy is worth 0.8 trillion US dollars. In addition to these industrial applications, waste heat is also a common issue in electronic devices, such as home appliances and personal computers, for which managing waste heat is not only for the purpose of improving the efficiency of power consumption but also is needed to keep the devices cool so that they can function properly. While conventional thermoelectric materials appear to be a promising potential solution to this issue, their performance is limited by the currently low figure of merit zT ($zT = \sigma S^2 T/\kappa$, where σ is electric conductivity, S is Seebeck coefficient, κ is thermal conductivity, and T is temperature). At the present time, the only known method of increasing zT requires complex nanostructuring, which is expect to dramatically raise the cost of the resulting thermal electric generators. Therefore, an efficient and powerful method of using heat to generate electricity is crucial for both integrated power system and waste heat management, at both industrial and microelectronic scales.

My thesis concerns the physics and thermodynamics in multiferroic materials undergoing first order solid-solid phase transformation, on which a novel method of converting heat to electricity relies. During such phase transformation, one or more ferroic properties of the material, *e.g.*, electric polarization or magnetization, changes drastically. Then by moving free charges or electromagnetic induction, the heat used to drive the phase transformation is converted into electricity. This energy conversion method has the following three major advantages comparing with others.

The first advantage is that this method provides high power density. The net work

output per cycle, according to the laws of thermodynamics, is a portion of the net heat absorbed by the thermodynamic system, *e.g.* the working material. The coefficient of proportionality is the efficiency. Hence, if two thermodynamic systems have relatively the same efficiency, the one absorbing more net heat per cycle provides more work output per cycle. At the same frequency, that means the higher power output. A phase-transforming material is able to exchange more heat with the environment than a normal, *i.e.* single phase, material. That is because during a first-order phase transformation, a large amount of heat, so-called latent heat, is absorbed or released – depending on whether it is being heated or cooled – by the working material. And because the method discussed here using solid-to-solid first order phase transformation, it potentially provides high power output density.

Steam engines also rely on a first-order phase transformation. But steam engines involve a vapor phase, which necessitates the use of pressure vessels, heat exchangers, turbines and piping. The methods discussed in this thesis have the potential to eliminate this infrastructure. To fully explore this potential, I develop thermodynamic models in this thesis that reveal the relationship between the energy conversion performance and material properties. The results will be used to evaluate the performance of materials currently available, and guide the direction of material search in the future.

The second advantage is related to the durability of the core working materials. In general, phase-transforming materials have shorter fatigue life than non-transforming materials. However, if the crystal structures of both phases satisfy certain compatibility conditions [3, 4], the materials undergoing cyclic phase transformations exhibit high durability. High durability also means low cost. Solid state energy-conversion materials, such as solar cells and conventional thermoelectrics,

typically suffer from the issue of functional degradation. A certain family of materials that will be used in the new energy conversion method have improved resistance to degradation caused by cyclic phase transformations. Such resistance in phase-transforming material is characterized as reversibility. A successful strategy of improving the reversibility of materials undergoing martensitic phase transformation has been theoretically proposed [5, 6] and experimentally confirmed [3, 4, 7]. Here, reversibility is quantified by the size of the hysteresis, and the degradation of latent heat and the migration of transformation temperature under repeated cycling [4]. Following this strategy, reliable materials with desirable functionality can be found. This strategy will be reviewed in detail later in this chapter.

The third advantage is that this method can achieve Carnot efficiency more easily than in single phase materials. The Carnot efficiency is the maximum efficiency of converting heat to other forms of energy, which in general can only be achieved by Carnot cycles. However, it is difficult in single phase materials to use a Carnot cycle to convert heat to other forms of energy in practice. The issue concerns the two isothermal processes in the Carnot cycle. For a single phase material, to achieve an isothermal process, it is necessary to change the pressure or magnetic field, etc., in a specific way during the process, which can be difficult to do in practice. The situation is different for a phase-transforming material. In such a material an isothermal process can be achieved at constant pressure (stress) or magnetic field. This occurs by the release or absorption of latent heat due to changes of the volume fractions of the phases. In this thesis I show that Carnot cycles having isothermal segments at constant external field are possible theoretically. How fast a material can transform nearly isothermally relies on heat transfer issues and on the kinetics of first order phase transformations, which is an actively developing area in thermodynamics, physics, solid mechanics and materials science.

1.2 Martensitic phase transformation and reversibility

Martensitic transformations, named after the German metallurgist Adolf Martens (1850–1914), are diffusionless, solid-to-solid phase transitions from the austenite phase at high temperature to the martensite phase at low temperature. The two phases are characterized by different crystal structures [8–10]. In general, austenite phase has a higher symmetry, *i.e.* a higher order of the point group, than martensite phase. In such cases, the point group of martensite is a subgroup of that of austenite. By Lagrange's theorem in group theory – the order of any subgroup must be a divisor of the order of the original group – the quotient of the orders of the two point groups is the number of martensite variants. Following the notation of continuum mechanics [11], let $\Omega \subset \mathbb{R}^3$ be a reference configuration and $\mathbf{y} : \Omega \to \mathbb{R}^3$ be a deformation with gradient $\nabla \mathbf{y}$. Austenite is often associated to the reference configuration and therefore the deformation gradient describing the austenite phase is the identity matrix $\mathbf{I}$. A particular deformation gradient $\mathbf{F}$ mapping an infinite crystal from austenite to a single variant of martensite can be determined through the Cauchy-Born rule [9]. $\mathbf{F}$ has the polar decomposition $\mathbf{F} = \mathbf{R}_F\mathbf{U}$, for a unique rotation tensor $\mathbf{R}_F \in \mathrm{SO}(3)$ and positive-definite symmetric tensor $\mathbf{U}$. Here, SO(3) is the set of all orthogonal matrices with determinant 1. $\mathbf{U}$ is called the *transformation stretch tensor*.

By the classical argument of thermodynamics, phases are the local minima of a free energy density. The common choice of state variable (independent variable) is the deformation gradient, then by the Galilean invariance, each energy well is a "ring" with SO(3) symmetry in the space of $\mathbb{R}^{3\times 3}$. For example, the set SO(3) is the energy well of austenite, while $\mathrm{SO}(3)\mathbf{U}$ is the energy well corresponding to the aforementioned particular variant. Let N be the number of variants, then $\mathrm{SO}(3)\mathbf{U}_i$ for

$i = 1, \ldots, N$ describe all energy wells for martensite. When only elastic energy is considered, all these N wells have the same free energy density. At a temperature higher (resp. lower) than the transformation temperature, the N martensite wells are higher (resp. lower) than the austenite well. At the transformation temperature, the $N+1$ wells have the same height.

Suppose there is a configuration where the state variable, which is the deformation gradient in this case, takes the value from the lowest energy well everywhere but a measure-zero region in the crystal. When the interfacial energy is neglected, the integrated total elastic energy of this configuration is no less than any other accessible configuration. Without loss of generality, we assign the global minimum of free energy density at the transformation temperature to be zero. Thus, the aforementioned minimum energy configuration actually has zero elastic energy. According to Gibbs [12], the material would like to form a zero-elastic-energy configuration, whenever it is possible. There is no penalty of doing so, if the material is allowed to have a spatially uniform deformation gradient, which is a global minimum. But, this might be an issue if the material has multiple deformation gradients co-existing, *i.e.* microstructure. For example, during martensitic phase transformations, austenite and martensite must co-exist so that the new phase can evolve. In these situations, the material has to divide itself into "domains". If within each domain the deformation gradient takes a global minimum of the bulk energy density, then because the interfaces between them have measure-zero, the integrated total bulk energy is still zero.

But, deformation gradient fields cannot be assigned arbitrarily, *e.g.* because a deformation gradient is a gradient field, the integration of the deformation gradient over a loop must vanish. This fact implies kinematic compatibility across the interfaces. The compatibility condition for a material being divided into two uniformly

deformed domains is that

$$\mathbf{F}_1 - \mathbf{F}_2 = \mathbf{a} \otimes \mathbf{n}, \tag{1.1}$$

where $\mathbf{F}_1$ and $\mathbf{F}_2$ are the deformation gradients in two parts respectively, $\mathbf{a}$ is a non-zero vector and $\mathbf{n}$ is the interface normal between two domains. This equation is called the *rank-one relation*. One immediate conclusion is that, such configuration requires a planar interface between two domains.

Going back to the scenario of martensitic phase transformation, since austenite must be present, we can put $\mathbf{F}_2 = \mathbf{I}$ in the rank-1 relation, and write $\mathbf{F}_1 = \mathbf{RU}$. That is

$$\mathbf{RU} - \mathbf{I} = \mathbf{a} \otimes \mathbf{n}. \tag{1.2}$$

Note that in order to solely satisfy the rank-one relation, $\mathbf{U}$ here is not necessarily one of the martensite variants. But the total elastic energy must be non-zero if $\mathbf{U}$ is not on the wells. Ball and James [13] proved that a solution, $\{\mathbf{R}, \mathbf{a}, \mathbf{n}\}$, to (1.2) exists for a symmetric matrix $\mathbf{U}$ if and only if the middle eigenvalue of $\mathbf{U}$ is unity, denoted $\lambda_2 = 1$. If the $\mathbf{U}$ corresponding to a martensite variant satisfies such condition, austenite and single variant martensite can co-exist and meet at a compatible interface, and the resulting total bulk free energy is zero.

When this compatibility condition is satisfied by the lattice parameters of two phases, the hysteresis of phase transformation is low [14], as the energy barrier for the growth of new phase is reduced, by the formation of a low energy two phase co-existing microstructure during phase evolution. This prediction was mainly derived by the geometrically non-linear theory of martensite [5, 6, 9, 13–15]. By the theory, as λ_2 approaches 1, the hysteresis of phase transformation approaches the minimum value. This prediction has been confirmed repeatedly in experiments [3, 7, 16]. For example, a NiTiCuPd thin film with λ_2 close to 1 exhibits a hysteresis as low as 2 °C

[3], and a NiCoMnSn bulk sample, the one used in the demonstration of the new energy conversion method, with λ_2 close to 1 has a hysteresis as low as 6 °C [16]. Therefore, in this thesis, I always assume low, or even zero, hysteresis in thermodynamic modeling. Yet, finite hysteresis would be a main source of energy loss. This is equivalent to assuming zero rate-independent dissipation or history-independent constitutive laws.

1.3 Ferroic-caloric in martensitic phase transformation

Ferroic properties of materials, such as ferromagnetism, ferroelectricity and ferroelasticity, often change drastically over a narrow temperature range, *i.e.* phase transformations. This change is accompanied by a large change of entropy, which suggests the possibility of converting energy between heat and other forms, *e.g.* magnetostatic, electrostatic and elastostatic energy. The usage of this effect, in the ferromagnetic regime, in refrigeration and electricity generation was demonstrated by Warburg [17] and Tesla [18] (and maybe others) already in 1800's. Their works have latter been named *magnetocaloric effect* and *pyromagnetic generators*, respectively. Later, the analogous concepts for ferroelectricity, *i.e.* *electrocaloric effect* [19–21] and *pyroelectric generators* [22–24], has been risen too. These early works used the second-order phase transitions near the corresponding Curie temperature. Because of the smooth (not sharp) decrease of the ferroic ordering at the Curie temperature, these early methods usually suffer from poor performance, *i.e.* low efficiency and low power output, and therefore have not been exploited commercially.

The thrust of ferroic energy conversion for eco-friendly refrigeration applications was driven by the discovery of the so-called *giant* magneto- and electrocaloric effects [25, 26]. Also, a novel method of electricity generation using giant magnetocaloric materials has been demonstrated by Srivastava *et. al.* [27]. Examples of reviews on

this fascinating class of materials are Refs. [21, 28–32]. These giant ferroic-caloric effects are often associated with martensitic phase transformations, where the ferroic properties and the entropy exhibit discontinuous jumps [5, 16, 33]. During martensitic phase transformation, there is an intrinsic ferroic property having a discontinuous jump, *i.e.* the ferroelastic strain. Inspired by this fact, the concept of (giant) elastocaloric refrigerators [34] and ferroelastic (shape memory) generators [35] has been proposed and demonstrated. Also, martensitic phase transformations can introduce metal-insulator transitions [36], which will be discussed in later chapters.

To sum up, during a multiferroic martensitic phase transformation, the material exchanges heat with the environment through the entropy change, and exchanges magnetostatic, electrostatic or elastostatic energy through the jumps of ferromagnetic, ferroelectric or ferroelastic properties. The interplay between these energy flows results in applications of refrigeration and electricity generation. The goal of my thesis is to explore these novel energy applications, by theoretical evaluation and experimental demonstration.

1.4 Outline of this thesis

The main content of the present thesis is organized into three chapters. In Chapter 2, the concept of energy conversion by multiferroic phase transformation is demonstrated on the Heusler alloy $Ni_{45}Co_5Mn_{40}Sn_{10}$. First, I review the material properties of such alloy: it undergoes a martensitic phase transformation from a martensite that is likely to be anti-ferromagnetic [37] to ferromagnetic austenite. During the transformation, the magnetization under a moderate applied magnetic field increases dramatically. An energy conversion method utilizing this alloy is proposed and demonstrated. The results show that the concept is indeed feasible. However

the efficiency and power output of the demonstration device are not satisfactory for applications. This leads to the study presented in Chapter 3 and 4. Another issue arises from the demonstration is that the current design requires oscillatory ambient temperature, but in reality we often have a temperature gradient/difference instead. The last section of Chapter 2 addresses this issue. I show that by combining a conservative force field, *e.g.* gravity, with the magnetic field, the specimen can be moved in the temperature gradient so that the phase transformation is driven cyclically. The trajectory has to be chosen carefully to avoid equilibrium points inside the mixed field. A brief thermodynamic analysis shows that this technique cannot improve the performance, although the device is self-starting.

After proving the feasibility of the concept, the question naturally arisen is "how much is the efficiency of this energy conversion method?". In Chapter 3, I develop a quasi-static thermodynamic model to estimate the efficiency of this kind of energy conversion system. It is a phenomenological model based on the Gibbs free energy. The free energy functions of martensite and austenite are obtained by integrating Maxwell relations with parameters fitted by experimental data. To examine the model, I compute temperature and field induced phase transformation and compare with experimental observation. The result is satisfactory. Then using these free energy functions, I compute the Clausius-Clapeyron relation and temperature-entropy diagram for the material. Based on them, two kinds of thermodynamic cycles for energy conversion, thermomagnetic Ericsson and thermomagnetic Rankine cycles, are proposed and analyzed. I also compare the efficiency of this new method and that of thermoelectric materials.

The biggest disadvantage of quasi-static models is the lack of ability of calculating power output. Hence, I extend the theory of finite-time thermodynamics in

Chapter 4 so that the power output can be discussed. Under the assumptions of *endoreversibility* and *ideal phase transformation system* (terminology will be explained in Chapter 4), an ODE of electric current is derived. The OED combines the contributions from electromagnetism, thermodynamics and heat transfer. Instead of directly solving the ODE numerically, I solve it analytically after certain simplifications. As a result, I find that the complexity of the multi-physics system collapses to a single dimensionless parameter, which I call the figure of merit of this new energy conversion method. As this parameter approaches infinity, the efficiency approaches the Carnot efficiency, when it is (near) unity, the efficiency reaches the Curzon-Ahlborn limit [38] and the power output is maximized. I also study the power maximization problem. The outcome is a matching condition between the device and the working condition (high and low ambient temperatures) that gives the maximum power output. This result is useful in choosing the ideal device for a given working condition and determining the ideal working condition for a given device.

The last chapter contains a summary of conclusions and future works.

Chapter 2

Ferromagnetic Martensitic Phase Transformation

The first demonstration of energy conversion by multiferroic phase transformation was done on the Heusler alloy $Ni_{45}Co_5Mn_{40}Sn_{10}$ in 2011 [27]. This alloy undergoes a martensitic phase transformation where its magnetic properties changes drastically [16]. In this chapter, I review in detail the demonstration, and explore the feasibility of a self-starting design that converts temperature difference into temperature oscillation. Sections 2.1 to 2.3 are extracted from a paper that has been published in *Advanced Energy Materials* by John Wiley and Sons [27]. My contribution to this work includes: preliminary evaluation of the concept, design of the basic configuration (strength of permanent magnet, aspect ratio of specimen, etc.), dynamic model of the current generated which has been compared to the experimental observation. Overall, this is a collaborative work. In particular, I acknowledge Vijay Srivastava whose contribution mainly includes: characterization of the material, making the actual device and measure the electric signal. Sec. 2.4 is not included in the published paper, so it is all my work.

2.1 Introduction

While the goal of discovering a material that is both strongly ferroelectric and strongly ferromagnetic remains elusive, numerous other interesting multiferroic materials are emerging [16, 39–44]. A particularly fertile area for discovery are crystalline materials having a big first order phase transformation, but with no diffusion [13]. Multiferroic properties like polarization or magnetization are generally sensitive to changes of lattice parameters [5, 39, 43]. In a material that undergoes a phase transformation having an abrupt change of lattice parameters, one can expect the two phases to exhibit diverse electromagnetic properties. The alloy $Ni_{45}Co_5Mn_{40}Sn_{10}$, that is used in energy conversion device described here, is of this type. It has a strongly ferromagnetic austenite phase, with magnetization approaching that of iron, and a nonferromagnetic martensite phase.

Alloys that undergo such martensitic phase transformations are also attractive for energy storage and conversion. Fundamentally, this is owing to the absence of diffusion and other relaxation processes and the presence of a low energy mode of transformation between crystalline lattices, *i.e.*, the passage of many austenite-martensite interfaces. Martensitic transformations are typically quite fast, with speeds of interfaces an appreciable fraction of the speed of sound in the material [45]. With a large change in the lattice parameters, large free energy changes are typical. Partly for these reasons, the highest energy density actuator, that converts heat to mechanical work, is the shape memory alloy NiTi [46], which undergoes a reversible martensitic transformation from a cubic to a monoclinic phase. Numerous emerging devices convert mechanical vibrations into electricity using piezoelectric, ferroelectric, magnetostrictive or ferromagnetic shape memory effects. These rely on quite different physical processes so we do not review them here.

With its low hysteresis and its large and abrupt change in magnetization at transformation, we conjecture that the natural application area for our device is energy conversion at small temperature difference. Cyclic heat engines of this type are necessarily of low efficiency, because the efficiency of all such devices is bounded by the Carnot efficiency $1 - T_{\min}/T_{\max}$, $T_{\min}$ (resp., $T_{\max}$) being the lowest (resp., highest) temperature experienced by any part of the device during the cycle, according to a fundamental theorem of thermodynamics. However, the definition of efficiency, η = (net work done)/(total heat absorbed) during the cycle, expressed in purely economic terms, is typically (energy sold)/(fuel bought). Given that all internal combustion engines waste heat at small temperature difference through cooling, it may be that the standard definition of efficiency is irrelevant. More generally, there are enormous reserves of energy on earth stored at small temperature difference, notably, the $\sim 20^\circ C$ difference between surface ocean temperatures and temperatures just below the thermocline in mid-latitude waters. What is needed in such cases is a more suitable measure of efficiency, consistent with thermodynamics at small temperature difference.

Multiferroic alloys that could be utilized in energy conversion devices must have highly reversible phase transformations [47]. A change of lattice parameters typically implies the presence of stress, notably in the transition layer between phases at the austenite/martensite interface [9]. If this stress is sufficiently large, it can drive the formation of dislocations and other defects that, after sufficiently many cycles of transformation, may lead to widening thermal hysteresis, migration of transformation temperatures, or failure [48–50]. At a macroscopic level such processes are often seen as the competition between phase transformation and crystal plasticity.

The particular alloy $Ni_{45}Co_5Mn_{40}Sn_{10}$ used here was found by implementing a new strategy for improving the reversibility of phase transformations. This can be

expressed [5, 9, 14] as the condition $\lambda_2 = 1$, where λ_2 is the middle eigenvalue of the transformation stretch matrix. When $\lambda_2 = 1$, the stressed transition layer in the austenite/martensite interface disappears [51]. In recent alloy development programs done by combinatorial synthesis methods [3, 7], the thermal hysteresis of phase transformations in NiTiX (X = Pd, Pt, Au) has been shown to drop precipitously from more than 30 °C to less than 6 °C as $\lambda_2 \to 1$. A particularly dramatic example of Zarnetta *et al.* [3] in NiTiCuPd alloys shows a hysteresis near zero* and corresponding improvement of the reversibility of transformation, quantified by the migration of hysteresis loops under repeated transformation, as $\lambda_2 \to 1$. The alloy $Ni_{45}Co_5Mn_{40}Sn_{10}$ ($\lambda_2 = 1.0032$) used here was discovered by this kind of tuning of lattice parameters by systematic change of composition [16]. Having $\lambda_2 = 1$ does not contradict an otherwise large change of lattice parameters, i.e., the other eigenvalues of the stretch matrix can remain far from 1, so the aforementioned abrupt change of electromagnetic properties is possible. In this general alloy system we found a correlation between the large magnetization of austenite and λ_2, with the maximum magnetization occurring near $\lambda_2 = 1$. An understanding of the the origins of this correlation is currently unavailable.

2.2 Characterization of $Ni_{45}Co_5Mn_{40}Sn_{10}$

Figure 2.1 shows the magnetization vs. temperature measured in the alloy. At the applied field of 1 T the phase transformation on heating causes an increase of the magnetization from less than 1.0×10^4 A/m^2(10 emu/cm^3) in the martensite phase to more than 1.1×10^6 A/m^2(1100 emu/cm^3) in the austenite phase. The austenite is

* The size of the thermal hysteresis $A_s - M_f$ in several NiTiCuPd alloys having λ_2 extremely close to 1 is shown to be 0 within the experimental error of measurement of temperature. A_s, A_f, M_s, M_f are defined by the construction shown in Figure 2.1.

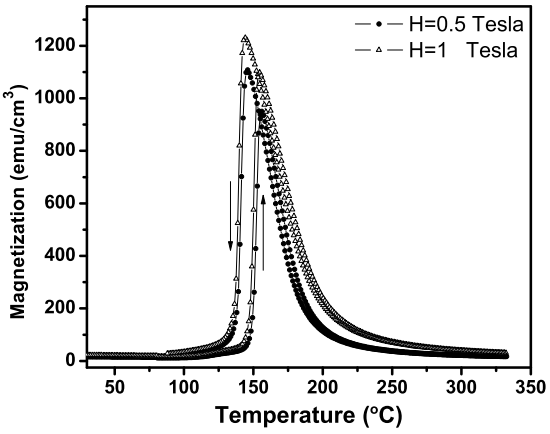

(a) Magnetization vs. temperature under 1 T

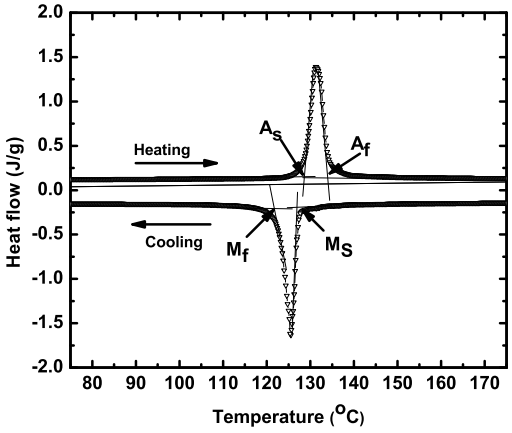

(b) Heat flow vs. temperature

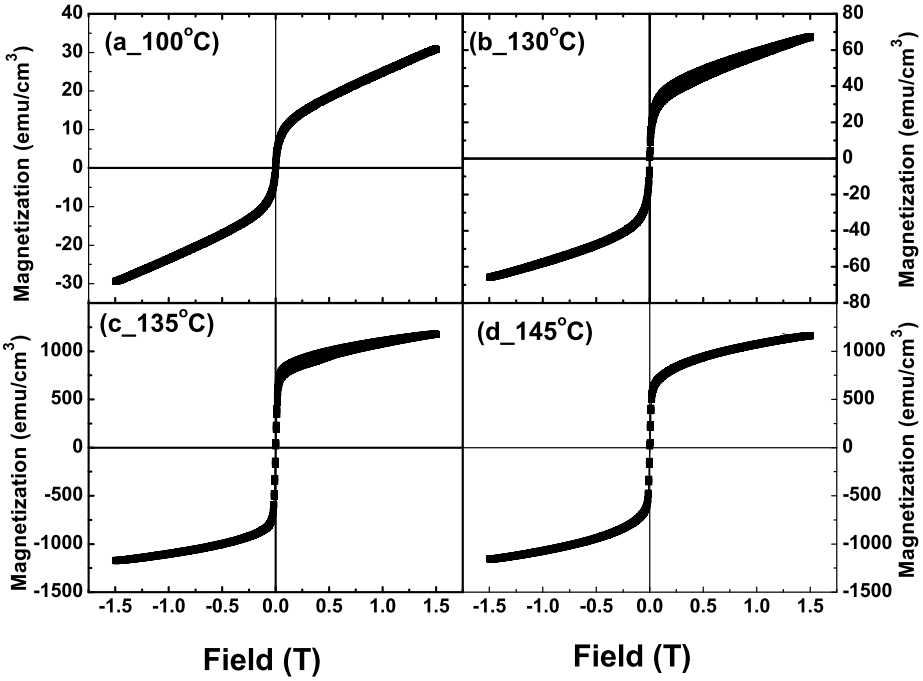

(c) Magnetization vs. applied field at different temperatures (Note the different scales)

Figure 2.1: Relevant properties of the alloy $Ni_{45}Co_5Mn_{40}Sn_{10}$. Reproduced with permission [16] ©2010 American Institute of Physics.

nevertheless magnetically very soft with a susceptibility of $\chi_a = 28.9(2.3\ \text{emu/cm}^3\ \text{Oe})$ measured from the data of Figure 2.1(c)(bottom-left) near $H = 0$. Magnetization vs. temperature at 0.5 T is nearly the same as shown in Figure 2.1(a). Figure 2.1(c)(top-left) suggests an inhomogeneous structure containing a small volume fraction of ferromagnetic particles in an antiferromagnetic matrix. Notice that this high magnetization of austenite occurs even though the transformation temperature $\theta_c = (A_s + M_f)/2$ measured[†] at low field is quite close to the approximate Curie temperature of 167 °C. These temperatures are somewhat high for the design of actual devices, but in this family of alloys, and in martensitic transformations in general, transformation temperatures are extremely sensitive to composition. Further alloy development would be needed to tune both λ_2 and θ_c. The thermal hysteresis measured by calorimetry (Figure 2.1(b)) is $A_s - M_f = 6$ °C and the latent heat is 16.5 J/g. The magnetization curves show zero remanence and coercivity within experimental error. This implies that changes of magnetization contributed negligible loss to the device. This also necessitated the use of a permanent magnet to bias the material, so that, upon heating to austenite, a uniformly magnetized sample was achieved. The loss due to the phase transformation is indicated by the hysteresis loops in several of the measurements. Data presented here were measured by Vijay Srivastava [16].

2.3 Demonstration device and voltage measurements

We show a schematic view of the demonstration in Figure 2.2(a). The specimen is fixed (to prevent movement) near a pole of a permanent bar magnet and is surrounded by a coil. Heat is supplied by an external heat gun. The basic idea is that, upon transformation on heating, the average magnetization **M** is increased in the

[†] see the footnote ∗ on page 15

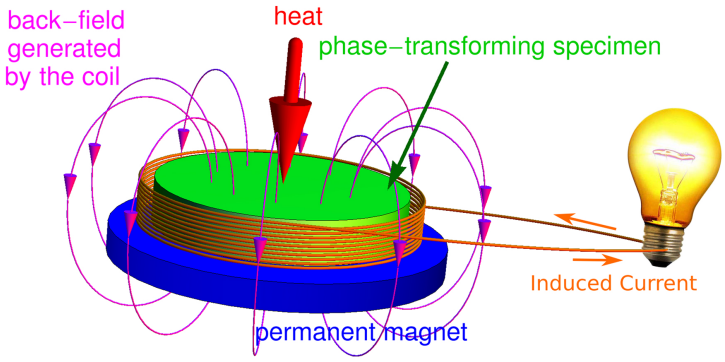

(a) Schematic view (Reproduced with permission [52] ©2013 The Royal Society of Chemistry.)

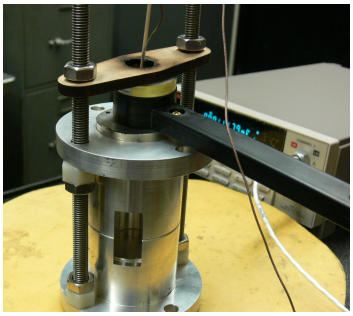

(b) Photo (Reproduced with permission [27] ©2011 John Wiley and Sons.)

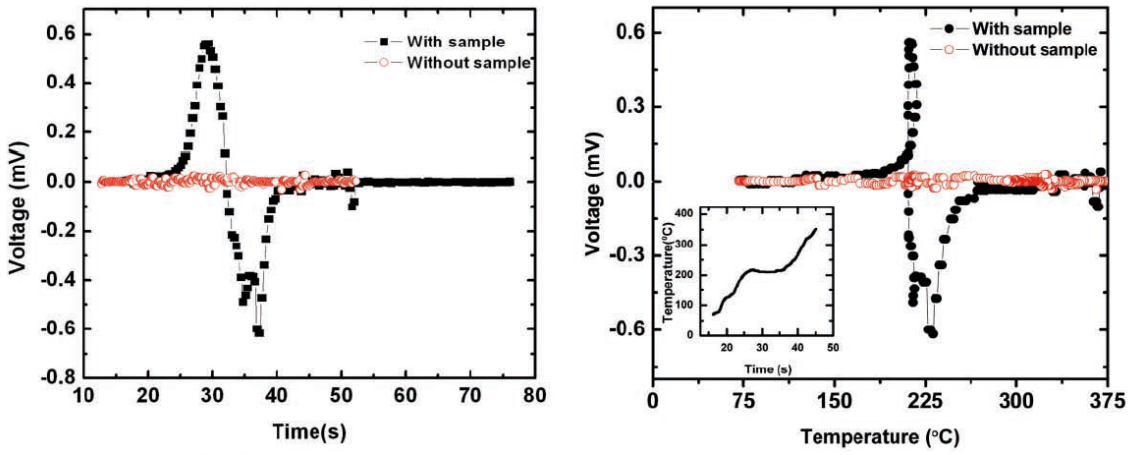

(c) Voltage vs. time and temperature (Reproduced with permission [52] ©2013 The Royal Society of Chemistry.)

Figure 2.2: The demonstration: schematic view, photo, voltage vs. time and voltage vs. temperature measurments.

specimen, giving a substantial component of $d\mathbf{M}/dt$. Demagnetization is prevented by the presence of the nearby permanent magnet. The dipolar relationship between the *magnetization* $\mathbf{M}$, the *magnetic field* $\mathbf{B}$ and *magnetizing force* $\mathbf{H}$,

$$\mathbf{B} = \mu_0(\mathbf{H} + \mathbf{M}), \tag{2.1}$$

then gives a nonzero $d\mathbf{B}/dt$. Above, $\mu_0 = 4\pi \times 10^{-7}$ is the *vacuum permeability*. The precise way in which the magnetization is partitioned between $\mathbf{H}$ and $\mathbf{B}$ is governed by micromagnetic considerations. A consequence of the design is that $d\mathbf{B}/dt \neq 0$ is induced in by the phase transformation. According to Faraday's law, for an arbitrary simple surface $\mathscr{S} \in \mathbb{R}^3$,

$$\oint_{\partial\mathscr{S}} \mathbf{E}\cdot\mathbf{t}\,dx = -\frac{d}{dt}\int_{\mathscr{S}} \mathbf{B}\cdot\mathbf{n}\,d^2x, \tag{2.2}$$

where $\partial\mathscr{S}$ is the edge of $\mathscr{S}$ with tangent unit vector field $\mathbf{t}$, and $\mathbf{n}$ is the normal unit vector field of $\mathscr{S}$. That means that an electric field is created during transformation. The design of the coil is to give a maximal component of E parallel to the wire, thereby driving a current. A potential difference across the coil of opposite polarity is obtained on the reverse phase transformation upon cooling.

We show a picture of the device in Figure 2.2(b). The specimen was arc-melted from elemental materials and, to retain as much mass as possible, it was not cut down to a convenient shape. The surrounding coil consisted of 2000 turns of fine insulated copper wire. A large resistance of 10 kΩ, placed between the ends of the coil, gave a potential difference between its ends during heating. Figure 2.2(c) shows the potential difference across the coil vs. time, and the temperature vs. time (inset of 2.2(c) (right)), measured simultaneously upon heating. The temperature measurement was done with a thermocouple placed below the specimen and therefore

must be considered an approximate representation of the temperature field on the specimen. The measured temperature vs. time is approximately monotone, so in the right subplot of Figure 2.2(c) we eliminate time between these plots and get the graph of voltage vs. temperature. We interpret the plateau in the inset as being due the absorption of latent heat: the lack of strict monotonicity here causes a slight reversal on voltage vs. temperature. By comparison with magnetization vs. temperature shown in the left subplot, we interpret the first rapid rise as due to the phase transformation. We interpret the subsequent sharp decrease as due to the rapid fall of magnetization vs. temperature close to the Curie temperature, as seen in the left subplot of Figure 2.2(c). The cooling curves confirm this interpretation.

Besides the micromagnetic considerations mentioned above, this analysis is too simple in another respect. The current created in the coil itself places a back field on the material, decreasing the overall rate of change of $\mathbf{B}$. A more accurate analysis accounting for this effect leads to a differential equation for the current described later. This back field plays an important role in the work output per cycle, as discussed in the forthcoming thermodynamic analysis.

2.4 On utilizing temperature difference

The design discussed above is based on an oscillating ambient temperature, which could be driven either passively or actively. However, there are many practical situations where neither does the ambient temperature oscillate by itself, nor do we have an effective way of heating and cooling periodically. Instead, there often is an external temperature difference. The natural strategy of utilizing a temperature difference for our energy conversion method is to move the specimen relative to the gradient. Moving the temperature gradient while fixing the specimen can be done

by a method such as active oscillatory heat pipes [53], which in general cost extra work input. In this section, we explore the possibility of moving the specimen in a given external temperature gradient, in particular by using conservative force fields, such as springs and gravity. A particular method of oscillating the active material is analyzed below. The idea is to enable the oscillation without extra work input. The notation in this section applies to this section only.

2.4.1 Magnetostatic energy curves

In this section, we establish the general theoretical framework of energy and power analysis. The calculation is based on the setup shown in Fig. 2.3, where all lengths are normalized by the depth in the third dimension, D.

Two energies are considered: magnetostatic (Zeeman) and gravitational energy. Both are functions of h, once other geometrical parameters are fixed. We denote them $E_{\mathrm{m-m}}(h)$ (martensite), $E_{\mathrm{m-a}}(h)$ (austenite) and $E_{\mathrm{g}}(h)$. Their derivatives with respect to $-h$ are the upwards magnetic force and gravity, $F_{\mathrm{m-a}}(h)$, $F_{\mathrm{m-m}}(h)$ and $F_{\mathrm{g}}(h)$. Note that $E_g(h)$ is an affine function of h, while. We know three properties of $E_{\mathrm{m-m,a}}(h)$: i) it decays at the rate of h^{-1} as $h \to \infty$; ii) it achieves a minimum at $h = 0$, so $F_{\mathrm{m-m,a}}(0) = 0$; iii) $F_{\mathrm{m-m,a}}$ achieves a maximum at the turning point h^* which is near $W/2$. In most cases, the specimen will not fully transform, because the automatic lifting/dropping starts before the transformation is finished. But even for a mixed phase specimen, the magnetostatic energy still has the similar features. We denote the magnetostatic energy of mixed phase specimen with the volume fraction of austenite $\nu \in [0,1]$ $E_{\mathrm{m}}(\nu, h) = \nu E_{\mathrm{m-a}}(h) + (1-\nu)E_{\mathrm{m-m}}(h)$. We draw qualitatively the magnetostatic energy at various volume fractions as shown in Fig. 2.4.

In general, there are three critical positions for each curve, denoted $h_I(\nu)$, $h_{II}(\nu)$ and $h_{III}(\nu)$. h_I and h_{II} are the two equilibrium positions on the curve. While the

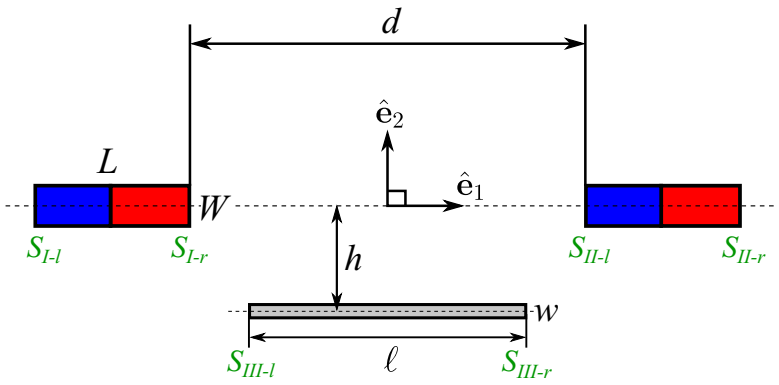

Figure 2.3: Geometric relation between permanent magnets and the specimen. Blue/red bars are permanent magnets. The gray plate is the specimen. $S_{\mathrm{I,II,III-l,r}}$ denote the six important vertical surfaces for the calculation of magnetostatic energy in Sect. 2.4.5.

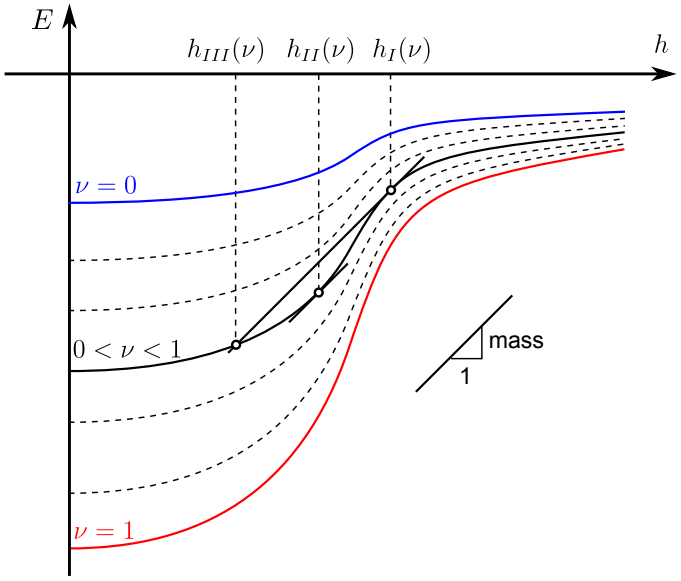

Figure 2.4: Magnetostatic enery with various volume fractions. Blue and red curves correspond to martensite and austenite single phases respectively. The slope of black lines is the gravity.

latter is stable, the former is not. A downwards perturbation ($\delta h > 0$) at h_I causes the specimen to drop to $h \to \infty$. A upwards perturbation ($\delta h < 0$) at h_I causes the specimen to lift to at most $h_{III}(\nu)$, where the velocity reduces to zero and the specimen starts to drop back to h_I. Therefore, the specimen with volume fraction ν can be lifted at the bottom position $\underline{h}$, if $\underline{h} \leqslant h_{III}(\nu)$, and it can drop automatically at the top position $\overline{h}$, if $\overline{h} \leqslant h_{II}(\nu)$.

These critical points do not always exist. When the maximum magnetic force at h^* equals to the gravity, all three critical points collapse to $h_I = h_{II} = h_{III} = h^*$. If the magnetic force is even weaker, those points disappear. Although h_I and h_{II}, if exist, for any volume fraction are positive, h_{III} might be negative if the gravity is weak compare to the magnetic force.

Note that if $\nu_1 < \nu_2$ and all the special h's exist, then $h_I(\nu_1) < h_I(\nu_2)$, $h_{II}(\nu_1) > h_{II}(\nu_2)$, $h_{III}(\nu_1) > h_{III}(\nu_2)$. Since the martensite single phase is supposed to stay at the bottom position and drop *automatically and completely* at the top position, we have $\overline{h}_{\max} = h_{III}(0)$ and $\underline{h}_{\min} = h_I(0)$. If the magnetic force on martensite single phase is so weak that $h_I(0)$ and $h_{III}(0)$ coincide or even do not exist, $\overline{h}_{\max} = \underline{h}_{\min} = h^*$. Since the austenite single phase is supposed to stay at the top position and be lifted automatically at the bottom position, we have $\overline{h}_{\min} = h_{III}(1)$ and $\underline{h}_{\max} = h_I(1)$.

2.4.2 Lifting and dropping processes

A real cycle is actually more complicated than just going back and forth between $\overline{h}$ and $\underline{h}$. Denote the volume fraction of austenite in the specimen $\nu \in [0,1]$. Neglecting the inertia of the phase front, the volume fraction is constant during each lifting/dropping, *i.e.* the phase transformation happens only when the specimen is in touch with the hot or cold plate. The typical lifting and dropping processes are illustrated in Fig. 2.5.

The left subplot of Fig. 2.5 illustrates the typical process of dropping. Suppose the specimen is lifted from point 0 to point 1 in austenite single phase. Then it is cooled and starts to transform, so the effective magentostatic energy curves goes up. When it passes point 2, the top position $\overline{h}$ becomes unstable. So dropping starts. However, when the volume fraction is still close to that of point 2, the specimen cannot drop all the way to the bottom position, because the natural stop position is higher than $\underline{h}$. In other words, there is a local minimum of total potential energy between $\overline{h}$ and $\underline{h}$. For example, if the specimen drops from point 3, it will stop at point 4 and then goes back to point 3. The temperature of the specimen is ratcheted down at each time when it touches the top position (heat sink), until it reaches point 5. Now, the natural stop position is the unstable equilibrium point 6. A downwards perturbation at point 6 or one further ratcheting down of temperature can cause the specimen to drop completely. We denote the volume fraction associated with point 5 and 6 the *dropping volume fraction*, $\underline{\nu}$. This is not the only possible way for a complete dropping. If the bottom position is higher than point 6, for example $\underline{h}'$ in Fig. 2.5, the specimen can have a complete drop before reaching $\underline{\nu}$, say, when $\nu = \underline{\nu}'$ at point 3. In this case, the specimen is lifted immediately when it reaches point 4 instead of staying at the bottom position. Depending on the infinitesimal cooling at point 3 and the infinitesimal heating at point 4, the volume fraction may be trapped at $\underline{\nu}'$, and the trajectory between points 3 and 4 may be dynamically stable. Clearly, we want the first kind of dropping than the second one. The criterion is $\underline{h} \geqslant h_I(\underline{\nu})$, when $\overline{h} = h_{III}(\underline{\nu})$. The latter determines $\underline{\nu}$.

Similar process of lifting is illustrated in the right subplot of Fig. 2.5. After the specimen drops from point 0 to point 1, heating starts. When the volume fraction reaches the so-called *lifting volume fraction* $\overline{\nu}$, lifting starts. It is possible that the specimen is lifted all the way to $\overline{h}$ as the trajectory $2 \rightarrow 3$ shown in Fig. 2.5. But, if

the top position is higher than the height of point 4, $h_{III}(\overline{\nu})$, the initial lifting stops at point 4. Then a ratcheting process similar to the aforementioned dropping takes place, until point 5 is reached. As discussed above, depending on the infinitesimal cooling at point 6 and the infinitesimal heating at point 5, the volume fraction may be trapped at $\overline{\nu}'$, and the trajectory between points 5 and 6 may be dynamically stable. To avoid this trapping, we need $\overline{h} \geqslant h_{III}(\overline{\nu})$, when $\underline{h} = h_I(\overline{\nu})$. The latter determines $\overline{\nu}$.

Clearly, the difference between $\underline{\nu}$ and $\overline{\nu}$ is maximized when $\overline{h} = \overline{h}_{\max}$ and $\underline{h} = \underline{h}_{\max}$. By this choice, if $\overline{h}_{\max} = h_{III}(0)$, $\overline{h} = 1$ and $\underline{h} = 0$, *i.e.* the transformation upon heating and cooling is complete. If, otherwise, the pure martensite is magnetically so weak that $\overline{h}_{\max} = h^*$ as discussed above, $\underline{\nu} > 0$ corresponds to the curve whose steepest slop equals to the gravity, on which points 2, 3 and 5 in the left subplot of Fig. 2.5 coincide. Ratcheting cooling is eliminated. But the transformation upon cooling is incomplete, as $\underline{\nu} \neq 0$. In this case, the dropping volume fraction is determined through

$$F_{\mathrm{m}}(\underline{\nu}, h^*) + F_{\mathrm{g}} = 0, \tag{2.3}$$

where $F_{\mathrm{m}}(\nu, h)$ is the vertical magnetic force on the specimen with the volume fraction ν and at the height h. If (2.3) is satisfied by a $\underline{\nu} \in [0,1]$, we say the dropping and the whole cycle are of *Type-I*, otherwise, *Type-II*. Type-I cycles (dropping) have complete transformation but ratcheting cooling, while Type-II cycles have direct cooling but incomplete transformation. Only when (2.3) is satisfied for $\underline{\nu} = 0$, the resulting cycle is both Type-I and Type-II, which has both complete transformation and direct cooling, and is called a *perfect cycle*. Tuning relative strength of the magnetic force and the gravity, and choosing proper top and bottom positions so that a perfect cycle is enabled, is the goal of geometrical design.

2.4.3 Kinetic energy loss

Each time the specimen is stopped at the top and bottom plates, it has finite velocity before stopping, so a certain amount of kinetic energy is lost. The loss is exactly the value of kinetic energy at the stopping position, as shown in Fig. 2.6. The kinetic energy at each position can be computed by the difference between the changes of E_m and E_g during the lifting/dropping process. It is given by

$$\begin{cases} \overline{E_\mathrm{k}}(h) = \left[E_\mathrm{m}(\overline{\nu}, \underline{h}) - E_\mathrm{m}(\overline{\nu}, h)\right] - \left[E_\mathrm{g}(h) - E_\mathrm{g}(\underline{h})\right], & \text{during lifting,} \\ \underline{E_\mathrm{k}}(h) = \left[E_\mathrm{g}(\overline{h}) - E_\mathrm{g}(h)\right] - \left[E_\mathrm{m}(\underline{\nu}, h) - E_\mathrm{m}(\underline{\nu}, \overline{h})\right], & \text{during dropping.} \end{cases} \tag{2.4}$$

Thus, the kinetic energy losses at the end of lifting and dropping (Fig. 2.6) are respectively $\overline{E_\mathrm{k}}(\overline{h})$ and $\underline{E_\mathrm{k}}(\underline{h})$. The total kinetic energy loss of a cycle is then

$$\mathscr{L}_\mathrm{k} = \overline{E_\mathrm{k}}(\overline{h}) + \underline{E_\mathrm{k}}(\underline{h}) = \Delta E_\mathrm{m}(\underline{h}) - \Delta E_\mathrm{m}(\overline{h}), \tag{2.5}$$

where $\Delta E_\mathrm{m}(h) = E_\mathrm{m}(\overline{\nu}, h) - E_\mathrm{m}(\underline{\nu}, h)$. This shows that $\mathscr{L}_\mathrm{k}$ is independent of the gravitational potential energy. We are lead to the following conclusions:

1. All the magnetic work done by the specimen (to external magnetic field sources) during phase transformation is converted into kinetic energy loss. Electricity is generated only by the back field, just like in the previous demonstration.

2. The back field is generated only when the specimen stays at the top and bottom position, rather than during the lifting or dropping. The power depends strongly on the heat transfer rate at the top and bottom positions.

3. The difference between the field strength at top and bottom positions does not enhance the efficiency, as briefly discussed in Sect. 2.4.4, but it enables the self

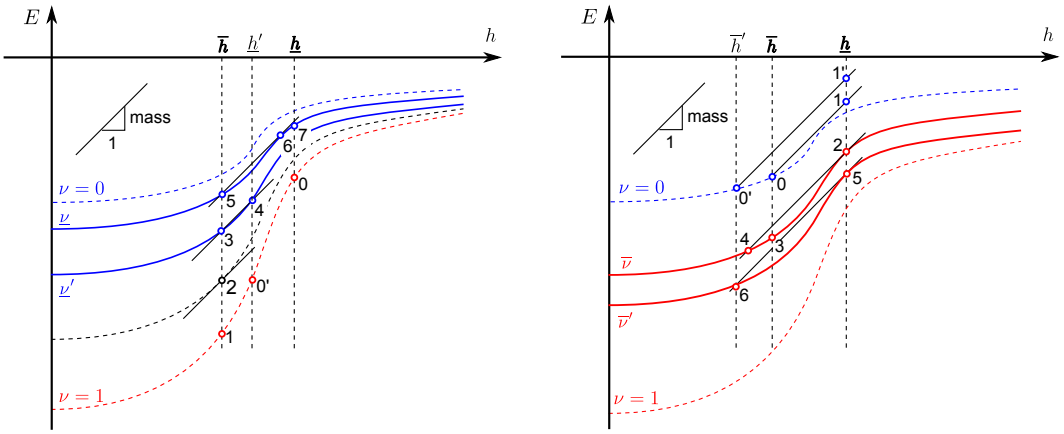

Figure 2.5: Determination of dropping (left) and lifting (right) volume fraction $\underline{\nu}$ and $\overline{\nu}$.

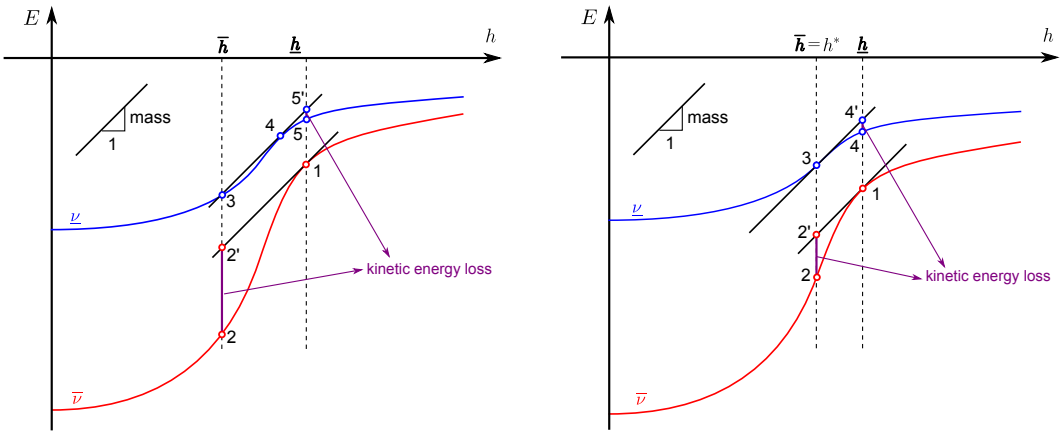

Figure 2.6: Kinetic energy loss for Type-I (left) and Type-II (right) cycles.

starting of the device and converts temperature difference into temperature oscillation.

4. Finally, from kinetic energy we can compute the time required for lifting and dropping, which is given by

$$\bar{t} = \int_{\underline{h}}^{\bar{h}} D\sqrt{\frac{w\ell D^3\rho}{2\overline{E_{\mathrm{k}}}(h)}}\,dh, \quad \underline{t} = \int_{\underline{h}}^{\bar{h}} D\sqrt{\frac{w\ell D^3\rho}{2\underline{E_{\mathrm{k}}}(h)}}\,dh. \tag{2.6}$$

In addition to heat transfer at the top and bottom positions, they can be used to estimate the overall frequency.

2.4.4 A brief discussion on efficiency

Although the change of background field does not directly contribute to electricity generation, it affects the efficiency, as shown in Fig. 2.7.

Fig. 2.7 illustrates the ideal energy conversion cycles in $T-S$ diagram. When the background field is fixed (the left cycle in Fig. 2.7), the reference transformation temperature T_0 can be measured or computed from the Clausius-Clapeyron relation. The back field induced during transformation upon heating and cooling shifts it by δT. The efficiency is given by

$$\eta_0 = \frac{2\delta T}{T_0 + \delta T}. \tag{2.7}$$

If the background field is different for transformation upon heating and cooling, an additional shift of transformation temperature ΔT is added to δT. However, the work output due to the change of background field (the shaded area in the right cycle of Fig. 2.7) all goes into magnetostatic energy. This can be seen by applying the

first law of thermodynamics to the specimen, without the presence of the coil, gives

$$\oint Q\,dt = \oint B_0\dot{M} + mv\dot{v}\,dt. \tag{2.8}$$

We have seen from the discussion in Sect. 2.4.3 that

$$\int_{\mathscr{C}_+\cap\mathscr{C}_-} B_0\dot{M}\,dt + \oint mv\dot{v}\,dt = 0, \tag{2.9}$$

where $\mathscr{C}_\pm$ are the heating and cooling processes in the cycle. So,

$$\oint Q\,dt = \int_{\overline{\mathscr{C}}\cap\underline{\mathscr{C}}} B_0\dot{M}\,dt, \tag{2.10}$$

where $\overline{\mathscr{C}}$ and $\underline{\mathscr{C}}$ are respectively the lifting and dropping processes. That is, the net heat coming from the shift of transformation temperature due to the change of background field is completely converted into the magnetic work, which is unusable in energy conversion. The efficiency of usable work output (electricity) is

$$\eta = \frac{2\delta T}{T_0 + \Delta T + \delta T}. \tag{2.11}$$

So $\eta < \eta_0$, *i.e.* the new design reduces the efficiency. However, in general $T_0 >> \Delta T \gtrsim \delta T$, the difference is negligible, and most of the analysis about the demonstration design, *e.g.* Chapter 3 and 4, is still valid for this new design.

Of course, this estimation is quite crude, because factors such as the unsymmetrical sifts of the transformation temperature about T_0, the dependence of δT on ΔT, and the backfield generated during lifting and dropping associated with fast magnetization and demagnetization are ignored.

2.4.5 Quantitative Results

Magnetostatic energy and magnetic force

In order to calculate the magnetostatic energy without using finite-element-like methods, we make the following assumptions:

1. All length scales are normalized by the depth of objects in the problem, denoted D. The domain of the problem along the third dimension is $x_3 \in [-0.5, 0.5]$.

2. Permanent magnets are uniformly self-magnetized so that the magnetic field at the end surfaces, $S_{\mathrm{I,II-l,r}}$, is $\mathbf{B}_0 = \mu_0 H_0 \hat{\mathbf{e}}_1$.

3. The specimen is uniformly magnetized to $\mathbf{M} = M\hat{\mathbf{e}}_1$. M depends on all lengths in Fig. 2.3 and the volume fraction ν.

Based these assumptions, permanent magnets and the specimen can be modeled by "magnetic charges" on the six end surfaces. The charge densities on those surfaces are

$$\sigma_{\mathrm{I-l}} = \sigma_{\mathrm{II-l}} = -H_0, \quad \sigma_{\mathrm{I-r}} = \sigma_{\mathrm{II-r}} = H_0, \quad \sigma_{\mathrm{III-l}} = -M, \quad \sigma_{\mathrm{III-r}} = M. \tag{2.12}$$

The magnetostatic potential energy generated by the permanent magnets is

$$\phi_0(\mathbf{x}) = \frac{\mu_0 H_0 D}{4\pi}\hat{\phi}(\mathbf{x}), \quad \hat{\phi}(\mathbf{x}) = \int_{S_{\mathrm{I-r}}} \frac{da'}{|\mathbf{x}-\mathbf{x}'|} - \int_{S_{\mathrm{II-l}}} \frac{da'}{|\mathbf{x}-\mathbf{x}'|}. \tag{2.13}$$

We neglect $S_{\mathrm{I-l}}$ and $S_{\mathrm{II-r}}$ because we can have $L \gg W$ or connect them with a flux path so that the surface charges go away.

The background field is given by $-\nabla\phi_0$, so the field at the center of the specimen is

$$\mathbf{B}_{\mathrm{c}} = \frac{\mu_0 H_0}{4\pi}\left(\int_{S_{\mathrm{I-r}}} \frac{\mathbf{x}-\mathbf{x}'}{|\mathbf{x}-\mathbf{x}'|^3}\,da' - \int_{S_{\mathrm{II-l}}} \frac{\mathbf{x}-\mathbf{x}'}{|\mathbf{x}-\mathbf{x}'|^3}\,da'\right)\Bigg|_{\mathbf{x}=(0,-h,0)} = \mu_0 H_0 \hat{B}(h;d,W)\hat{\mathbf{e}}_1, \tag{2.14}$$

where

$$\hat{B}(h;d,W) = \frac{1}{4\pi}\int_{-\frac{1}{2}}^{\frac{1}{2}}\int_{-\frac{W}{2}}^{\frac{W}{2}} \frac{d}{\left(d^2/4+(h+x_2)^2+x_3^2\right)^{3/2}}\,dx_2\,dx_3. \tag{2.15}$$

If parameters are chosen according to the base design (Table 2.1), the distribution of $\hat{B}$ along h is plotted in Fig. 2.8.

Let $\chi_{\mathrm{a,m}}$ be the susceptibility of austenite and martensite so that

$$\mathbf{M}_{\mathrm{a,m}} = \chi_{\mathrm{a,m}}\mathbf{B}_{\mathrm{c}}/\mu_0. \tag{2.16}$$

The Zeeman energy of the uniformly magnetized specimen is

$$E_{\mathrm{m}}(\nu,h) = \int_{S_{\mathrm{III-l}}\cap S_{\mathrm{III-r}}} \phi_0\sigma D^2\,da = \frac{\mu_0 H_0^2 D^3}{4\pi}\chi(\nu)\hat{B}(h)\hat{E}_{\mathrm{m}}(h), \tag{2.17}$$

where $\chi(\nu) = \nu\chi_{\mathrm{a}} + (1-\nu)\chi_{\mathrm{m}}$ and

$$\begin{aligned}\hat{E}_{\mathrm{m}}(h) :=& \hat{E}_{\mathrm{m}}(h;\ell,w,d,W)\\ =& \left(\int_{S_{\mathrm{III-r}}}\int_{S_{\mathrm{I-r}}} + \int_{S_{\mathrm{III-l}}}\int_{S_{\mathrm{II-l}}} - \int_{S_{\mathrm{III-l}}}\int_{S_{\mathrm{I-r}}} - \int_{S_{\mathrm{III-r}}}\int_{S_{\mathrm{II-l}}}\right)\frac{da'\,da}{|\mathbf{x}-\mathbf{x}'|}.\end{aligned} \tag{2.18}$$

Using parameters in Table 2.1, $\hat{E}_{\mathrm{m}}(h)$ and $\hat{E}_{\mathrm{m}}(h)\hat{B}(h)$ are plotted in Fig. 2.9. From the figure, we see that no matter what the ν-dependent coefficient is the function $E_{\mathrm{m}}(\nu,\bullet)$ has the three features mentioned in Sect. 2.4.1.

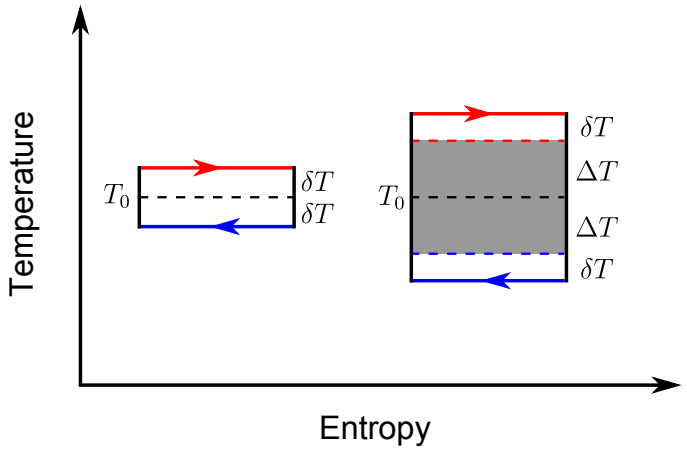

Figure 2.7: Schematics of energy conversion cycles under fixed (left) and changing (right) background magnetic field. T_0 is the transformation temperature under reference magnetic field. ΔT is the shift of transformation temprature due to the change in background field, while δT is the shift due to the back field.

parameter	value	parameter	value
W	0.347	d	1
w	0.1	ℓ	0.9

Table 2.1: Base design: default values of parameters used in calculation.

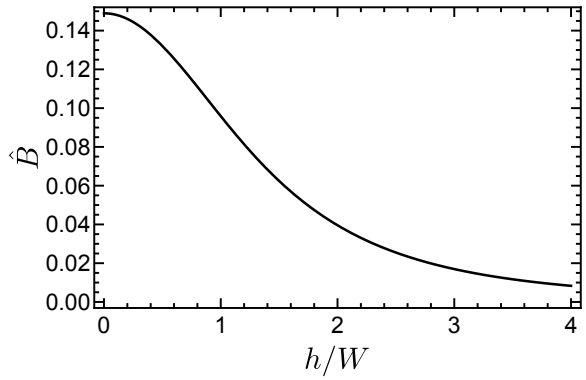

Figure 2.8: Vertical distributions of magnetic field at the center of the specimen.

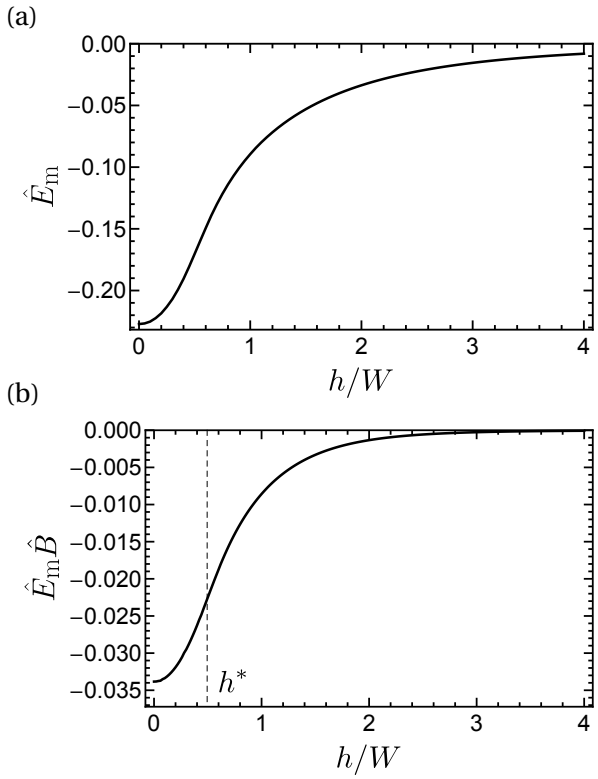

Figure 2.9: Vertical distributions of magnetostatic energy.

The vertical magnetic force (positive direction upwards) exerted on the specimen is

$$F_{\mathrm{m}}(v,h) = \frac{1}{D}\frac{\partial E_{\mathrm{m}}(v,h)}{\partial h} = \frac{\mu_0 H_0^2 D^2}{4\pi}\chi(v)\hat{F}_{\mathrm{m}}(h), \tag{2.19}$$

where $\hat{F}_{\mathrm{m}}(h) = \hat{B}'(h)\hat{E}_{\mathrm{m}}(h) + \hat{B}(h)\hat{E}'_{\mathrm{m}}(h)$ is plotted in Fig. 2.10. From the figure, we see that the maximum magnetic force occurs near $W/2$ as expected.

Top and bottom positions

Two of three critical points for a mangetostatic energy curve can be obtained by locating the intersections between $\hat{F}_{\mathrm{m}}$ in Fig. 2.10 and the (absolute value of) normalized gravity

$$\hat{F}_{\mathrm{g}}(v) := \hat{F}_{\mathrm{g}}(v; w, \ell) = \frac{4\pi w \ell D \rho g}{\mu_0 H_0^2 \chi(v)}. \tag{2.20}$$

Using parameters given in Table 2.2, $\hat{F}_{\mathrm{g}}$ is plotted in Fig. 2.11.

Note that, the normalized gravity for $v = 0$ equals to the maximum $\hat{F}_{\mathrm{m}}$, *i.e.*

$$\hat{F}_{\mathrm{g}}(0) = \max_h \hat{F}_{\mathrm{m}}(h) = \hat{F}_{\mathrm{m}}(h^*). \tag{2.21}$$

In other words, condition (2.3) is satisfied by the martensite single phase. According to our discussion in Sect. 2.4.1, a perfect cycle is possible if we can choose the top and bottom positions to be

$$\overline{h} = h^* = 0.494\,W = 0.171 \text{ cm}, \qquad \underline{h} = h_I(1) = 3.009\,W = 1.044 \text{ cm}. \tag{2.22}$$

The magnetostatic energy curves for two single phases and the top and bottom positions of the perfect cycle are shown in Fig. 2.12. The velocity during lifting and dropping is computed through kinetic energy and plotted in Fig. 2.13. Note that in

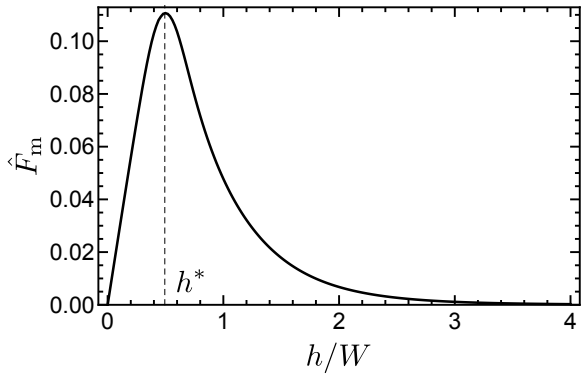

Figure 2.10: Vertical distributions of magnetic force.

parameter	description	value	unit
μ_0	vacuum permeability	$4\pi \times 10^{-7}$	
$\mu_0 H_0$	magnetic field near the pole of magnet	1	T
ρ	mass density	10	g/cm^3
g	gravitational acceleration	9.8	m/s^2
χ_{a}	susceptibility of austenite	$10^6\mu_0$	
χ_{m}	susceptibility of martensite	$10^4\mu_0$	
D	length scale	1	cm

Table 2.2: Parameters used in the calculation.

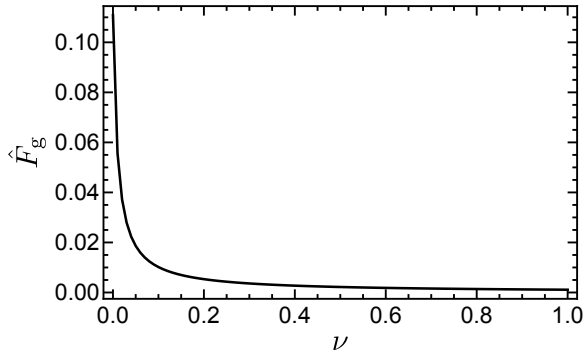

Figure 2.11: Normalized gravity as a function of the volume fraction.

Fig. 2.13 the velocity is not zero at $h/W = 0.5, 3.0$ during dropping and lifting, respectively, because the analysis applies only to the interval of free flight. That is, the impacts that occur at $h/W = 0.5, 3.0$ are treated as perfectly plastic. Time duration as calculated by Eqn. (2.6) is

$$\overline{t} = 0.277 \text{ s}, \qquad \underline{t} = 0.463 \text{ s}, \tag{2.23}$$

for lifting and dropping respectively.

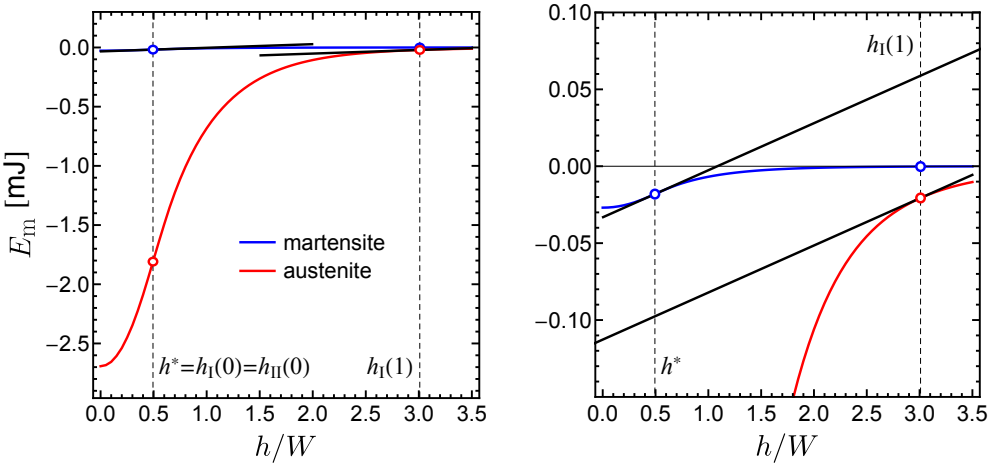

Figure 2.12: Magnetostatic energy for martensite and austenite. The right subplot is a magnification of the left one.

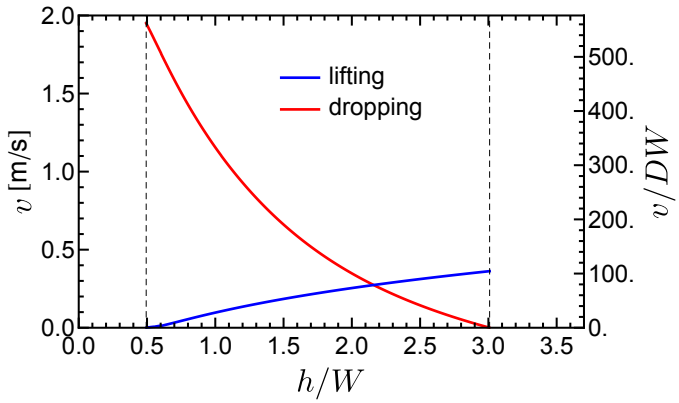

Figure 2.13: Velocity (speed) during lifting and dropping.

Chapter 3

Thermodynamics

3.1 Introduction

In the chapter, I review a thermodynamic model for energy conversion using a first order phase transformation with an abruptly changing magnetization, which was published in Energy & Environmental Science [52]. DSC and SQUID measurements (Sect. 3.2) were done by Kanwal Bhatti, while the fitting and analysis were my work. In the paper, we evaluate explicitly the thermodynamic functions in the theory for the alloy $Ni_{44}Co_6Mn_{40}Sn_{10}$, which has been subject to a detailed characterization study by calorimetry, wide angle x-ray diffraction, SQUID magnetometry and small angle neutron scattering. [37] (The alloy used in Chapter 2 was the nearby alloy $Ni_{45}Co_5Mn_{40}Sn_{10}$.) This off-stoichiometric Heusler alloy undergoes a cubic (space group $Fm\bar{3}m$) to monoclinic (space group $P2_1$, 5M-modulated) martensitic phase transformation at about 390 K, with a sudden change of magnetization. The evidence [37] suggests the martensite is antiferromagnetic with a small fraction of nanoscale spin clusters, which may be retained austenite. The austenite phase of this alloy is ferromagnetic with a magnetization of 8×10^5 A m^{-1} (800 emu cm^{-3}) at 4 T near the

transformation temperature. It is fascinating to add that the nearby alloy $Ni_{45}Co_5Mn_{40}Sn_{10}$ has a measured magnetization in austenite of $1.17\times10^6\,A\,m^{-1}$, but either an increase or a decrease of Co by 1%, substituted for Ni, leads to a significant drop of magnetization. This extreme sensitivity of magnetization to ±1% changes of composition remains unexplained. tent.

It is worth to mention that the model presented here can also be used to analyze magnetic refrigeration based on magnetocaloric effect [54, 55]. Materials showing this effect can use changes in magnetic field to move heat from hot to cold regions. In fact, our prototype material $Ni_{44}Co_6Mn_{40}Sn_{10}$ is close to the Ni-Mn-Sn alloy system which has been identified to have "inverse magnetocaloric effect" [40]. The magnetic refrigeration near room temperature is enabled by the discovery of a so-called giant magnetocaloric effect,[25] which typically occurs in materials having a first order martensitic phase transformation [56, 57]. The magnetic ordering also changes abruptly during such transformations. It can change from strong ferromagnetic martensite to weak ferromagnetic austenite phase [25, 56], weak ferromagnetic martensite to strong ferromagnetic austenite [40], or antiferromagnetic martensite to ferromagnetic austenite [57, 58] as in our prototype alloy. Some magnetocaloric alloys also have low hysteresis [59], although the connection with the alloy development strategy, $\lambda_2 \to 1$, is unknown. Since the thermodynamic cycles of a refrigerator and a heat engine working at the same temperature difference are identical except for the signs of the net work done and heat absorbed, our explicit free energy and our analysis of energy conversion cycles can be easily adopted to magnetic refrigerators.

3.2 Experimental section

The active material for the characterizations was obtained from a polycrystalline ingot (3 g) of $Ni_{44}Co_6Mn_{40}Sn_{10}$ prepared by arc melting the elemental materials Ni (99.999%), Mn (99.98%), Co (99.99%) and Sn (99.99%) under positive pressure of argon. The arc melting furnace was purged three times and a Ti getter was melted prior to melting each sample. To promote homogeneity, the ingot was melted and turned over six times. Conversion from A m^2 kg^{-1} to A m^{-1} was done with a density 8.0 g cm^{-3}. All samples were weighed before and after melting and lost less than 1% by mass. The resulting buttons were homogenized in an evacuated and sealed quartz tube at 900 °C for 24 h, and quenched in room-temperature water. Differential scanning calorimetry (DSC) measurements were done on a Thermal Analyst, calibrated with indium, at a heating and cooling rate of ±10 K/ min between 225 and 475 K. For the DSC measurements, each sample was thinned and finely polished to ensure good thermal contact with the pan. For polycrystalline $Ni_{44}Co_6Mn_{40}Sn_{10}$ (Fig. 3.1) such measurements reveal T_{ms} =398 K, T_{mf} =388 K, T_{as} =382 K, and T_{af} =392 K, where T_{ms}, T_{mf}, T_{as}, and T_{af} are the martensite start, martensite finish, austenite start, and austenite finish temperatures using the standard parameterization of martensitic phase transformation temperatures. The latent heat computed from the graph is L = 13.17 J/g. C_a = 3.65 mJ/K and C_m = 3.90 mJ/K are the average heat capacities for austenite and martensite single phases, respectively. Magnetometry was done in a Quantum Design SQUID magnetometer from 5 to 600 K, in applied magnetic fields from 0.001 to 7 T. For low-field measurements the remnant field profile in the superconducting magnet was measured, and the field at the sample nulled to $\ll 1 \times 10^{-4}$ T. The magnetic properties of $Ni_{44}Co_6Mn_{40}Sn_{10}$ used in the present study are taken from Ref. [37] where more details about experimental methods can

be found.

3.3 Gibbs free energy and Clausius-Clapeyron relation

We now build up a thermodynamic model to describe the first order phase transformation in materials having different magnetic properties in the two phases. According to classical equilibrium thermodynamics, the Gibbs free energy ψ as a function of external magnetic field H and temperature T in a *single phase material* satisfies the Maxwell relations

$$\frac{\partial \psi(H,T)}{\partial H} = -\mu_0 M, \qquad \frac{\partial \psi(H,T)}{\partial T} = -S. \tag{3.1}$$

Integrating the first relation, we have

$$\psi(H,T) = -\mu_0 \int_0^H M(h,T)\,dh + f(T), \tag{3.2}$$

where $f(T)$ is the field-independent component of the free energy, and $M(H,T)$ is the magnetization as a function of external field and temperature. The latter can be obtained from single-phase M-H and M-T measurements reported in the following sections, where the exact method of interpolation is also provided. Based on Eqn. (3.2), we can express entropy and heat capacity as

$$S(H,T) = -\mu_0 \int_0^H \frac{\partial M(h,T)}{\partial T}\,dh + \frac{df(T)}{dT}, \tag{3.3a}$$

$$C(H,T) = T\frac{\partial S(H,T)}{\partial T}. \tag{3.3b}$$

When no field is applied, $\psi(H,T)$ reduces to $f(T)$, and the heat capacity is simply $C(0,T) = T(d^2 f/dT^2)$. Based on DSC data of the alloys of interest (Fig. 3.1), we treat

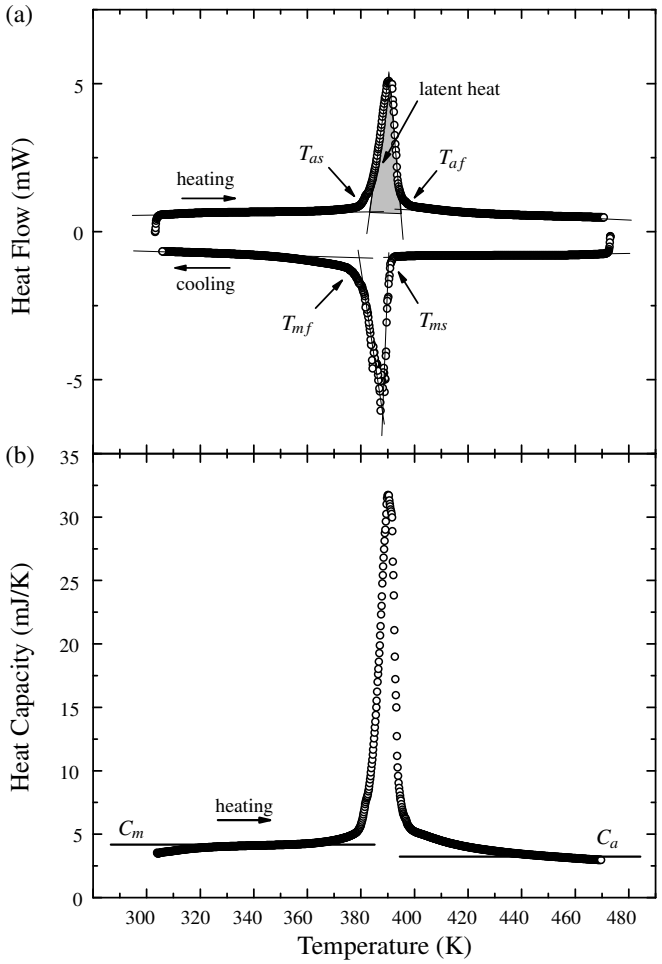

Figure 3.1: (a) Heat flow and (b) heat capacity vs temperature measured by DSC at heating/cooling rate of 10 K/min. T_{ms}, T_{mf}, T_{as}, and T_{af} are the martensite start/finish and austenite start/finish temperatures, respectively. (Reproduced with permission [52] ©2013 The Royal Society of Chemistry.)

the heat capacity of each phase as a constant, denoted by C_m and C_a for martensite and austenite phases, respectively. (Throughout this paper, we use subscripts m or a to denote the thermodynamic functions in martensite or austenite single phase, respectively. Functions without subscripts pertain to the state of the whole specimen, including two-phase mixtures.) The entropy of each phase at zero field then can be obtained by integrating Eqn. (3.3b) over the second argument at $H = 0$ from T_0 to T.

$$S_\mathrm{m}(0,T) = C_\mathrm{m} \ln(T/T_0) + C_1, \tag{3.4a}$$

$$S_\mathrm{a}(0,T) = C_\mathrm{a} \ln(T/T_0) + C_2, \tag{3.4b}$$

where T_0 is the zero-field transformation temperature given by the DSC measurement, and the difference of integration constants $C_1 - C_2$ is evaluated from

$$[S_\mathrm{a}(0,T_0) - S_\mathrm{m}(0,T_0)]\, T_0 = L, \tag{3.5}$$

using the measured zero-field latent heat per unit volume, L. By basic thermodynamic principles excluding the equivocal third law of thermodynamics, only the difference $C_1 - C_2$ has physical meaning in a temperature range bounded away from $T = 0$ K. Without loss of generality, we therefore choose $C_1 = 0$ and $C_2 = L/T_0 - \Delta C$, $\Delta C = C_\mathrm{a} - C_\mathrm{m}$. Then using Eqn. (3.3a), we have the field-independent components of free energy functions

$$f_\mathrm{m}(T) = -C_\mathrm{m}[T_0 - T + T\ln(T/T_0)] + C_3, \tag{3.6a}$$

$$f_\mathrm{a}(T) = -C_\mathrm{a}[T_0 - T + T\ln(T/T_0)] - (L/T_0 - \Delta C)\, T + C_4. \tag{3.6b}$$

$C_3 = -(L - \Delta C T_0)$ and $C_4 = 0$ are determined by the condition $f_\mathrm{a}(T_0) = f_\mathrm{m}(T_0)$. Substituting f's back into Eqn. (3.2) leads to the complete free energy functions, once the magnetization function $M(H,T)$ is obtained. The $M-H$ curve of the alloy at 390 K is plotted in Fig. 3.2. In the figure, we see that the $M-H$ curve can be divided into three regions: low field (< 0.25 T), intermediate field (between 0.25 and 2 T), and high field (> 2 T). In the low field region, a small fraction of the specimen that is ferromagnetic quickly saturates. After saturating the ferromagnetic component, in the intermediate field region, the linear response due to the antiferromagnetic component dominates. Finally, we observe a field induced phase transformation in the high field region. Since the field used in the energy conversion is usually in the intermediate region, for the martensite phase, we use an affine function, $M_\mathrm{m}(H) = a + bH$, to fit its $M-H$ response, with two temperature-independent parameters a and b, as shown in Fig. 3.2. The fitting parameters obtained from the graph are $a = 19748$ A/m and $b = 19.3183$. The total free energy of martensite phase is then $\psi_\mathrm{m}(H,T) = -\mu_0(aH + bH^2/2) + f_m(T)$.

The difference between the linear fitting and the nonlinear data at low fields may contribute a small additive constant ($\sim 10^{-6}$ J cm^{-3}) to the free energy at intermediate fields after integration. As explained in Sect. 3.4, the temperatures T_as and T_af computed from Eqn. (3.11) are characterized by two constant differences ($\Delta\Psi_\mathrm{s}$ and $\Delta\Psi_\mathrm{f}$ in Sect. 3.4) between the Gibbs free energies of austenite and martensite single phases. The constant introduced here by the discrepancy between data and linear fitting in the low field region can be absorbed into those two fitting parameters. We drop it for simplicity.

For the austenite phase, we use the Weiss molecular field theory to derive the magnetization function, $M_\mathrm{a}(H,T)$. Although it is considered more accurate to use the Heisenberg Hamiltonian to describe the interactions between atomic moments,

the Weiss molecular field theory matches experiments very well within the range of temperature and field of interest, as shown below in Fig. 3.3. Furthermore, the simplicity of this model and its capability of reproducing the measured effect of field on transformation temperature is appealing. In molecular field theory, each atom (or molecule in Weiss' terminology, or formula unit in our calculation) in the crystal is assumed to have a magnetic moment, $\mu_{\mathrm{m}}\mathbf{J}$, where μ_{m} is the magnitude and $\mathbf{J}$ is the direction of the moment. The magnetization is then $M = N_{\mathrm{v}}\mu_{\mathrm{m}}\langle J\rangle$, where N_{v} is the number of spins per unit volume. In our fitting, we found two spin sites per formula unit worked well. $\langle J\rangle$ is the mean value of the projection of $\mathbf{J}$ along a certain direction, usually the direction of the external field. Weiss assumed that the interaction between an atom and all the others can be described as an effective internal magnetic field, called the *molecular field*, which is proportional to the magnetization, $\mu_0 H_{\mathrm{m}} = \gamma M$, where γ is the *molecular field constant*. We use the spin-1 Brillouin function, *i.e.* assuming $J = 1$, to compute the mean value of atomic moments

$$\langle J\rangle = B_1\left[\frac{\mu_{\mathrm{m}}(\gamma N_{\mathrm{v}}\mu_{\mathrm{m}}\langle J\rangle + \mu_0 H)}{k_{\mathrm{B}}T}\right], \tag{3.7}$$

where k_B is Boltzmann constant and $B_j(a)$ is the jth Brillouin function

$$B_j(z) = \frac{2j+1}{2j}\coth\left(\frac{2j+1}{2j}z\right) - \frac{1}{2j}\coth\left(\frac{z}{2j}\right). \tag{3.8}$$

The choice $J = 1$ is reasonable (see Ref. [60]) and provides a good fit, but is not supported by knowledge of the detailed magnetic ordering of $Ni_{44}Co_6Mn_{40}Sn_{10}$. As far as we know, the data needed for a quantitative calculation of J for austenite is unavailable for this alloy.

Eqn. (3.7) gives the magnetization in austenite phase as a function of temperature and field through the relation $M = N_v \mu_m \langle J \rangle$. When $H = 0$, it reduces to the spontaneous magnetization as a function of temperature only. The temperature where this spontaneous magnetization vanishes is the Curie temperature. The molecular field constant γ which fits best the data and which is used in following calculation gives a Curie temperature of 439 K. The $M - T$ curve of the same material measured at a low field (10^4 A m^{-1}) shows that the Curie temperature is about 425 K.[37] The discrepancy between fitted and measured values of the Curie temperature suggests that the magnetic property of this material cannot be fully explained by such a single magnetic sublattice $J = 1$ molecular field approximation. The reasons include the interaction between multiple magnetic sublattices (Ni/Co, Mn_1, Mn_2) [61] and the spatial disordering of species in such an off-stoichiometric alloy [61]. In a nutshell, getting a more accurate $M - H$ response in the region where no magnetic measurement of austenite is available, *i.e.* below the transformation temperature, is rather difficult. However, for the purpose of studying small shifts in transformation temperature, as we do in the rest of this paper, this simple fitting model is sufficient. The fitting of austenite magnetization in $Ni_{44}Co_6Mn_{40}Sn_{10}$ is shown in Fig. 3.3. The fitting gives $\mu_m = 4.2\ \mu_B$, which is the same as 8.4 μ_B/f.u., and the molecular field constant is $\gamma = 1573.55$ T m A^{-1}. The result shows excellent agreement with experimental data in both M_a *vs.* T at fixed H and M_a vs H at fixed T curves. The formula unit used here is $Ni_{1.76}Co_{0.24}Mn_{1.60}Sn_{0.40}$. $M_0 = N_v \mu_m$ is the calculated saturation magnetization at $T = 0$ K. The parameters used in the fitting are listed in Table. 3.1.

Overall, the fitting of this data to the function $M_a(H, T)$ is excellent. The small discrepancy occurring at low field (< 0.1 T) is likely to be a result of complex domain interactions arising from the competition of demagnetization and anisotropy energies. The fact that the saturation magnetization at 0 K is much larger than the high

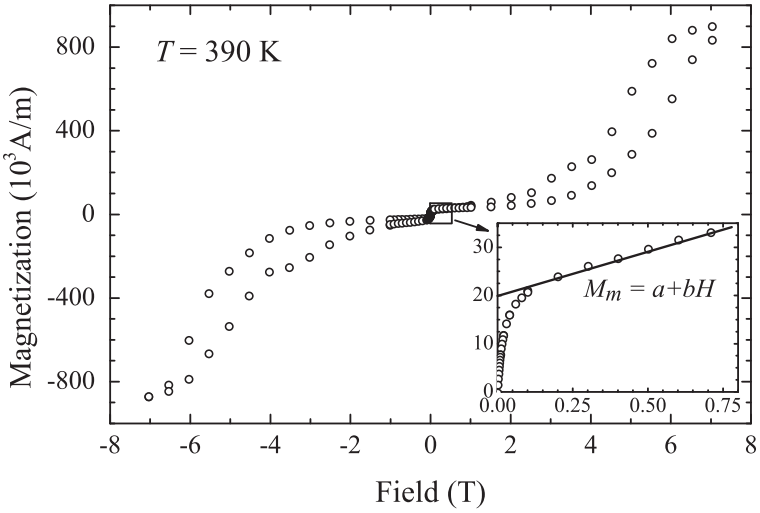

Figure 3.2: Fitting of M-H curve for martensite near the transformation temperature. (Reproduced with permission [52] ©2013 The Royal Society of Chemistry.)

C_m	C_a	L	μ_m	γ	a	b
2.40	2.22	105.36	4.2	1573.55	19748	19.3183

Table 3.1: Parameters used in the fitting of austenite magnetization function, $M_a(H,T)$, in $Ni_{44}Co_6Mn_{40}Sn_{10}$. Heat capacities C_m and C_a (J cm^{-3} K^{-1}), and the latent heat L (J cm^{-3}) are obtained from the DSC measurement (Fig. 3.1). The atomic moment μ_m (μ_B) and the molecular field constant γ (T m A^{-1}) for the austenite phase (Fig. 3.3), and coefficients a (A m^{-1}) and b (dimensionless) for the martensite phase (Fig. 3.2), are fit to the Curie temperature and M-H, M-T curves from the SQUID data. (Reproduced with permission [52] ©2013 The Royal Society of Chemistry.)

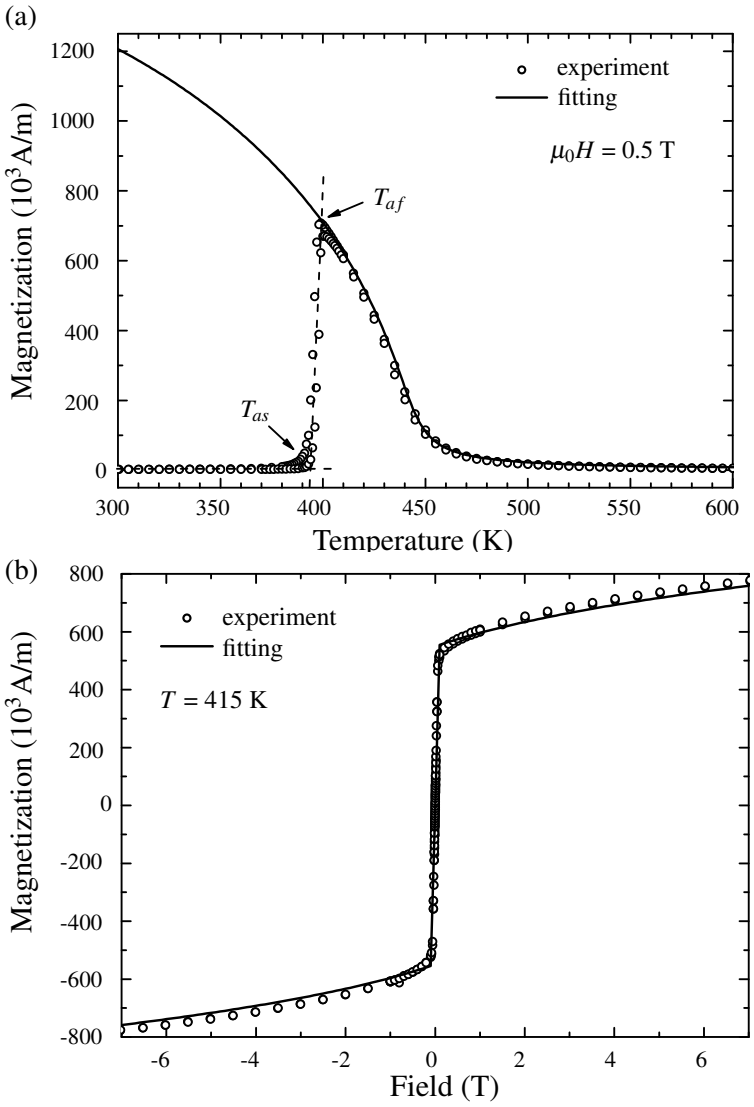

Figure 3.3: Magnetization of austenite phase as a function of (a) temperature and (b) field calculated by Weiss molecular field theory. Open circles are experimental data for both heating and cooling, [37] solid lines are fitted by spin-1 Brillouin function. (Reproduced with permission [52] ©2013 The Royal Society of Chemistry.)

field magnetization on the M_a-H curve in Fig. 3.3b is because 415 K is very close to the Curie temperature, which is about 425 K for this alloy.

In summary, the Gibbs free energy used in the rest of this paper is defined explicitly by

$$\psi(H,T) = -\mu_0 \int_0^H M(h,T)\,dh + f(T), \tag{3.9}$$

where $M = M_a(H,T) = N_v \mu_m \langle J \rangle$ for the austenite phase, with $\langle J \rangle$ given by Eqn. (3.7) and Eqn. (3.8) evaluated with μ_m given in Table 3.1, $M_m(H) = a + bH$ for the martensite phase (a, b in Table 3.1), and f for martensite and austenite, respectively, given by Eqn. (3.6) (C_a, C_m, L in Table 3.1).

To sum up, the theory starts from the assumptions in the form of two Maxwell relations, Eqn. (3.1), and the validity of molecular field approximation. Most of Sect. 3.3 is a theoretical derivation based on these assumptions. Several fitting parameters are needed to evaluate the model. These parameters are obtained from calorimetry data (Fig. 3.1), magnetization curve for martensite (Fig. 3.2) at one temperature, and magnetization vs. field of austenite (Fig. 3.3b) at one temperature, and magnetization vs. temperature at 0.5 T (Fig. 3.3a). The fitted values are listed in Table 3.1. The model is then used to predict other experiments as explained in the next section.

3.4 Temperature and field induced phase transformation

The transformation temperature $T_M = T_M(H)$ as a function of the field H is defined as the temperature where the Gibbs free energy functions of two phases are the same

at the given field (Fig. 3.4a), *i.e.*,

$$\psi_{\mathrm{a}}(H, T_{\mathrm{M}}(H)) = \psi_{\mathrm{m}}(H, T_M(H)). \tag{3.10}$$

The variation of T_{M} with changes of H defines the effect of field on transformation temperature, which is usually quantified by diffentiating Eqn. (3.10) with respect to H and using Eqn. (3.1). The result is a version of the *Clausius-Clapeyron relation* appropriate to magnetic field induced transformation.

Note that the Gibbs free energies in Fig 3.4a are not monotonically decreasing, which means that the entropy is not positive at all temperatures. This can be fixed by adding an affine function of temperature $c_1 T + c_2$ to the Gibbs free energy, which preserves all the results of the paper. In our case c_1 could be chosen to make the entropy positive. We could in fact adjust c_1 and c_2 to satisfy the classical version of the third law of thermodynamics. Since this law is controversial and since the low temperature behavior of $Ni_{44}Co_6Mn_{40}Sn_{10}$ involves a number of unusual effects such as exchange bias, which we have not modeled, we did not do this. The entropy does increase as the temperature increases, which is shown as the concavity of Gibbs free energies.

In order to initiate the transformation from martensite to austenite, the critical temperature T_{as} must be slightly higher than the computed T_{M}, due to the existence of an energy barrier between two equal depth energy wells at T_M. We denote such an energy barrier $\Delta\psi_{\mathrm{s}}$. A similar concept is applied to the temperature T_{af} with a different constant $\Delta\psi_{\mathrm{f}}$. Thus in the model, the temperature T_{as} and T_{af} are determined

through

$$\psi_{\mathrm{a}}(H, T_{\mathrm{as}}) - \psi_{\mathrm{m}}(H, T_{\mathrm{as}}) = \Delta\psi_{\mathrm{s}}, \tag{3.11a}$$

$$\psi_{\mathrm{a}}(H, T_{\mathrm{af}}) - \psi_{\mathrm{m}}(H, T_{\mathrm{af}}) = \Delta\psi_{\mathrm{f}}. \tag{3.11b}$$

The constants on the right hand sides are chosen to give agreement with the measured transformation temperature at 0.5 T. Then it is seen from Fig. 3.4b that the predicted variation of transformation temperature with magnetic field matches experimental data quite well for fields in the range $0 < \mu_0 H < 8$ T in $Ni_{44}Co_6Mn_{40}Sn_{10}$. One remark here is that the zero-field experimental data is obtained from the DSC measurement, while the measured austenite start and finish temperatures, denoted by T_{as} and T_{af} respectively, are interpolated from SQUID data. The measurements from these two methods are slightly different from each other.

By the inspection of the M-T curves in Fig. 3.5a, the transition between two phases is abrupt but not perfectly sharp. An exact quantitative model of this phenomenon would require a detailed study of the mechanism of nucleation [37], and could also involve an assessment of demagnetization and rate effects. However, simple rate-independent models [60] have been successfully used for the quasi-static regime as in our case, and we adopt this simple approach. Therefore, following Ref. [60], we approximate $\partial M(H,T)/\partial T$ during the phase transformation by a Gaussian. Specifically, we assume that the average magnetization of the specimen is given by

$$\begin{aligned} M(H,T) &= \left[1 - \chi\left(\bar{A}, \Delta A, T\right)\right] M_{\mathrm{m}}(H) \\ &\quad + \chi\left(\bar{A}, \Delta A, T\right) M_{\mathrm{a}}(H,T), \end{aligned} \tag{3.12}$$

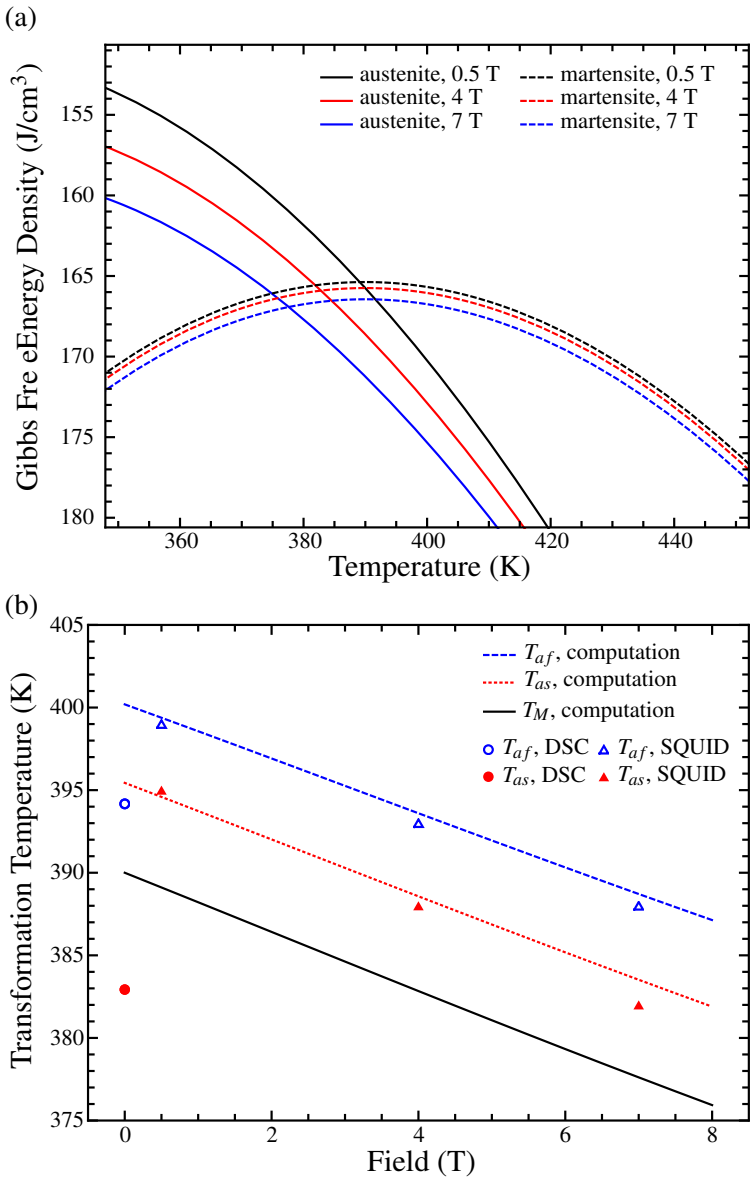

Figure 3.4: (a) Gibbs free energy of both phases expressed as Eqn. (3.2) and (b) the transformation temperature as a function of field computed from Eqn. (3.10). The simulation of $T_{\rm as}$ and $T_{\rm af}$ are computed from Eqn. (3.11) with the energy barriers $\Delta\psi_{\rm s}$ and $\Delta\psi_{\rm f}$ as two fitting parameters. The method of obtaining $T_{\rm as}$ and $T_{\rm af}$ from M-T curves is shown in Fig. 3.3a. For the alloy $Ni_{44}Co_6Mn_{40}Sn_{10}$, $\Delta\psi_{\rm s} = -2.3$ J cm^{-3} and $\Delta\psi_{\rm f} = -4.3$ J cm^{-3}. (Reproduced with permission [52] ©2013 The Royal Society of Chemistry.)

where $\bar{A} = [T_{as}(H) + T_{af}(H)]/2$, $\Delta A = T_{af}(H) - T_{as}(H)$, and

$$\chi(x_c, \Delta, x) = \frac{1}{2}\left[1 + \mathrm{erf}\left(\frac{x - x_c}{\sqrt{2\Delta^2}}\right)\right] \tag{3.13}$$

is the cumulative distribution function of the Gaussian, which might be interpreted as the volume fraction of austenite.

The calculated temperature and field induced phase transformations compared with experimental data are shown in Fig. 3.5. The primary features of these curves are captured reasonably well by our method.

The logic of this section is summarized as following. The Gibbs free energy functions obtained in Sect. 3.3 only apply to single phases. Gibbs criterion of phase transformation, Eqn. (3.10), links them together. So Eqn. (3.10) is the fundamental assumption of this section. Eqn. (3.11) are the hypothesis on A_s and A_f, which is used to link the theoretical phase transformation temperature to the experimentally observed phase transformation temperatures. Knowing A_s and A_f is not enough to predict the exact transition path the specimen between them. Eqn. (3.12) and Eqn. (3.13) are a postulated simple way to model the transition. In summary, all the four equations in this section are assumptions that are made to describe the phase transformation based on the Gibbs free energy obtained earlier. The black line in Fig. 3.4b is calculated from the model (and has not been used in the fitting), while the red and blue lines are used to evaluate a single unknown parameter in Eqn. (3.11). All of the lines in Figs. 3.5a,b are calculated from the model, except the high temperature part of the black line in Fig. 3.5a, which was used in the fitting.

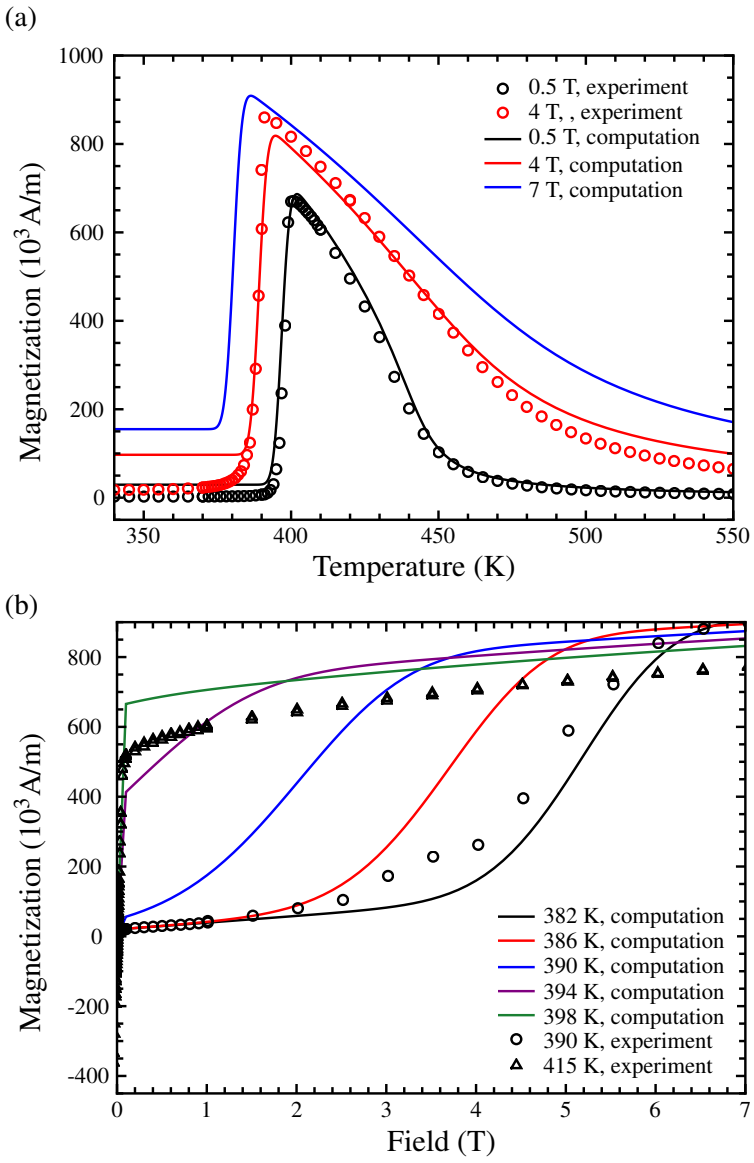

Figure 3.5: Total magnetization of the whole specimen (a) varies with temperature at fixed field, and (b) with field at fixed temperature. Experimental data in these plots were measured for heating. Full data sets including heating and cooling refer to Ref. [37]. (Reproduced with permission [52] ©2013 The Royal Society of Chemistry.)

3.5 Thermodynamic cycles

A thermodynamic cycle consists of a sequence of thermodynamic processes (often quasi-static) of a system in which the state variables return to their original values after one period. During the cycle, heat and mechanical, electrical or magnetic work can be transfered between the system and the environment. Thermodynamic cycles are useful for analyzing energy conversion systems.

The analog of the traditional P-V diagram in the present case is the H-M diagram, which is Fig. 3.5b with the axes interchanged. As in the traditional case when phase transformation is present, a subset of the T-S or H-M diagrams may consist of a *mixed phase region*. This region is defined as the set of values of the state variables for which both phases minimze the Gibbs free energy and therefore the state variables for the individual phases necessarily give the same Gibbs free energy. In the mixed phase region an additional state variable, the volume fraction $0 < \chi < 1$ of, say, austenite, is introduced. In our case the values of the state variables $T, H, S_\mathrm{a}, S_\mathrm{m}, M_\mathrm{a}, M_\mathrm{m}, \chi$ in the mixed phase region are determined by the equilibrium conditions (3.1), the conditions that M and S are extensive variables, $M = (1-\chi)M_\mathrm{m} + \chi M_\mathrm{a}$, $S = (1-\chi)S_\mathrm{m} + \chi S_\mathrm{a}$, and the condition that the Gibbs free energy functions of the two phases are the same, *i.e.*, $\psi_\mathrm{a}(H,T) = \psi_\mathrm{m}(H,T)$. The values of $M_\mathrm{a}, M_\mathrm{m}$ are the corresponding equi-minimizers of the Gibbs free energy. If these conditions cannot be satisfied, or the domains of the free energies φ or ψ exclude certain values of the state variables, then these regions must be excluded from the thermodynamic diagrams. The latter is also important for the evaluation of energy conversion devices.

The measured value $\lambda_2 = 1.0042$ in $Ni_{45}Co_5Mn_{40}Sn_{10}$ corresponding to a thermal hysteresis of 6 K [16] is quite low. In similar systems, by carefully tuning λ_2 even

closer to 1, thermal hysteresis has been reproducibly tuned to less than 1 K in films produced by combinatorial synthesis methods [3], and between 2 and 3 K in arc-melted buttons [6]. We assume that these procedures extend to the kinds of materials discussed here so that the (already low) hysteresis is even further lowered, so we neglect the losses due to hysteresis in the arguments below.

We now describe the thermodynamic diagrams based on the specific free energy evaluated above for $Ni_{44}Co_6Mn_{40}Sn_{10}$. The most useful is the $T-S$ diagram shown in Fig. 3.6, because the area of a loop in the $T-S$ diagram is the net work output, due to the first law of thermodynamics. By direct calculation based on the Gibbs free energy determined in Sect. 3.3, the mixed phase region is represented in this diagram by the region between the dotted curved on the left, corresponding to martensite, and the series of dashed curves on the right for austenite. There are several curves on the right due to the effect of magnetic field H on transformation temperature, *i.e.*, the mixed phase region depends on both independent variables H and T. Overall efficiency is of course affected by how this is recovered, either by induction or some other process. We defer a discussion of the latter to Sect. 3.6.

The mixed phase region, between the dotted and dashed lines in Fig. 3.6, is the most interesting region for energy conversion, because in this region the latent heat can utilized. By definition, the efficiency η of a cycle is W/Q^+, where W is the net work done and Q^+ is the heat absorbed. That is, if the cycle is parameterized by $(T(t), S(t))$, $0 \le t < t_1$,

$$Q^+ = \int_{\mathscr{T}^+} T(t)\dot{S}(t)\, dt, \tag{3.14}$$

where $\mathscr{T}^+$ is the set of times in the interval $[0, t_1)$ for which $\dot{S}(t) > 0$. Carnot cycles are by definition rectangles in the $T-S$ diagram, and these give maximum efficiency $\eta_{\text{Carnot}} = 1 - T_{\min}/T_{\max}$ among all cycles operating between temperatures

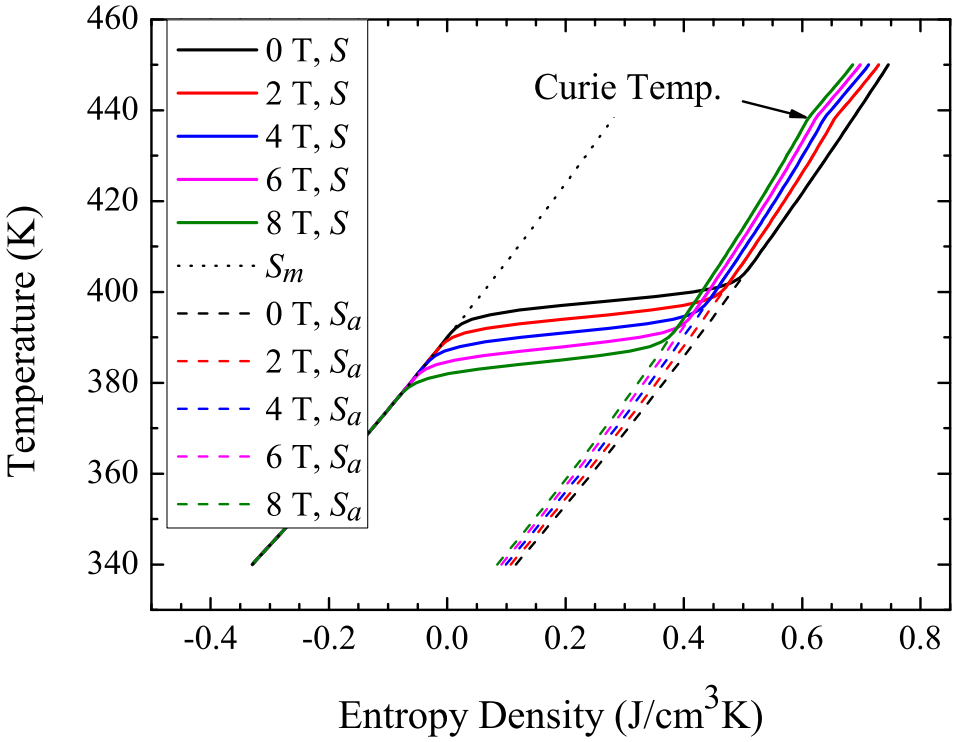

Figure 3.6: Constant field curves in $T - S$ diagram. The dotted line is the entropy of martensite single phase, which is field independent. The dashed lines are the entropy of austenite single phase at different fields, and solid lines are the entropy of the whole specimen containing both phases. (Reproduced with permission [52] ©2013 The Royal Society of Chemistry.)

$T_{\min} < T_{\max}$, by a classical argument. As one can see from Fig. 3.6, the thermomagnetic model given in Sects. 3.2-3.4 admits Carnot cycles of reasonable size in the mixed phase region. Note that Carnot cycles are also possible in the single phase austenite region – the upper right in Fig. 3.6 – although they are so small as to be impractical in our example and also entail exceptionally large changes of the external field over small temperature intervals.

Observe that the predicted constant field lines in the mixed phase region shown in Fig. 3.6 are not perfectly horizontal. Hence Carnot cycles in the mixed phase region require a changing field on the isothermal segments. It may be possible to design devices with this feature, but a simpler approach is to consider cycles having two adiabatic segments alternating with two constant field segments. The resulting cycle is the thermomagnetic analog of the Rankine cycle, and we therefore term this a *thermomagnetic Rankine cycle*. Such a thermomagnetic Rankine cycle is illustrated in Fig. 3.7. Its efficiency can be computed by direct calculation of Q^+ and W using the first law of thermodynamics. Geometrically, the efficiency is the ratio between the area enclosed by the loop $1 \to 2 \to 3 \to 4 \to 1$ and that below the curve $1 \to 2 \to 3$.

Another classical cycle, used widely in jet engines, is the air-standard Ericsson cycle. It also can be adapted to the case of phase transformation and thermomagnetic materials, so we term the resulting cycle the *thermomagnetic Ericsson cycle*. The thermomagnetic Ericsson cycle contains two isothermal segments alternating with two constant field segments. It is defined as follows.

1. Process $1 \to 2$: Heating at constant field. The working material, $Ni_{44}Co_6Mn_{40}Sn_{10}$ in our example, is initially placed in the field H_{min} at the temperature T_{min}, denoted as "1" in Fig. 3.8. It is heated to T_{max} at the constant field. Ideally, the heat for this purpose solely comes from process $3 \to 4$.

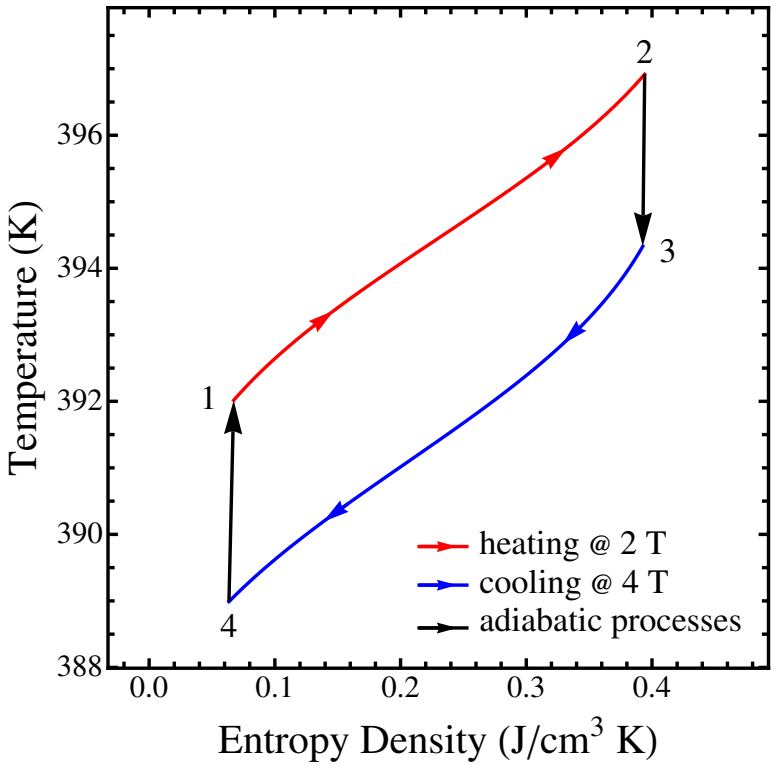

Figure 3.7: A thermomagnetic Rankine cycle. This cycle differs from the thermomagnetic Ericsson cycle by replacing two isothermal processes by adiabatic processes. Two fields are still $H_{\min} = H_0 - \Delta H$ and $H_{\max} = H_0 + \Delta H$, while four temperatures are chosen to be $T_1 = T_{\text{as}}(H_{\max})$ and $T_2 = T_{\max} = T_{\text{af}}(H_{\min})$, according to eqn (3.11), T_3 and $T_4 = T_{\min}$ are the solutions to $S(H_{\min}, T_2) = S(H_{\max}, T_3)$ and $S(H_{\min}, T_1) = S(H_{\max}, T_4)$ respectively. In this drawing, we use $\mu_0 H_0 = 3$ T and $\mu_0 \Delta H = 1$ T. The efficiency is given by the ratio between the area enclosed by the loop $1 \to 2 \to 3 \to 4 \to 1$ and that below the curve $1 \to 2 \to 3$. (Reproduced with permission [52] ©2013 The Royal Society of Chemistry.)

2. Process 2 → 3: Isothermal magnetization. The field is increased to H_{max} without change of temperature. Heat is absorbed during this process.

3. Process 3 → 4: Cooling at constant field. The working material is actively cooled to the temperature T_{min} at the constant field H_{max}. Heat is emitted during this process. Ideally, this heat is completely used to heat the material in the process 1 → 2.

4. Process 4 → 1: Isothermal demagnetization. The field is decreased to H_{min} isothermally, returning the working material to state 1.

An attractive feature of the thermomagnetic Ericsson cycle, as in the ordinary Ericsson cycle, is that if dissipative processes are neglected, the Carnot efficiency is achieved. This is achieved by using, and only using, the heat emitted in process 3 → 4 as the supply for the heating process 1 → 2, so that the heat-exchange with the external environment is no longer required during either process 1 → 2 or 3 → 4. This technique is called "regeneration". The thermomagnetic model given in Sects. 3.2-3.4 admits these ideal thermomagnetic Ericsson cycles. To see this, the material properties have to be such that during the constant field heating 1 → 2 the heat absorbed has to be equal to the heat emitted during 3 → 4, and, at the same time, these segments must begin and end on the same isothermal segments. This is possible according to the following argument. Referring to Fig. 3.8, consider parameterizing the constant field segments 1 → 2 and 4 → 3 by functions $S_{12}(T)$ and $S_{43}(T)$ using T as a parameter. These sigmoidal curves have the property that there is a temperature T_s such that $dS_{12}/dT < dS_{43}/dT$ for $T < T_s$ and $dS_{12}/dT > dS_{43}/dT$ for $T > T_s$. Thus, by the intermediate value theorem, there are values $T_{\min} < T_s < T_{\max}$ such that

$$\int_{T_{\min}}^{T_{\max}} T\frac{dS_{12}}{dT}\,dT = \int_{T_{\min}}^{T_{\max}} T\frac{dS_{43}}{dT}\,dT. \tag{3.15}$$

This is the equality of heats in $1 \rightarrow 2$ and $4 \rightarrow 3$. In fact, it is seen that over a broad range of temperatures in the mixed phase region, $T_{\min} < T_s$ can be assigned and then $T_{\max}$ can be determined such that Eqn. (3.15) holds. Fig. 3.8 shows an example of a thermomagnetic Ericsson cycle where Eqn. (3.15) has been satisfied by a simple numerical procedure.

There are numerous potential device designs utilizing back-to-back plates of active material, together with suitable flux paths that could be used to approximate the conditions of either thermomagnetic Carnot or Ericsson cycles. The switching of the field can also be integrated as part of the device. For example, in the demonstration [27] the current produced in the surrounding coil exerted a back-field on the specimen, which had the effect of altering the field.

The maximum efficiency for conventional thermoelectric materials is given by the formula [62, 63]

$$\eta_{\text{te}} = \left(1 - \frac{T_{\min}}{T_{\max}}\right) \frac{\sqrt{1 + z\overline{T}} - 1}{\sqrt{1 + z\overline{T}} + T_{\min}/T_{\max}}, \tag{3.16}$$

where $\overline{T} = (T_{\min} + T_{\max})/2$, and $zT = \sigma S^2/\kappa$ is the figure of merit of the material at temperature T. Here, S is the temperature-dependent Seebeck coefficient, σ is the electrical conductivity, and κ is the thermal conductivity. Here it is important to note that for thermoelectrics there are two figures of merit in common use, zT and ZT. The former refers to the material alone, as can be seen from its definition, while the latter is for the whole device: for whole devices, ZT is in fact typically calculated from Eqn. (3.16) (with of course zT replaced by ZT) and the measured efficiency of the device (see *e.g.* Ref. [63], p. 112, box 4).

Since our predictions above refer to material rather than device, we compare the efficiency of energy conversion of aforementioned cycles with the thermoelectric

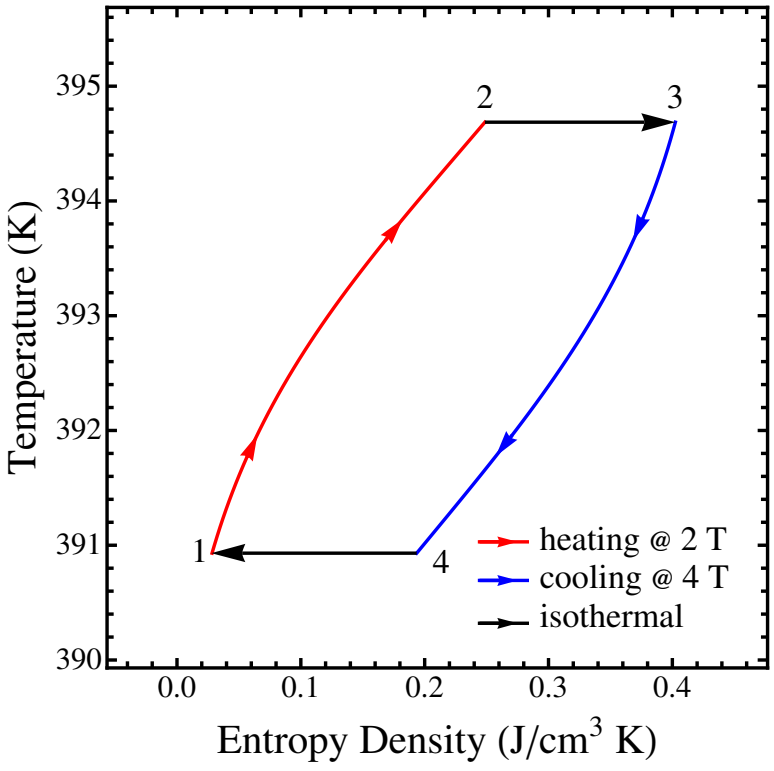

p]

Figure 3.8: A thermomagnetic Ericsson cycle. The cycle contains a constant field heating (red arrowed line) from T_{min} to T_{max} at H_{min}, a constant field cooling (blue arrowed line) from T_{max} to T_{min} at H_{max}, and two isothermal processes (black arrowed lines) switching between two fields isothermally. Two fields are given by $H_{\text{min}} = H_0 - \Delta H$ and $H_{\text{max}} = H_0 + \Delta H$, while two working temperatures are $T_{\text{min, max}} = [T_{\text{as}}(H_{\text{min}}) + T_{\text{af}}(H_{\text{max}})]/2 \pm \delta T$, according to Eqn. (3.11), and δT is chosen to satisfy Eqn. (3.15). In this drawing, we use $\mu_0 H_0 = 3$ T and $\mu_0 \Delta H = 1$ T. The efficiency is given by the ratio between the area enclosed by the loop $1 \to 2 \to 3 \to 4 \to 1$ and that below the curve $1 \to 2 \to 3$. (Reproduced with permission [52] ©2013 The Royal Society of Chemistry.)

efficiency η_{te} based on the material figure of merit zT and the working temperature near the transformation temperature of $Ni_{44}Co_6Mn_{40}Sn_{10}$. The best currently available thermoelectric materials at $\bar{T} = 140$ °C have $zT \approx 1$ (n-type Bi_2Te_3 paired with p-type Sb_2Te_3). In 2008, a hot pressed nanocrystalline powder of BiSbTe having $zT = 1.4$ near 100 °C was reported [64]. Below we use both $zT = 1.0$ and $zT = 1.4$ in our comparisons.

We compare the efficiency of thermomagnetic Ericsson, Rankine and Carnot cycles with that of a thermoelectric having the figure of merit $zT = 1.0, 1.4$ in Fig. 3.9. The thermomagnetic cycles are all assumed to be working at the temperature difference given by the difference between two fields, ΔH, in Fig. 3.9. The efficiency of thermomagnetic Ericsson cycles are computed without assuming regeneration, as then they recover the Carnot efficiency. Excluding thermoelectric generators using radioisotopes, commercial thermoelectric generators generally operate in the range under $\Delta T = 100$ K. For these, the comparison in Fig. 9 shows a competitive efficiency by this new energy conversion method.

Another noteworthy feature of the efficiency, especially for thermomagnetic Rankine cycles, is that as ΔH increases, the efficiency increases. What's more, for a Rankine cycle, the efficiency approaches to the Carnot efficiency as ΔH increases. However, a ΔH larger than 2 T is impractical in most cases. An alternative strategy is to use a material with a strong effect of field on transformation temperature, so that the same ΔH corresponds to a larger ΔT, and therefore provides a higher efficiency. Geometrically, in Fig. 3.9, such a material would move the curves corresponding to thermomagnetic Rankine and Ericsson cycles to the left, while keeping all other curves fixed. According to the aforementioned discussion on the Clausius-Clapeyron relation, the strategy of improving material properties here is to lower the ratio between latent heat and zero-field transformation temperature while retaining

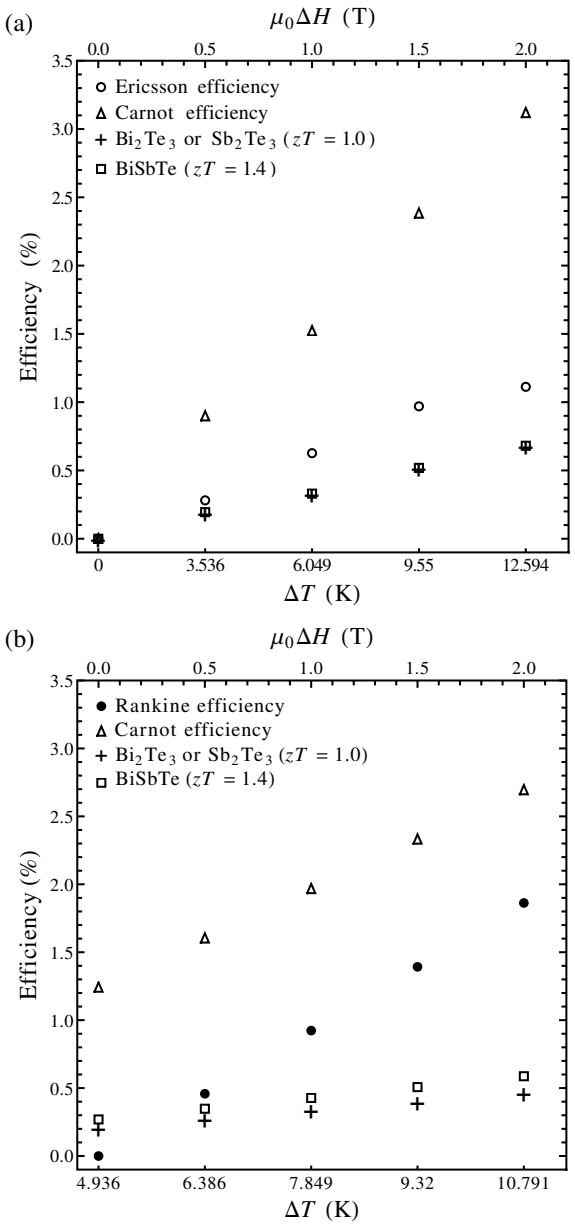

Figure 3.9: Efficiencies of thermodynamic cycles. The efficiencies of thermomagnetic Ericsson (a) and Rankine (b) cycles. (Reproduced with permission [52] ©2013 The Royal Society of Chemistry.)

a large change in magnetization.

3.6 Energy Conversion

The comparison summarized in Fig. 3.9 concerns the efficiency of materials only, both for the thermoelectric and multiferroic devices, with the electromagnetic work output calculated using standard definitions, but not accounting for the way the work output is recovered. Here we postulate and analyze a specific mechanism.

In this section we consider an axisymmetric specimen of the working material surrounded by a pick-up coil and placed near a permanent magnet which applies a background field. The coil is connected to a load that is modeled by a resistor here. We heat and cool the specimen by forced convection or radiation. During the phase transformation, the change in magnetization generates a current in the pick-up coil due to Faraday's law, and this coil further induces a *back-field* on the core region. This back-field decreases (resp., increases) the external field during heating (resp., cooling). Thus the efficiency of converting heat into magnetic work can be estimated by a thermomagnetic Ericsson or Rankine cycle as discussed in the previous section with the change of the field due to the changing back-field. It is the goal of this section to analyze how much of this magnetic work is recovered as the electric work on the load by the proposed device. A schematic of the device is shown in Fig. 2.2a.

In this section we use $\mathbf{H}$ to denote the total magnetic field including external ($\mathbf{H}_{\text{ext}}$) and self-induced ($\mathbf{H}_{\text{m}}$) parts, where the external field further splits into two parts: an applied field ($\mathbf{H}_0$) and a current-induced back field ($\mathbf{H}_{\text{b}}$). The magnetic power done by the external field on the specimen is

$$\mathscr{P}_{\text{mag}} = \int_{\Omega} \mu_0 \mathbf{H}_{\text{ext}} \cdot \dot{\mathbf{M}} \, d\mathbf{x}. \tag{3.17}$$

We model the permanent magnet as a fixed background field $\mathbf{B}_0 = \mu_0 \mathbf{H}_0$ distributed uniformly over Ω. If the thermodynamic system is chosen to be the specimen alone, the first law of thermodynamics gives

$$\frac{d}{dt}\int_\Omega u\, d\mathbf{x} = -\oint_{\partial\Omega} \mathbf{q}\cdot\mathbf{n}\, da + \int_\Omega \mu_0 (\mathbf{H}_0 + \mathbf{H}_\mathrm{b})\cdot\dot{\mathbf{M}}\, d\mathbf{x}, \tag{3.18}$$

where u is the internal energy density, $\mathbf{q}$ is the heat flux per unit area, ϵ_0 is the vacuum permittivity, and $\mathbf{n}$ is the outer normal of the surface $\partial\Omega$. The left hand side of Eqn. (3.18) is the rate of change of the total internal energy. The first term on the right hand side is the total heat flux flowing across the boundary of Ω. The second term on the right hand side is the magnetic power done by the external field on the specimen, as noted above. In this case, the external field contains both the background field from the permanent magnet, $\mathbf{H}_0$, and the back-field induced by the coil, $\mathbf{H}_\mathrm{b}$. Define the total internal energy U and heating power $\mathscr{Q}$ by

$$U = \int_\Omega u\, d\mathbf{x}, \quad \mathscr{Q} = -\oint_{\partial\Omega} \mathbf{q}\cdot\mathbf{n}\, da. \tag{3.19}$$

The integration of the first law around a closed cycle therefore gives

$$\int_{\mathscr{C}} \mathscr{Q}\, dt = -\int_{\mathscr{C}}\int_\Omega \mu_0 \mathbf{H}_\mathrm{b}\cdot\dot{\mathbf{M}}\, d\mathbf{x} dt, \tag{3.20}$$

where $\mathscr{C} = [0, t_1)$ is the time interval of the cycle. Since no internal dissipation is considered, the integral on the left hand side ($= \int_{\mathscr{C}} T\dot{S} dt$) is the area of the corresponding loop in the $T-S$ diagram discussed in the previous section. Here we have shown that the net heat is converted into magnetic work done by the back-field on the specimen. Next, we show that this magnetic work equals the electric work on the load, $\int_{\mathscr{C}} I^2 R\, dt$, where I is the current in the coil and R is the resistance of the load.

The proof can take two approaches: one is a direct proof by Maxwell's equations, and the other is by rewriting the first law for a different choice of the system that consists of all the components, *i.e.* specimen, permanent magnet, coil and load resistor.

In the second approach in which the system consists of the specimen, permanent magnet, coil and resistor, we have to model the continuous cooling of the resistor which is necessary to restore the system to its original state after each cycle. (Of course, in applications, this dissipation to heat would occur in the extended systems served by the energy conversion device.) Without loss of generality, we choose the boundary of this system large enough so that no fields cross it. Since no work is done by this system and there is no change of internal energy in a full cycle, it is then seen that the first law for this system is the heat balance,

$$\int_{\mathscr{C}} \mathscr{Q}\, dt = \int_{\mathscr{C}} I^2 R\, dt, \tag{3.21}$$

i.e., the heat absorbed of the specimen equals the heat dissipated by the load.

Combining Eqn. (3.21) with Eqn. (3.20) we get

$$-\int_{\mathscr{C}}\int_{\Omega} \mu_0 \mathbf{H}_\mathrm{b} \cdot \dot{\mathbf{M}}\, d\mathbf{x} dt = \int_{\mathscr{C}} I^2 R\, dt. \tag{3.22}$$

Equation (36) says that the thermomagnetic efficiency calculated in the previous section is the same as the efficiency of converting heat into electricity using the proposed device, under the assumptions made here. Hence, we conclude that *the magnetic work done by the specimen is fully recovered to the electric work on the load.* In other words, in the formula $\eta = W/Q^+$ used for efficiency in the Sect. 3.4, W is equal to the electric energy dissipated in the load resistor. This argument also clarifies the important role of the back-field in producing this work.

To solve either version of the first law of thermodynamics for the power output,

we need relationships among $\dot{\mathbf{M}}$, $\mathbf{H}_\mathrm{b}$ and I. These relationships are affected by micromagnetic phenomena, heat transfer properties of the heating device and specimen, and the kinetics of phase transformation. A more device-oriented analysis, in addition to a 3D kinetic model of the phase-changing material, is required to further evaluate the performance of such devices.

The final remark we want to make is about demagnetization. Demagnetization is expected to introduce a strong shape dependence to the energy landscape of the material (see Ref. [52], Appendix). In the energy conversion system proposed in this section, although the total magnetic work done by the demagnetization field, $\int_{\mathscr{C}} \mathbf{H}_m \cdot \dot{\mathbf{M}}\, dt$, in a full cycle vanishes, as noted above, it still plays an important role on the specimen-shape dependence of total (magnetic or electric) work output through its influence on the back field. It can be seen by the following arguments. Ampère's law gives a linear relation between the back-field and the current in the coil, $\mathbf{H}_b \propto I$. Faraday's law gives a linear relation between the current and the rate of change in magnetic flux, $I \propto \dot{\mathbf{B}}$. Thus, we have $\mathbf{H}_b \propto \dot{\mathbf{B}}$. The primary contribution to $\dot{\mathbf{B}}$ is the abrupt change in magnetization across phase transformation. Due to demagnetization, this contribution has two components: $\dot{\mathbf{H}}_\mathrm{m}$ and $\dot{\mathbf{M}}$. $\mathbf{H}_\mathrm{m}$ is in general proportional to $\mathbf{M}$. Thus, a significant demagnetization field kills part of the change in magnetization and therefore reduces $\dot{\mathbf{B}}$ drastically, which in turn lowers the back-field $\mathbf{H}_\mathrm{m}$, shrinks the thermomagnetic cycle in the $T-S$ diagram, and finally reduces the efficiency. However, demagnetization is not the only shape-dependent factor in this kind of devices, other such factors include the heat transfer property. A comprehensive analysis on the shape-dependence of the efficiency and the power output, again, requires a more sophisticated thermodynamic model.

Chapter 4

Performance Analysis

4.1 Introduction

The history of ferroic-caloric energy conversion was briefly reviewed in Chapter 1. The purpose of this chapter is to develop a thermodynamic model to evaluate the performance of these energy conversion mechanisms, and the implication for materials development and devices design. Since the thermodynamic analysis of heat engines and refrigerators are almost completely analogous, I focus on the former. In particular, I focus on the efficiency and power output of the novel electricity generation demonstrated by Srivastava *et. al.* [27].

Thermodynamic theories of ferroic-caloric materials aim at predicting energy conversion performance using the data from the two major classes of characterization techniques of ferroic-caloric materials: *direct* and *indirect* measurements. In a direct measurement, through precise calorimetry, the materials response $\theta(F)$ is measured, from which the quantity $\Delta\theta/\Delta F$ is obtained. θ is the temperature and F is the thermodynamic conjugate variable (force) of the ferroic property, denoted X in this chapter. For example, F is the magnetic inductance if X is the magnetization.

Since precise calorimetry is difficult in practice, an easier indirect method has been used more frequently, which measures the response $X(F,\theta)$. The underlying thermodynamic argument is the Maxwell relation $\partial X(F,\theta)/\partial\theta = \partial S(F,\theta)/\partial F$, where S is the entropy. Due to this consideration of experimental simplicity, this work, following our previous paper[52], is based on the thermodynamic function $X(F,\theta)$ and the resulting Gibbs free energy $G(F,\theta)$ which can be fitted [52] by indirect measurement data.

Besides the choice between direct and indirect measurements, the usage of the aforementioned Maxwell relation is also controversial [65, 66]. The problem is that the Maxwell relations in classical thermodynamics are the consequences of the smoothness (second-order differentiability) of thermodynamic potentials, such as the Gibbs free energy, of the material, while during first-order phase transformations, like those giving giant magneto- and electrocaloric effects, the thermodynamic potential changes, at least locally, discontinuously by the definition of such transformations. Hence, the validity of the Maxwell relations are questionable, and the Clausius Clapeyron relation is more suitable [65]. Nevertheless, Sun *et. al.* [66] used a simple derivation to show that the weak (integration) form of the Maxwell relation exactly reduces to the Clausius-Clapeyron relation, if the derivative $\partial X(F,\theta)/\partial\theta$ at the transformation temperature is interpreted as a Dirac delta distribution. In other words, by extending the notion of differentiability to the sense in Lebesgue's theory of integration, the difference between smooth and discontinuous changes of thermodynamic potentials at the first order phase transformation converges. Then, generally speaking, at least for homogeneous materials, the choice between Maxwell and Clausius-Clapeyron relations is only personal. I choose the Clausius-Clapeyron relation in this chapter, because, as I will derive below, this approach gives a simple formula of the efficiency in terms of only one material constant that can be calculated or fitted [52] from the

indirect measurement data $X(F,\theta)$.

Since most of the existing thermodynamic models [22, 23, 52, 67] of ferroic-caloric energy conversion are quasi-static in nature, they cannot predict the power output. The simplest rather acceptably accurate finite-time thermodynamics is the *endoreversible thermodynamics* proposed by Curzon and Ahlborn [38] (see also Ref. 68–72) The terminology "endoreversibility", as proposed by Rubin [70], means that the irreversibility only comes from the heat exchange between the working material and heat reservoirs, while the working material internally still performs reversible processes. The losses due to the finite rate of processes are located only in the interaction between the reversible subsystem and its environment. Van den Broeck [73] proved that the efficiency formula derived by Curzon and Ahlborn [38] (the C-A efficiency) agrees with, without approximation, the theory of linear irreversible thermodynamics, universally up to quadratic order in the deviation from equilibrium [74]. In this chapter, I adopt the assumption of endoreversibility to establish a finite-rate thermodynamic model that is capable of predicting the power output of the new energy conversion method (Sect. 4.2 and 4.3). A natural application of endoreversible thermodynamics is the prediction of cycles with maximum power output [75, 76]. I study ferroic-caloric energy conversion cycles working at maximum power output (Sect. 4.3), with not only the Newton's law of cooling, like what Curzon and Ahlborn did [38], but also the constant power radiative heating. By applying the results to the example of ferromagnetic-ferroelastic materials (Sect. 4.4), we are able to identify another parameter, besides the coefficient in the Clausius-Clapeyron relation, that affects strongly the efficiency and power output. We name it the *figure of merit*. The figure of merit has a noteworthy dependence on the shape of the specimen, which is explored in Sect. 4.4, where other conclusions based on a set of realistic material constants and design parameters are made.

A further question naturally arises here: after the optimized cycle at given working conditions being predicted, what material can be used to perform such a cycle? The answer is related to the constitutive properties, such as heat capacity [77], of the working material. For a phase-transforming material, the most important constitutive properties are the Clausius-Clapeyron coefficient and the figure of merit. By relating these parameters to the study on cycles working at maximum power, we obtain the criteria of matching the devices (material properties + design parameters) and working temperatures for the best performance. Using these criteria, one can choose the most suitable materials/devices for the target working condition, as well as decide the best working conditions for the candidate materials/devices on hand. These criteria are discussed in Sect. 4.4.4.

Before entering the main content of the chapter, I want to make a remark about hysteresis of first order (martensitic) phase transformations in ferroic-caloric materials. Hysteresis is a loss of energy due to irreversible processes during phase transformation cycles that cannot be avoided by any design strategy, which reduces the energy conversion efficiency [59] and causes the functional degradation of materials [3]. An effective way of avoiding hysteresis is in the step of material development. By tuning the composition, the lattice parameters can be made to satisfy the geometrical compatibility condition $\lambda_2 = 1$ [9, 13], where λ_2 is the middle eigenvalue of the transformation stretch matrix. The idea is that when $\lambda_2 = 1$, the stress field at the austenite/martensite interface caused by lattice misfit is eliminated. [14, 51] Experiments confirmed that this strategy leads to low hysteresis, highly stable martensitic materials. The material used as an example in this chapter, the NiCoMnSn alloy, has $\lambda_2 = 1.0032$ and a hysteresis as low as 6 °C [16]. Even in materials not satisfying $\lambda_2 = 1$ by its intrinsic lattice parameters, if the twin wall energy is low, they can form self-organized (adaptive) nanoscale twin laminate whose macroscopically average

lattice satisfies $\lambda_2 = 1$ [78]. This has been confirmed in both ferroelectric [79] and ferromagnetic [80] martensites. Therefore, in the rest part of this chapter, I neglect the thermal hysteresis in phase transformations, which is in fact consistent with the assumption of endoreversibility mentioned above.

4.2 Thermodynamics of Phase Transformation

The thermodynamics of fully non-equilibrium processes has not been well established to date, various assumptions are needed to analyze finite-rate processes by methods analogue to that used in equilibrium thermodynamics, *i.e.* Gibbs' theory [12]. In this chapter, Gibbs' picture of first order phase transformation is validated by adopting the assumption of endoreversibility [38, 72]. Hence, I am able to model finite-rate – but not far away from equilibrium – processes in the energy conversion using phase-changing multiferroic materials.

4.2.1 Clausius-Clapeyron relation and the Rankine cycles

Let the ferroic property of a material is represented by an internal variable X. Examples of X include magnetization and electric polarization. Its thermodynamic working conjugate is denoted F, namely the thermodynamic force of X. Examples of F include magnetic or electric field along the direction of magnetization or polarization. Thus, in the cases considered in the current chapter, X and F are both non-negative, as they have the same positive direction, which I choose to be positive for convenience. One can also think them as the magnitudes of X and F. The Gibbs free energy is then defined by the following two Maxwell relations:

$$\frac{\partial G(F,\theta)}{\partial F} = -X, \quad \frac{\partial G(F,\theta)}{\partial \theta} = -S, \tag{4.1}$$

where θ and S are temperature and entropy of the material respectively. They are defined so that the above Maxwell relations make sense. According to Gibb's theory, a first order phase transformation occurs at the transformation temperature T that satisfies

$$G_m(F,T(F)) = G_a(F,T(F)), \tag{4.2}$$

where the subscripts m and a denote the low and high temperature phases respectively. Note that, as indicated by Eqn. (4.2), the transformation temperature depends on the thermodynamic force. In general, we need the explicit forms of G_m and G_a in oder to solve this equation for $T(F)$, which is called the *Clausius-Clapeyron* relation whose physical interpretation is the effect of thermodynamic force on transformation temperature. An example of such a relation in the alloy $Ni_{44}Co_6Mn_{40}Sn_{10}$ was given in Ref. 27. I shall design the thermodynamic cycles of energy conversion based on the Clausius-Clapeyron relation.

A useful tool of analyzing the performance of an energy conversion system is the temperature-entropy diagram, which depends on the constitutive properties of the working material (Fig. 4.1(a)). During a full thermodynamic cycle, all the state variables of the system, such as internal energy (temperature) and entropy, return to their initial values, thus its trajectory on the temperature-entropy plane forms a loop. Suppose during a cycle the system (material) changes its internal energy while doing work and absorbing heat at the rate of Q, the first law of thermodynamics gives the efficiency of converting heat into work output and the average power output of one full cycle as

$$\eta = \int_{\mathscr{C}} Q\,dt \Big/ \int_{\mathscr{C}} (Q+|Q|)/2\,dt, \quad \mathscr{P} = -\frac{1}{|\mathscr{C}|}\int_{\mathscr{C}} Q dt, \tag{4.3}$$

where $\mathscr{C} \subset [0,\infty)$ is the time interval of a cycle.

Although the most efficient energy conversion cycles are the Carnot cycles, the Rankine cycles are in practical more easier to perform [52]. A Rankine cycle consists of two constant force (isobaric) processes and two adiabatic processes. Denote the two constant forces F_+ and F_- corresponding to heating and cooling processes, respectively. In the rest of this chapter, subscripts + or − indicates the variables associated with the isobaric heating or cooling respectively. Let T_{as}, T_{af}, T_{ms} and T_{mf} be the austenite start, finish, martensite start and finish temperatures of the phase transformation respectively. In an ideal system, they all collapse to a single transformation temperature T which is a function of the thermodynamic force. Let a Rankine cycle be initiated at the state $(F_+, T_{\mathrm{s}+})$ with $T_{\mathrm{s}+} = T_{\mathrm{as}}(F_+)$. Then the specimen is heated to the temperature T_{f+}, while F_+ is fixed. $T_{\mathrm{f}+}$ is determined so that the system has the same entropy of its third state $(F_-, T_{\mathrm{s}-})$, where $T_{\mathrm{s}-} = T_{\mathrm{ms}}(F_-)$, so that we can adiabatically move the system to the latter state. The final process is an isobarically cooling at F_- to the temperature $T_{\mathrm{f}-}$, where $T_{\mathrm{f}-}$ is determined in the same fashion of determining $T_{\mathrm{f}+}$. An example of such a Rankine cycle in the real material $Ni_{44}Co_6Mn_{40}Sn_{10}$ was given in Ref. 52, and a schematic of general cases is shown in Fig. 4.1(b).

4.2.2 Ideal phase transformation systems

It is helpful to parameterize a Rankine cycle so that analytical formulas of efficiency and power output, which capture the main features of performance caused by phase transformation, can be derived, because these formulas can be used to guide the material search and device design. For this purpose, I introduce the model of *ideal phase transformation systems*. This model is based on the following four assumptions.

1. The entropy difference, $S_{\mathrm{a}}(F,\theta) - S_{\mathrm{m}}(F,\theta)$, is a constant.

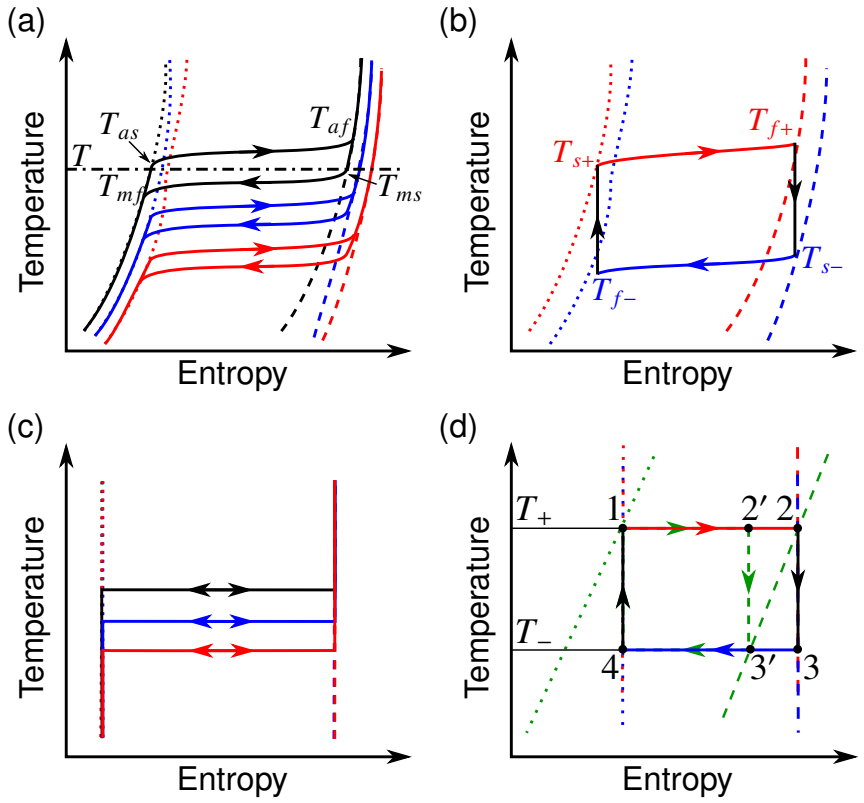

Figure 4.1: Subfigure (a) is a schematic of the constitutive properties of a multiferroic material undergoing first order phase transformation in the temperature-entropy plane. T_{as} (resp. T_{ms}) and T_{af} (resp. T_{mf}) represent respectively the austenite (resp. martensite) start and finish temperatures. T is the transformation temperature determined by equalizing the Gibbs free energy of two phases. In all subfigures, dotted (resp. dashed) lines are curves corresponding to the low (resp. high) temperature single phase. Solid lines representing the effective properties of the whole material. Red, blue, and black indicate the material's behaviors under different thermodynamic forces. Subfigure (b) shows a energy conversion Rankine cycle utilizing the material. $T_{\text{s+}}$ (resp. $T_{\text{s-}}$) and $T_{\text{f+}}$ (resp. $T_{\text{f-}}$) represent respectively the start and finish temperatures of the isobaric processes upon heating (resp. cooling). Subfigures (c) and (d) show respectively the constitutive properties and a Rankine cycle (1234) of an ideal phase transformation system. $T_{\pm}$ are the transformation temperatures under the thermodynamic force $F_{\pm}$ respectively. Subfigure (d) also shows the compare the Rankine cycles of an ideal system to that of a system without the assumption of zero heat capacity, $12'3'4$, where the green curves correspond to the latter system.

This assumption is true if both phases have the same heat capacity at any temperature and under any thermodynamic force. Since we mainly consider solid-solid phase transformation, this assumption is mild. Geometrically, it means that, in the $T-S$ diagram, the isobaric curves corresponding to each single phase are parallel to each other. Under this assumption, the Clausius-Clapeyron relation (4.2) reduces to

$$\frac{dT}{dF} = -\frac{X_\mathrm{a} - X_\mathrm{m}}{S_\mathrm{a} - S_\mathrm{m}} = -\frac{X_\mathrm{a} - X_\mathrm{m}}{\ell / T_0}, \tag{4.4}$$

where ℓ and T_0 are respectively the latent heat and transformation temperature measured at a zero thermodynamic force. I call them the *reference latent heat* and *reference transformation temperature* respectively.

2. $\Delta X := X_\mathrm{a} - X_\mathrm{m}$ is independent of transformation temperature.

   This assumption relies on the fact that if the change in ferroic property X is large relative to its variation with T or F. Under this assumption, Eqn. (4.4) is further simplified,

$$\frac{T - T_0}{T_0} = -\frac{(X_\mathrm{a} - X_\mathrm{m})F}{\ell} = -\frac{\Delta X F}{\ell}. \tag{4.5}$$

   In a dimensionless form, I write

$$\bar{T} = 1 - C\bar{F}. \tag{4.6}$$

   where $\bar{T} = T/T_0$, and $\bar{F} = F/[F]$. $[F]$ is the characteristic unit of thermodynamic force F, which will be chosen accordingly when the exact meanings of X and F are specified. The dimensionless parameter $C = \Delta X[F]/\ell$ is called the *Clausius-Clapeyron coefficient*.

In the rest of this chapter, I shall continue using the superimposed bar to denote dimensionless variables. The corresponding characteristic unit will be specified when a dimensionless variable with the same physical dimension first appears. For example, from now on, all dimensionless temperatures are normalized by T_0.

3. *Reversible phase transformation*: $T_{\mathrm{as}} = T_{\mathrm{af}} = T_{\mathrm{ms}} = T_{\mathrm{mf}} = T$.

   Clearly, this is an assumption of zero hysteresis. It really is just a consequence of the endoreversibility instead of an extra assumption. Even in general, it is also a weak assumption for martensitic phase transformation, given the evidence that by tuning the composition of a family of materials, the hysteresis of such transformation can be reduced to nearly zero.[3] Geometrically, in $T-S$ diagram, under this assumption, isobars and isotherms coincide during phase transformation, as shown in Fig. 4.1(c).

4. *Zero heat capacities*: $S_{\mathrm{a}}(H,T)$ and $S_{\mathrm{m}}(H,T)$ are both constants.

   This is a step further than Assumption 1. Physically, it assumes that the heat capacities of two phases are not just equal but actually vanishing (negligible) simultaneously. It can be validated by the observation on typical differential scanning calorimetry measurements of such solid-solid phase transformation that the peaks at transformation temperatures due to the latent heat absorbed/emitted are much higher than the plateaus whose heights correspond to single phase heat capacities. Geometrically, the isobars of single phases in $T-S$ diagram become vertical lines (see Fig. 4.1(c)). Although it is a strong assumption, it does not affect our predictions of efficiency and power output, as discussed below.

Based on these assumptions, a Rankin cycle is equivalent to a Carnot cycle (Fig. 4.1(d)). A Carnot cycle originally has four degrees of freedom: two temperatures and one entropy difference. Here, it reduces to two because of the constrains introduced by the Clausius-Clapeyron relation (4.6). A convenient choice would be (T_+, T_-) or (F_+, F_-). The efficiency defined by $(4.3)_1$ is now

$$\eta = 1 - \frac{T_-}{T_+} = \frac{C(\bar{F}_- - \bar{F}_+)}{1 - C\bar{F}_+}. \tag{4.7}$$

Since $0 \leqslant \bar{T}_- \leqslant 1 \leqslant \bar{T}_+$, the Clausius-Clapeyron relation (4.6) requires

$$C\bar{F}_+ \leqslant C\bar{F}_- \leqslant 1. \tag{4.8}$$

This is trivial when $C \leqslant 0$, but becomes a constrain on $\bar{F}_\pm$ when $C > 0$, which is $\bar{F}_+ \leqslant \bar{F}_- \leqslant 1/C$.

Let the time of heating, cooling, and adiabatic processes be t_+, t_-, t_0 respectively. The power output defined by $(4.3)_2$ is

$$\mathscr{P} = \Delta X(F_- - F_+)/(t_+ + t_- + t_0). \tag{4.9}$$

Since the adiabatic switching between two thermodynamic forces is irrelevant to the efficiency, and of little interest to the power output: what it does is just a slight change in the denominator, and the change is uncoupled to any other parameter. Common treatments of t_0 is either assuming that it is proportional to $t_+ + t_-$, as Curzon and Ahlborn [38] did, or simply neglecting it, as I shall do in this chapter. We still cannot compute the power output until the heat transfer model is given, which will be discussed in Sect. 4.3.

Finally, consider the corrections due to Assumption 4. The comparison of Rankine cycles with and without those assumptions are shown in Fig. 4.1(d). From Fig. 4.1(d), we see that the assumption of zero heat capacities does not affect either the efficiency formula (4.7) or the average power output formula (4.9). Because, both real and ideal cycles correspond to the same $F_\pm$, therefore the same $\theta_\pm = T_\pm$, which are the only internal parameters on which the heat transfer depends (Sect. 4.3). There are only two minor corrections due to such an assumption. First, the frequency computed by the ideal system model, *i.e.* $f = 1/(t_+ + t_-)$, is actually underestimated, because the real cycle has the same power but a smaller net work output. Let the heat capacity be a constant c, and the entropy of martensite single phase at the reference transformation temperature be zero, the entropy of state 1, 2, and $2'$ are respectively

$$\begin{cases} S_1 = c\ln\left(1 - C\bar{F}_+\right), \\ S_2 = c\ln\left(1 - C\bar{F}_+\right) + \ell/T_0, \\ S_{2'} = S_{3'} = c\ln\left(1 - C\bar{F}_-\right) + \ell/T_0. \end{cases} \tag{4.10}$$

The ratio of real frequency to ideal frequency is the same as that of the area enclosed by 1234 to $12'3'4$, which is in terms of entropy differences

$$\frac{S_2 - S_1}{S_2' - S_1} = \frac{1}{1 + \bar{c}\ln\left[(1 - C\bar{F}_-)/(1 - C\bar{F}_+)\right]}, \tag{4.11}$$

where the heat capacity is normalized by $[c] = \ell/T_0$. Second, it puts an bound on the differnce between F_+ and F_-, because when the difference is too large, the cycle shrinks to a single vertical line , or even an loop with “negative area". The limiting cases is that S_1 is equal to $S_{3'}$. The inequality $S_1 \leqslant S_{3'}$ leads to a constrain on F_+ and

F_-,

$$(1 - C\bar{F}_-) \big/ (1 - C\bar{F}_+) \geqslant e^{-1/\bar{c}}. \tag{4.12}$$

Furthermore, it leads to a bound on the efficiency, $\eta \leqslant 1 - \exp(-1/\bar{c})$. By comparing (4.11) with (4.12), we see that the second correction can also be understood as a consequence of the finiteness of real frequencies.

4.3 Heat Transfer and Power Output

The generic form of a heat transfer law is $Q(\tau, \theta)$, where $\tau > 0$ is the temperature of the heat reservoir (or the environmental temperature, or the ambient temperature). Consider two heat transfer laws in this chapter:

1. Newton's law of cooling: the heat flux depends linearly on the temperature difference between the specimen and the reservoir.

$$Q = Q(\tau, \theta) = \alpha h (\tau - \theta). \tag{4.13}$$

   Above, $h \geqslant 0$ is the heat transfer coefficient with unit of $\mathrm{W/m^2K}$, and α is the ratio of the surface for heat exchange to the volume of specimen.

2. Radiation: We assume that the radiation source is modeled by an assigned heat flux:

$$Q = \alpha q, \tag{4.14}$$

   where q is the radiation power density with the unit of $\mathrm{W/m^2}$. For example, if the radiation source is a perfect black body, then q is given by the Stefan–Boltzmann law.

Then, we can study rate-dependent cycles by specifying the heat transfer methods for heating and cooling branches, in addition to prescribing the time evolution of the heat reservoir, $\tau(t)$. In this chapter, I focus on two heat transfer modes of a Rankine cycle: a) both heating and cooling are convective, and b) cooling is convective and continuous, while heating is radiative and periodic.

4.3.1 Convective heating and cooling

In the first mode of heat transfer, the temperature of heat reservoir is set to be a constant τ_+ (reps. τ_-) during the heating (reps. cooling). Thus, the heating rate as a function of time is given by

$$Q^I(t) = \begin{cases} Q^I_+ := \alpha h_+(\tau_+ - \theta_+), & t \in \mathscr{C}_+; \\ Q^I_- := \alpha h_-(\tau_- - \theta_-), & t \in \mathscr{C}_-. \end{cases} \tag{4.15}$$

$\mathscr{C}_\pm$ denote the time intervals of heating and cooling branches of a cycle, respectively. Here, I adopt the ideal system assumptions given in Sec. 4.2, so the temperature of the specimen during heating or cooling is constant too, *i.e.* $\theta_+ = T_+$ or $\theta_- = T_-$. Their relations to the thermodynamic forces F_+ and F_- are also given above. Clearly, we need $\tau_- \leqslant \theta_- \leqslant \theta_+ \leqslant \tau_+$. The total heat absorbed or emitted during heating and cooling are the corresponding latent heat $\ell_\pm$, respectively. According to the conservation of entropy, as a consequence of endoreversibility (also Assumption. 1), we have

$$\ell_+/\theta_+ = \ell_-/\theta_- = \ell/T_0. \tag{4.16}$$

The time for heating/cooling is then $t_\pm = |\ell_\pm / Q_\pm|$. The (average) power output in terms of $\theta_\pm$ is

$$\mathscr{P} = \frac{\alpha(\theta_+ - \theta_-)}{\dfrac{\theta_+}{h_+(\tau_+ - \theta_+)} + \dfrac{\theta_-}{h_-(\theta_- - \tau_-)}}. \tag{4.17}$$

It can be rewritten in terms of $F_\pm$,

$$\mathscr{P} = \frac{\alpha C(\bar{F}_- - \bar{F}_+)T_0}{\dfrac{1 - C\bar{F}_+}{h_+(\bar{\tau}_+ - 1 + C\bar{F}_+)} + \dfrac{1 - C\bar{F}_-}{h_-(1 - C\bar{F}_- - \bar{\tau}_-)}}, \tag{4.18}$$

where $\bar{\tau}_\pm = \tau_\pm / T_0$. This formula can be used to design the Rankine cycles or predict their power output. The frequency corresponding to this power output is $f = \mathscr{P} T_0 / \ell(\bar{\theta}_+ - \bar{\theta}_-)$. The real frequency will be higher than this due to the correction discussed in Sect. 4.2.

Fixing τ_+ and τ_-, the power output can be maximized over θ_+ and θ_-. The maximizer is given by (see also Ref. 38),

$$\theta_\pm = \frac{1 + \sqrt{h'\tau'}}{1 + \sqrt{h'}} \sqrt{\tau_\pm \tau_+}, \tag{4.19}$$

where $\tau' = \tau_- / \tau_+$ and $h' = h_- / h_+$. Thus, in order to make a Rankine cycle working at maximum power output, the thermodynamic force should be set as $\bar{F}_\pm = (1 - \bar{\theta}_\pm)/C$. The maximum power output and corresponding efficiency and frequency are

$$\mathscr{P}^I_{max} = \alpha h_- \tau_+ \, (1 - \sqrt{\tau'})^2 \Big/ (1 + \sqrt{h'})^2, \tag{4.20a}$$

$$\eta^I_{max} = 1 - \sqrt{\tau'}, \tag{4.20b}$$

$$f^I_{mas} = (\alpha h_- T_0 / \ell) \Big/ (1 + \sqrt{h'\tau'}). \tag{4.20c}$$

Using Eqn. (4.6), we can design a Rankine cycle utilizing a phase-transforming multiferroic material so that the power output is maximized for the given working temperatures. The only requirement is that if the Clausius-Clapeyron coefficient C is positive (resp. negative), then θ_+ (resp. θ_-) must be greater (resp. less) than the reference transformation temperature, T_0.

4.3.2 Radiative heating and convective cooling

In the second heat transfer mode, the heat reservoir is kept at the temperature of τ all the time, while a radiative heating with the power of q is applied during only the heating processes of cycles. Thus, the heating rate is given by the following piecewise constant function of time.

$$Q^{II}(t) = \begin{cases} Q_+^{II} := \alpha q + \alpha h(\tau - \theta_+), & t \in \mathscr{C}_+; \\ Q_-^{II} := \alpha h(\tau - \theta_-), & t \in \mathscr{C}_-. \end{cases} \tag{4.21}$$

Note that the positiveness of Q_+^{II} and negativeness of Q_-^{II} yield $\tau < \theta_- < \theta_+$. This time, the power output in terms of $\theta_\pm$ is

$$\mathscr{P} = \frac{\alpha(\theta_+ - \theta_-)}{\dfrac{\theta_+}{q - h(\theta_+ - \tau)} + \dfrac{\theta_-}{h(\theta_- - \tau)}}. \tag{4.22}$$

In terms of $F_\pm$, it becomes

$$\mathscr{P} = \frac{\alpha C(\bar{F}_- - \bar{F}_+)T_0}{\dfrac{1 - C\bar{F}_+}{q - h(1 - C\bar{F}_+ - \bar{\tau})} + \dfrac{1 - C\bar{F}_-}{h(1 - C\bar{F}_- - \bar{\tau})}}, \tag{4.23}$$

where $\bar{\tau} = \tau/T_0$. Note that, in this case is, $Q_+^{II} > 0$ is not automatically satisfied. Instead, it puts a constrain on θ_+ that $\theta_+ < q/h + \tau$. In terms of F_+, it is $C\bar{F}_+ > 1 - q/hT_0 + \bar{\tau}$.

Following the same arguments used in the preceding subsection, we maximize the power output over $\theta_\pm$ and get

$$\begin{cases} \theta_+ = \tau(1 + q' + \sqrt{1+q'})/2, \\ \theta_- = \tau(1 + \sqrt{1+q'})/2, \end{cases} \tag{4.24}$$

where $q' = q/h\tau$. Note that for any $q' > 0$, the aforementioned constrain on θ_+ due to $Q_+^{II} > 0$ is satisfied by the maximizer $(4.24)_1$. The maximum power output and corresponding efficiency are

$$\mathscr{P}_{max}^{II} = \alpha h\tau \left[q' + 2(1 - \sqrt{1+q'})\right] \Big/ 4, \tag{4.25a}$$

$$\eta_{max}^{II} = q' \Big/ \left[1 + q' + \sqrt{1+q'}\right], \tag{4.25b}$$

$$f_{max}^{II} = (\alpha h T_0/\ell) \left[q' + 2(1 - \sqrt{1+q'})\right] /2q'. \tag{4.25c}$$

An interesting observation is that in Eqn. (4.25), the efficiency approaches 1/2 as $q' \to 0$, while in the previous result, *i.e.* Eqn. (4.20), it goes to 1 as $\tau' \to 0$. Both limiting cases correspond to a 0 K convective cooling.

Both Eqns. (4.20) and (4.25) have no explicit dependence on material constants, but clearly not every material, along with an appropriate device, can perform the cycles described the solutions. Finding materials (or devices) having the particular constitutive properties that match exactly the requirements of a cycle working at

maximum power output is crucial for the performance optimization of energy conversion. Fortunately, phase-transforming materials provide a lot of such opportunities due to the rich variability of constitutive properties in their mixed-phase region in the $T-S$ diagram. [52]

4.4 Example: Thermomagnetic Phase Transformation

4.4.1 Material consideration: thermomagnetic energy conversion

The alloy $Ni_{44}Co_6Mn_{40}Sn_{10}$, as well as its nearby compositions, undergoes a first order martensitic phase transformation from an antiferromagnetic martensite to an ferromagnetic austenite phase upon heating.[16, 37] During the transformation, its magnetization increases about $\Delta M = 10^6$ A/m. The latent heat and transformation temperature at zero-field measured by differential scanning calorimetry (DSC) are respectively about $\ell = 10^8$ J/m^3 and $T_0 = 400$ K. With these three material constants, among other parameters listed in Table 4.1, we can make some analytical predictions based on the ideal system assumptions.

In this example, as shown by Song *et. al.* [52] to be a good approximation of the full 3D continuum theory, $X = M$ and $F = \mu_0 H$, where M is magnetization, H is the *external* magnetic field, and μ_0 is the vacuum permeability. Given that $\Delta M > 0$, the scale of F can be chosen to be $[F] = \mu_0 \Delta M$, so that $\bar{F} = H/\Delta M := \bar{H}$, *i.e.* $[H] = \Delta M$. Other common choices of $[F]$ include $\mu_0 M_s$ and H_0 with M_s being the saturation magnetization of austenite or martensite, and H_0 is a reference magnetic field strength, such as the one generated by a permanent magnet. I choose $\mu_0 \Delta M$ because the resulting Clausius-Clapeyron coefficient is a pure material constant. In fact, all the following analysis is valid for any choice of $[F]$. If the material is modeled

by an ideal system, the Clausius-Clapeyron relation reads, according to Eqn. (4.6),

$$\bar{T} = 1 - C\bar{H}, \tag{4.26}$$

where the dimensionless Clausius-Clapeyron coefficient, in this example, becomes $C = \mu_0(\Delta M)^2/\ell$ which is positive. The efficiency of an ideal Rankine cycle, as given by Eqn. (4.7), is then

$$\eta = \frac{C(\bar{H}_- - \bar{H}_+)}{1 - C\bar{H}_+}. \tag{4.27}$$

Let $\bar{H}_\pm = \bar{H}_0 \pm \Delta\bar{H}$. I decide not to further explore these cycles, because the thermomagnetic energy conversion is of less interest compared to the thermoelectric energy conversion introduced below. Readers who are interested in the detail of these thermomagnetic cycles refer to Ref. 52.

4.4.2 Device consideration: thermoelectric energy conversion

The alloy $Ni_{45}Co_5Mn_{40}Sn_{10}$ was used as the active material in the demonstration of direct energy conversion from heat to electricity [27]. In the demonstration device, as well as its generalized versions discussed below, an axisymmetric specimen of the alloy is placed in a uniform background field – generated by a permanent magnet – and surrounded by a pick-up coil. The coil is connected to a load that is modeled by a resistor here. I drive the phase transformation by the two aforementioned heat transfer modes. During the phase transformation, the change in magnetization generates a current in the pick-up coil due to Faraday's law of induction, and this coil further induces a *back-field* on the core region.

I use the thermodynamics and heat transfer models developed above to analyze the performance of this kind of energy conversion devices. The thermomagnetic cycles of the working material in such devices are the same as described above with

$\bar{H}_0$ being the background field and $\Delta\bar{H}$ being the back-field. As proven in Ref. 52, in this setting, the magnetic work done by the back-field on the alloy is equal to the electricity delivered to the load. So, by studying just the thermomagnetic cycles, we can evaluate the performance of the thermoelectric conversion. A major difference between the cycles considered here and those mentioned before is that the thermodynamics forces are no longer independent parameters of a cycle. Instead, it now depends on the heat transfer properties of the device. Roughly speaking, as one can imagine, a faster heat transfer generates a stronger back-field, *vice versa*. The exact dependence of $\Delta\bar{H}$ on the heat transfer rate can be derived starting with Ampère's and Faraday's laws in electromagnetism.

According to Ampère's law, the vector back-field generated by the coil is a linear function of the current, *i.e.*,

$$\mathbf{H}_b(\mathbf{x}) = \mathbf{l}(\mathbf{x})\, I, \tag{4.28}$$

where the vector field $\mathbf{l}$ is the coefficient of the proportionality, which solely depends on the geometry of the coil. Note that $\mathbf{l}$ is inhomogeneous but varying slowly at the length scale of the core region. For a full loop of wire in the coil, whose enclosing area is $\mathscr{O}$, Faraday's law reads

$$\int_{\partial\mathscr{O}} \mathbf{E}\cdot d\boldsymbol{\ell} = -\int_{\mathscr{O}} \dot{\mathbf{B}}\cdot\mathbf{n}\, da, \tag{4.29}$$

where the vectors $\mathbf{E}$ and $\mathbf{B}$ are electric field and magnetic induction respectively.

When the coil contains N turns, denoted $\mathscr{O}_i$, $i = 1,2,\cdots,N$, the induced electromotive force is

$$\begin{aligned} V &= \int_{\mathscr{W}} \mathbf{E}\cdot d\boldsymbol{\ell} = \sum_{i=1}^{N}\int_{\partial\mathscr{O}_i} \mathbf{E}\cdot d\boldsymbol{\ell} = -\sum_{i=1}^{N}\int_{\mathscr{O}_i} \dot{\mathbf{B}}\cdot\mathbf{n}\,da, \\ &= -\mu_0\sum_{i=1}^{N}\int_{\mathscr{O}_i} (\dot{\mathbf{H}}_b + \dot{\mathbf{H}}_m + \dot{\mathbf{M}})\cdot\mathbf{n}\,da. \end{aligned} \tag{4.30}$$

where $\mathscr{W}$ is the center-line path of the coil and the vector $\mathbf{H}_m$ is the demagnetization field generated by the magnetization. I have used the dipolar relation $\dot{\mathbf{B}} = \mu_0(\dot{\mathbf{H}}_b + \dot{\mathbf{H}}_m + \dot{\mathbf{M}})$ and the fact that the background field is constant. To evaluate the last term, note that because M is the volume averaged magnetization, and the demagnetization field $\mathbf{H}_m$ is proportional to M, we have to a good approximation,

$$\begin{aligned} &\mu_0\sum_{i=1}^{N}\int_{\mathscr{O}_i} (\dot{\mathbf{H}}_m + \dot{\mathbf{M}})\cdot\mathbf{n}\,da \\ =&\mu_0 NA\frac{d}{dt}\frac{1}{vol(\Omega)}\int_0^L\int_{\mathscr{O}_i} \mathbf{H}_m + \mathbf{M}\,da\,dx\cdot\mathbf{n} \\ \approx&\mu_0(1-\delta)NA\dot{M}, \end{aligned} \tag{4.31}$$

where A is the cross-section area of the specimen (distinct from the surface area for heat transfer), and $\delta \in (0,1)$ is the demagnetization factor along the direction of magnetization. δ approaches to its limiting value of 1 (resp. 0), as the shape of the specimen approaches to a thin sheet (resp. thin rod). Suppose the specimen is in the shape of a cylinder with the basal area of A and the height of h, placed in coil co-axially (see Fig. 4.3). Denote the aspect ratio of the specimen $\gamma := \mathsf{h}/2\sqrt{A/\pi}$, the

demagnetization factor δ is well approximated by [81]

$$\delta(\gamma) = \begin{cases} \dfrac{1}{\gamma^2-1}\left[\dfrac{\gamma}{\sqrt{\gamma^2-1}}\ln\left(\gamma+\sqrt{\gamma^2-1}\right)-1\right], & \gamma > 1, \\ 1-\dfrac{\gamma}{1-\gamma^2}\left[\dfrac{\arccos\gamma}{\sqrt{1-\gamma^2}}-\gamma\right], & \gamma < 1. \end{cases} \tag{4.32}$$

Eqns. (4.28), (4.30), and (4.31) imply an ordinary differential equation for the current,

$$IR = V = -\mu_0\left(\sum_{i=1}^{N}\int_{\mathscr{O}_i}\mathbf{l}\cdot\mathbf{n}\,da\right)\dot{I} - \mu_0(1-\delta)NA\dot{M}. \tag{4.33}$$

Here R is the total resistance of the coil and the external load. If the resistance of the coil is non-negligible, the real efficiency and power output are appropriate fractions of the values calculated below.

The term in the parenthesis on the right hand side of (4.33) is the inductance of the coil in air. Closed form formulas of the inductance can be computed for many types of coils, as given, for example, by Terman [82]. For a finite size coil with the length of d and the inner/outer radius of r_i/r_o, the approximation of inductance can be obtained from Biot-Savart's law,

$$\begin{aligned} \mathscr{L} &\equiv \sum_{i=1}^{N}\int_{\mathscr{O}_i}\mathbf{l}\cdot\mathbf{n}\,da \\ &\approx \frac{\pi\bar{r}wN^2}{2\hat{w}}\ln\left(\frac{2(w+\hat{w})+\sqrt{1+4(w+\hat{w})^2}}{2w+\sqrt{1+4w^2}}\right), \end{aligned} \tag{4.34}$$

where $\bar{r} = (r_o + r_i)/2$ is the average radius, $w = 2r_i/d$ is the (inner) aspect ratio, and $\hat{w} = 2(r_o - r_i)/d$. For a single layer solenoid, *i.e.* $\bar{r} = r_i = r_o$, Eqn. (4.34) leads to the

asymptotic formulas [83]:

$$\mathscr{L} \approx \begin{cases} \pi r w N^2/2, & w \ll 1; \\ r N^2, & w \gg 1. \end{cases} \tag{4.35}$$

The key observation on the asymptotic formulas is that for a long coil ($w \ll 1$), $\mathscr{L}$ depends linearly on w, while for a short coil ($w \gg 1$), it is independent of w and therefore suffers no singularity as $w \to \infty$.

4.4.3 Efficiency and the figure of merit

To solve the Eqn. (4.33) for the current, we need a relationship between $\dot{M}$ and I. This relationship is affected by micromagnetic phenomena and the kinetics of phase transformation. Given that little is known about the latter, even for an ideal system, we make the following simple hypothesis of stationary evolution, *i.e.*, $\dot{M}$ is a constant. With these assumptions either the heating or the cooling process yields an explicit solution to (4.33) given by

$$\begin{aligned} I(t) = &- e^{-Rt/\mu_0 \mathscr{L}} [I(0) - \mu_0 (1-\delta) N A \dot{M}/R] \\ &- \mu_0 (1-\delta) N A \dot{M}/R, \end{aligned} \tag{4.36}$$

where $I(0)$ is the initial condition at the beginning of heating or cooling. Given the inductance of a coil as in Eqn. (4.35), when r is in the scale of cm, N is several hundred, and R is 1 Ohm, $R/\mu_0 \mathscr{L}$ is then in the order of $10^3 - 10^4$ Hz. When the time scale of the phase transformation is much slower than this time constant, *i.e.* the frequency satisfies $f \ll R/\mu_0 \mathscr{L}$, the power output is well approximated by its asymptote, or upper bound in the sense of power output, $I = -\mu_0 (1-\delta) N A \dot{M}/R$. Due to

the equivalence of magnetic work and electricity,[52] in a full cycle, the average electric power output converted from heat is $\mathscr{P} = \fint_{\mathscr{C}} I^2 R\, dt = -\fint_{\mathscr{C}} \langle \mathbf{H}_b \cdot \dot{\mathbf{M}} \rangle_\Omega\, dt$. We can write $\langle \mu_0 \mathbf{H}_b \cdot \dot{\mathbf{M}} \rangle_\Omega = -\mu_0^2 (1-\delta)^2 N^2 A \dot{M}^2 / R\mathsf{h}$ in this approximation. Here, the angled brackets denote volume averages, and the dashed integral symbols denote time averages. Let the stationary change of magnetization in heating and cooling processes be $\dot{M}_+ > 0$ and $\dot{M}_- < 0$ respectively, the thermodynamic forces to be used in the Clausius-Clapeyron relation are therefore

$$\mu_0 \bar{H}_\pm = \mu_0 \bar{H}_0 - \mu_0 \hat{C} \dot{\bar{M}}_\pm, \tag{4.37}$$

where $\bar{M} = M/\Delta M$, and $\hat{C} = \mu_0 (1-\delta)^2 N^2 A \Delta M / R\mathsf{h} H_0$. Hence, $\dot{\bar{M}}_\pm$ have the dimension of time^{-1}, and $\hat{C}$ has that of time. The efficiency as given by Eqn. (4.27) is now

$$\eta = \frac{C\hat{C}(\dot{\bar{M}}_+ - \dot{\bar{M}}_-)}{1 - C\bar{H}_0 + C\hat{C}\dot{\bar{M}}_+}. \tag{4.38}$$

The power output is

$$\mathscr{P} = -\ell C \hat{C} \dot{\bar{M}}_+ \dot{\bar{M}}_-, \tag{4.39}$$

and the corresponding frequency is

$$f = \dot{\bar{M}}_+ \dot{\bar{M}}_- \Big/ \left(\dot{\bar{M}}_- - \dot{\bar{M}}_+ \right). \tag{4.40}$$

If the heat transfer method is specified, we can compute $\dot{\bar{M}}_\pm = Q_\pm / \ell_\pm$. Here, I discuss the two aforementioned modes of heat transfer. In the first mode, $Q_\pm$ are given by Eqn. (4.15). Combining Eqns. (4.15),(4.16) and (4.26), under the help of (4.37), we obtain a pair of equations for $\dot{\bar{M}}_\pm$. Solving them for $\dot{\bar{M}}_\pm$ leads to

$$\dot{\bar{M}}_\pm = g(z z'_\pm, \hat{\tau}_\pm)(1 - C\bar{H}_0)/2C\hat{C}, \tag{4.41}$$

where $\hat{\tau}_\pm = \bar{\tau}_+/(1-C\bar{H}_0)$, $z'_- = h' = h_-/h_+$, $z'_+ = 1$, and the dimensionless function $g(z,\tau)$ is defined as

$$g(x,y) := -x - 1 + \sqrt{(x+1)^2 + 4x(y-1)}. \tag{4.42}$$

Note that g is positive (resp. negative) and monotonically increasing (resp. decreasing) when $y > 1$ (resp. $y < 1$), and it is identically zero when $y = 1$. I name the dimensionless parameter

$$z = \frac{C\hat{C}\alpha h_+ T_0}{(1-C\bar{H}_0)\ell} \tag{4.43}$$

the *figure of merit* of such an energy conversion device using the given material and the given heat transfer mode. Under these definitions, the efficiency (4.38) can be rewritten as a function of $\hat{\tau}_\pm$, $z'_\pm$ and z, *i.e.*

$$\eta = \frac{g(zz'_+,\hat{\tau}_+) - g(zz'_-,\hat{\tau}_-)}{2 + g(zz'_+,\hat{\tau}_+)}. \tag{4.44}$$

Similarly, the power output (4.39) and the frequency (4.40) reduce to

$$\hat{\mathscr{P}} := \mathscr{P}/(1-C\bar{H}_0)\alpha h_+ T_0 = -g(zz'_+,\hat{\tau}_+)g(zz'_-,\hat{\tau}_-)/4z, \tag{4.45}$$

$$\hat{f} := \frac{2C\hat{C}f}{(1-C\bar{H}_0)} = \frac{-g(zz'_+,\hat{\tau}_+)g(zz'_-,\hat{\tau}_-)}{g(zz'_+,\hat{\tau}_+) - g(zz'_-,\hat{\tau}_-)}. \tag{4.46}$$

Recall that the thermodynamic force must be non-negative, Eqn. (4.37) requires $\hat{C}\dot{\bar{M}}_+ \leqslant \bar{H}_0$, which introduces a constrain on $\hat{\tau}_+$, according to Eqn. (4.41),

$$g(zz'_+,\hat{\tau}_+) < 2C\bar{H}_0/(1-C\bar{H}_0). \tag{4.47}$$

Another constrain caused by the correction of non-zero heat capacities, *i.e.* Eqn. (4.11),

is now

$$\frac{1+g(zz'_+,\hat{\tau}_+)/2}{1+g(zz'_-,\hat{\tau}_-)/2} \geqslant e^{-1/\bar{c}}. \tag{4.48}$$

Since $g(zz'_+,\hat{\tau}_+)>0$ and $g(zz'_-,\hat{\tau}_-)<0$, this is a weak constrain when $\bar{c}$ is small.

If, instead, the second heat transfer mode, Eqn. (4.21), is used, the solutions for $\dot{\bar{M}}_\pm$ are still in the form of Eqn. (4.41) but with different parameters: $z'_\pm = 1$, $\hat{\tau}_- = \bar{\tau}/(1-C\bar{H}_0)$, $\hat{\tau}_+ = (\bar{\tau}+q/hT_0)/(1-C\bar{H}_0)$. The figure of merit is the same as Eqn. (4.43), except h_+ is now replaced by h. The efficiency and power output are given by the same equations, (4.44) and (4.45) respectively.

Notice that $\lim_{x\to\infty} g(x,y) = 2(y-1)$, the Carnot efficiency is recovered as $z\to\infty$, *i.e.* $\lim_{z\to\infty}\eta = 1-(\hat{\tau}_-/\hat{\tau}_+) = 1-(\tau_-/\tau_+)$, but the effective power output vanishes, *i.e.* $\lim_{z\to\infty}\hat{\mathscr{P}} = 0$. By plotting the efficiency and power output with varying z in Fig. 4.2, we confirm the above two claims and observe a maximum power output occurring at some finite z. For the constants used in plotting Fig. 4.2, which are $z'_\pm = h' = 1$, this critical value of z is 1. Moreover, we find that the C-A efficiency [38] is recovered when $z=1$, again with the constants used in the plotting.

A noteworthy property of z is its dependence on the shape of specimen, in particular the aspect ratio γ, because of the geometry-dependent factors such as $\hat{C}$, α and A/h. We consider, in this chapter, two types of configurations in which the shape-dependence of z can be explicitly derived (Fig. 4.3).

a) A disk with heat transfer through the top surface (Fig. 4.3(a))

   The surface-volume ratio of heat transfer for this configuration is then simply $\alpha = 1/\mathrm{h}$, Thus, the shape-dependence of z is

$$z \propto [1-\delta(\gamma)]^2/\gamma^2. \tag{4.49}$$

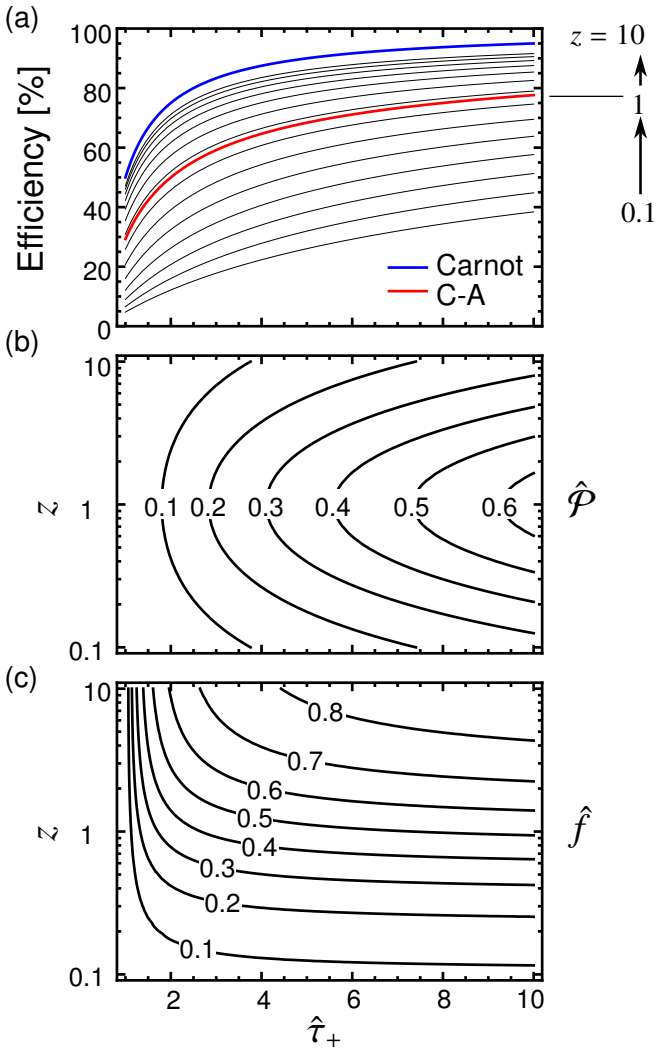

Figure 4.2: (a) Efficiency, (b) effective power output, and (c) effective frequency of the proposed device with the figure of merit varying from 0.1 to 10. The blue and red curves represent the Carnot and Curzon-Ahlborn [38] (C-A) efficiencies, respectively. In this plot, I choose $z'_{\pm} = h' = 1$ and $\hat{\tau}_- = 0.5$.

By plotting it in Fig. 4.3(a), I conclude that the best aspect ratio for this configuration is thin film, *i.e.* $\gamma \to 0$, where the value of the geometry factor is $\lim_{\gamma\to 0} [1-\delta(\gamma)]^2/\gamma^2 = \pi^2/4$.

b) A cylinder with heat transfer through the side surface (Fig. 4.3(b))

In this configuration, the surface-volume ratio of heat transfer is $\alpha = 2/\sqrt{A/\pi}$. The shape-dependence of z becomes

$$z \propto 4[1-\delta(\gamma)]^2/\gamma. \tag{4.50}$$

The coefficient 4 is chosen so that the shape-independent part of z is the same in both configurations, so the value computed from (4.49) and (4.50) are comparable. Note that it has one less order dependence on the aspect ratio γ. Consequently, a large γ is more favorable in this configuration than it is in the previous one. However, as shown in Fig. 4.3(b), a nano-wire, *i.e.* $\gamma \to \infty$ ($1/\gamma \to 0$), is not the best shape. Instead, there exists an optimized aspect ratio near $\gamma = 0.7$ ($1/\gamma = 1.4$).

Overall, the shape-dependence of z is weak, given the fact that it exhibits no singularity for any γ. However, the dimensional power output $\mathscr{P}$, as given in (4.45), has one more dependence on the surface-column ratio α, and therefore might exhibit singularities at some extreme geometries. So, it is power output rather than efficiency that is more sensitive to the tuning of the aspect ratio.

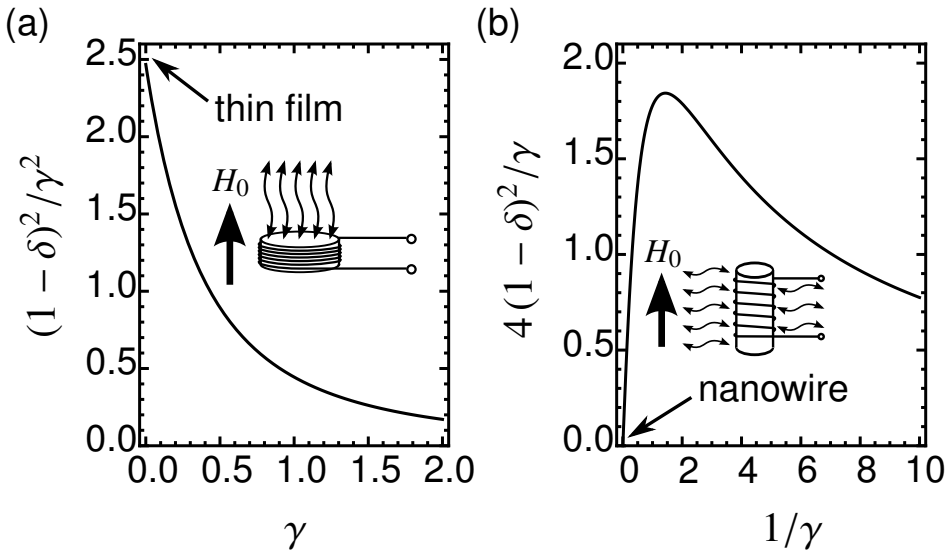

Figure 4.3: Shape-dependence of the figure of merit for devices with heat exchanging through the (a) top or (b) side surface. In the insets, the cylinder represents the specimen which is surrounded by a coil, the curly double arrows indicate the surface of heat-exchange, and the bold arrow shows the direction of the background magnetic field.

4.4.4 Energy conversion at maximum power

On the one hand, in Sect. 4.3, we found that when heat transfer parameters, h's, τ's and q, are fixed, there exists a pair of θ_+ and θ_- for which the constrained optimization problem can be solved to provide the maximum power. On the other hand, in the Sect. 4.4.3, we saw that in an ideal thermoelectric conversion system , the same set of heat transfer parameters also gives the energy conversion Rankine cycle for a given material, as well as its efficiency and power output. Thus, there is an issue about matching. We name it the *design-task matching* problem. We call the set of material constants and design parameters the *most suitable device* to work under certain working (heat transfer) conditions, if such device can perform the predicted maximum-power cycle. In the same manner, we can define the *best working conditions* for a given design, *i.e.* material constants + design parameters. The design-task matching is the focus of this subsection.

First, consider the case of convective heating and cooling. Comparing the results in Sect. 4.3 and Sect. 4.4.3, more specifically using (4.19), (4.26), (4.37) and (4.41), we have

$$1+g(zz'_{\pm},\hat{\tau}_{\pm})/2=\frac{1+\sqrt{h'\tau'}}{1+\sqrt{h'}}\sqrt{\hat{\tau}_{\pm}\hat{\tau}_{+}}. \tag{4.51}$$

As material constants, design parameters and heat transfer conditions vary, Eqn. (4.51) does not always have a non-trivial solution. There are two special cases: i) $\hat{\theta}_+$ and $\hat{\theta}_-$ coincide, and ii) $\hat{\theta}_-$ in the solution approaches zero. Here $\hat{\theta}_{\pm}=\bar{\theta}_{\pm}/(1-C\bar{H}_0)$. In case i), $\hat{\tau}_+$ and $\hat{\tau}_-$ must coincide too. So let $\hat{\tau}_+=1+\epsilon$ and $\hat{\tau}_-=1-\kappa\epsilon$, for some $\kappa,\epsilon>0$ where ϵ is small. Expanding (4.51) to the first order in ϵ leads to a pair of equations whose solution is $\kappa=1$, $z=1/\sqrt{h'}$. This gives one bound on z for the existence of non-trivial solutions, which is $1/\sqrt{h'}$. For case ii), let $\hat{\tau}_-=0$, then solving $\hat{\theta}_-=0$ for z leads to the second bound on z that is $1/h'$. The relative size of two bounds depends

on whether h' is greater or less than 1. In either case, we can write

$$\min\{1/\sqrt{h'}, 1/h'\} \leqslant z \leqslant \max\{1/\sqrt{h'}, 1/h'\}. \tag{4.52}$$

Consequently, when $h' = 1$, *i.e.* the same fluid manifold is used for heating and cooling, the figure of merit z must be strictly 1. It puts a quite rigid constrain on the design-task matching. Solutions to the matching equation (4.51) with $h' = 0.2$ and 2 are plotted in Fig. 4.4. The intersections between a vertical line and the $\hat{\tau}_\pm$ curves suggest a design-task matching: the best working temperatures are their vertical coordinates, and the most suitable design is characterized by their common horizontal coordinate.

Second, consider the mode of convective cooling and radiative heating. The modified Eqn. (4.51), according to (4.24), (4.26), (4.37) and (4.41), is now

$$\begin{cases} 1 + g(z, \hat{\tau})/2 = \hat{\tau}(1 + \sqrt{1 + q'})/2, \\ 1 + g(z, \hat{\tau}(1 + q')/2 = \hat{\tau}(1 + q' + \sqrt{1 + q'})/2, \end{cases} \tag{4.53}$$

By observation, we find that

$$q' = \left(\frac{1 - z - \hat{\tau} - \sqrt{(z-1)^2 + 4z\hat{\tau}}}{\hat{\tau}} \right)^2 - 1 \tag{4.54}$$

solves both equations in (4.53) simultaneously, regardless of z. Thus, for each $\hat{\tau} \in (0, 1)$, there is a family of solutions to the design-task matching. The only constrain is $\hat{\theta}_+ > 1$, which reduces to

$$z < \left(\hat{\tau} + 3\sqrt{\hat{\tau}} + 2 \right) \Big/ 2. \tag{4.55}$$

Or, if $z > 0$ is given, the constrain on $\hat{\tau}$ is

$$\begin{cases} 0 < \hat{\tau} < 1, & 0 < z \leqslant 1, \\ \dfrac{5 + 4z - 3\sqrt{1+8z}}{2} < \hat{\tau} < 1, & 1 < z < 3, \\ \hat{\tau} \notin (0,1), & z \geqslant 3. \end{cases} \tag{4.56}$$

Both (4.55) and (4.56) suggest that $z < 3$. In Fig. 4.5, I plot the region in $z - \hat{\tau}$ plane where the design-task matching has non-trivial solutions.

4.4.5 Real materials

In Table 4.1, I list the material properties close to those of the alloy $Ni_{44}Co_6Mn_{40}Sn_{10}$, as well as other realistic design parameters and heat transfer conditions. The configuration of the device corresponds to the inset of Fig. 4.3(a). The heat transfer coefficients are the typical values of enforced or free convection by common fluids.

The Clausius-Clapeyron coefficient computed from these parameters is $C = 0.01$, which is positive. The parameter $\hat{C} = 7.6 \times 10^{-6}$ s, which is quite small. Unsurprisingly, the figure of merit, $z = 3.1 \times 10^{-5}$, is small too. As a consequence, the efficiency will also be low. Even worse, it is difficult to solve the design-task matching, at least with convective heating and cooling, for this extremely small z, as it is likely to be out of the range between $1/\sqrt{h'}$ and $1/h'$ mentioned in Sect. 4.4.4. Thus, improving the figure of merit to around the order of 1 is undoubtedly one of the most urgent tasks for future works.

However, even for such a low-z material, it is still possible to obtain a good performance in terms of the power output. The power output and frequency with convective heating and cooling for parameters listed in Table 4.1 are plotted in Fig. 4.6,

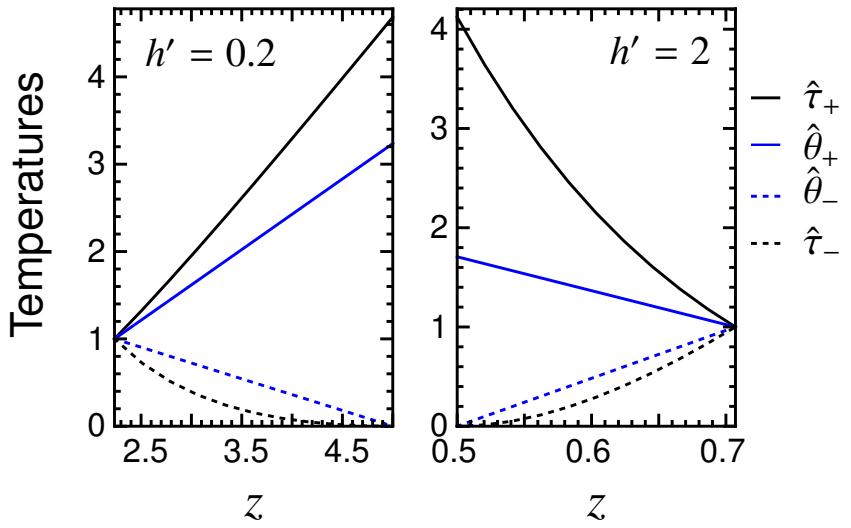

Figure 4.4: Solutions to the design-task matching with convective heating and cooling, and $h' = 0.2$ (left) or 2 (right).

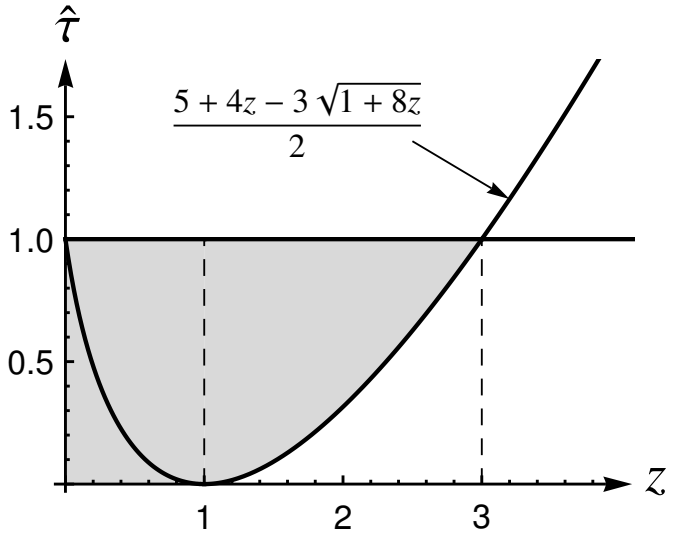

Figure 4.5: The region in $z - \hat{\tau}$ plane where a solution to the design-task matching with radiative heating and convective cooing can be found.

parameter	description	value	unit
ΔM	change of magnetization	10^6	A/m
ℓ	latent heat at zero-field	10^8	J/m^3
T_0	transformation temperature	400	K
A	basal area of the cylinder	4π	cm^2
h	height of the cylinder	10	μm
$\mu_0 H_0$	background magnetic field	1	T
N	number of turns in the coil	500	
R	resistance of the load	1	Ohm
h_+	heat transfer coefficient	1000	W/m^{2}K
h_-	heat transfer coefficient	200	W/m^{2}K

Table 4.1: Parameters used in the example. The first group contains material constants which are approximately those of $Ni_{44}Co_6Mn_{40}Sn_{10}$. The second group contains design parameters. The third group contains heat transfer conditions (coefficients).

where we see that the power output density is not too bad. A similar result can be obtained by studying the other method of heat transfer. Note that the major limitation on the frequency is the cost of switching between the heating and cooling processes. For that, a frequency less than 10 Hz would be considered feasible. Our goal here is to retain, or increase, the power output while reducing the frequency to less than 10 Hz.

When x is in the vicinity of zero, the g-function can be linearized as $g(x,y) = 2x(y-1)+\mathcal{O}(x^2)$. Substituting its linear part into Eqns. (4.45) and (4.46) gives

$$\begin{cases} \mathscr{P} = (\alpha h_+ T_0 z)\,(1-C\bar{H}_0)h'\,(\hat{\tau}_+ - 1)\,(1-\hat{\tau}_-)\,, \\ f = \dfrac{\alpha h_+ T_0}{\ell}\dfrac{h'\,(\hat{\tau}_+ - 1)\,(1-\hat{\tau}_-)}{(\hat{\tau}_+ - 1)+h'\,(1-\hat{\tau}_-)}. \end{cases} \tag{4.57}$$

Excluding terms that are always in the order of 1, our task reduces to fixing, or improving, $\alpha h_+ T_0 z$ while lowering $\alpha h_+ T_0/\ell$. For that, our strategy boils down to two steps: i) decrease $\alpha h_+ T_0/\ell$ by any possible method; ii) if the power output is unaffected or increased during the first step, we are done. Otherwise, tune those parameters other than α, h_+, T_0 or ℓ to raise the power back. Note that among those parameters, we are most likely to tune N and R. Some examples of such a strategy are listed in Table 4.2.

Form Table 4.2, we see that our simple strategy works, and the following two interesting observations are found. First, by comparing Case 1 with Case 2, we see that increasing N and decreasing R have about the same effect on the improvement of performance. The latter is much easier, once we realize that decreasing R is equivalent to distributing the load to multiple units. It also suggests that using a large number of units simultaneously might be a way to increase z to the order of 1. Second, although increasing the latent heat ℓ can directly decreases the frequency, but it is

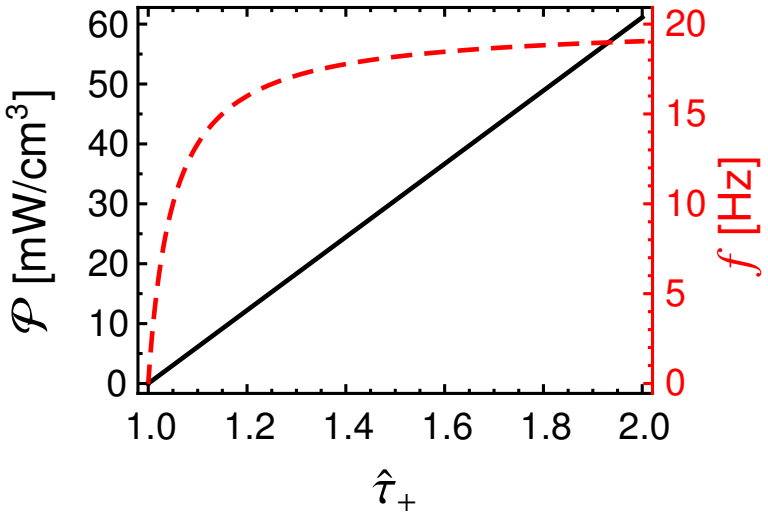

Figure 4.6: The power output density (black solid line and the left axis) and the frequency (red dashed line and the right axis) of a design based on realistic parameters, as listed in Table. 4.1.

	step i	step ii	$\mathscr{P}$ [mW/cm^3]	f [Hz]	z
	original performance		31	18	3.1E-6
1	h $\to$ 100 μm	$N \to 2000$	48	1.8	4.9E-4
2	h $\to$ 100 μm	$R \to 0.1$ Ohm	30	1.8	3.1E-4
3	$T_0 \to 300$ K h $\to$ 50 μm	$R \to 0.1$ Ohm	34	2.7	2.3E-4
4	$\ell \to 10^9$ J/m^3	$R \to 0.1$ Ohm	3.1	1.8	3.1E-6
5	$\ell \to 10^7$ J/m^3 h $\to$ 500 μm	$R \to 0.1$ Ohm	546	3.6	0.032
6	$\ell \to 10^7$ J/m^3 h $\to$ 100 μm	$R \to 0.1$ Ohm	2864	18	0.034

Table 4.2: Examples of strategies to improve the energy conversion performance. The working temperatures are $\hat{\tau}_- = 0.75$ and $\hat{\tau}_+ = 1.5$.

evident from Case 4 and 5 that lowering ℓ is actually much more favorable from the point of view of the power output. That is because the latter increases the Clausius-Clapeyron coefficient and, subsequently, the figure of merit z. This might also give us some clue of bringing z to the order of 1.

In this chapter, all the analysis before Sect. 4.4.5 is a theoretical model based on the following assumptions: i) the ideal phase transformation system introduced in Sect. 4.2.2; ii) the heat transfer laws given in Sect. 4.3; and iii) the approximation of the ODE of current discussed in Sect. 4.4.3. Figs. 4.2 to 4.5 are predictions derived from the model.

Fig. 4.6 and Table 4.2 are calculated using the model and the parameters listed in Table 4.1. Unfortunately, there are no experimental data available to compare with at this time. To do such experiments, we need a material with properties listed as the first three rows of Table 4.1, such as an alloy in the family NiCoMnSn. Then one needs to build a device with parameters listed as the next five rows in Table 4.1, or modified according to Table 4.2. According to standard data for heat transfer coefficients [84], the values listed in Table 4.1 can be achieved by forced and free convective heat transfer with air. One thing to keep in mind is that the final apparatus must have the ability to track heat and work input and output accurately for the whole device, in order to compare with the thermodynamic analysis.

The most difficult part of these measurements is likely to be the measurement of the heat input and output of the whole device, which may require a whole-device calorimeter. We note that if energy is consumed by a device to supply hot air, this contribution must be included in the work consumed, and the effect is to lower the overall efficiency. A simple but less accurate way to estimate the heat input is to use the measured latent heat of the material, scaled to the actual size. This may not be sufficiently accurate because (i) the DSC rate will usually differ from the actual rate

of heat transfer, (ii) the DSC measurement is typically done with no applied field, (iii) the "tails" in a heat flow vs. temperature graph from DSC are difficult to estimate, (iv) the dissipation due to twin boundary and magnetic domain wall boundary motion may be different in a DSC machine than in the actual device. The power output can be directly monitored by a voltage or current meter, as long as the internal and external resistance are measured accurately.

Chapter 5

Conclusions and Future Work

5.1 Conclusions

During martensitic phase transformation, the crystal structure of the material changes significantly. Since ferroelectric and ferromagnetic properties depend sensitively to the lattice parameters, materials undergoing martensitic phase transformation often exhibit abrupt changes of these properties. Such change can be utilized to convert heat into electricity by classical electromagnetism. The concept has been demonstrated on an alloy $Ni_{45}Co_5Mn_{40}Sn_{10}$ which has an abrupt change in magnetization during martensitic phase transformation.

Thermodynamic analysis shows that Clausius-Clapeyron relation, *i.e.* the effect of magnetic field on transformation temperature, is crucial for this kind of energy conversion. That is because in order to have finite work output, the phase transformation must occur at different temperatures upon heating and cooling in a cycle. The Clausius-Clapeyron relation can be obtained by Gibbs free energy, and the latter can be modeled by classical phenomenological thermodynamics and fitted by experimental data. Based on the fitted phenomenological model, thermodynamic

cycles can be designed and analyzed. As a result, we found that the efficiency of the new energy conversion method can exceed that of the state-of-the-art thermoelectric materials, if the transformation temperature upon heating and cooling are sufficiently separated.

The discussion on power output requires a finite-time thermodynamic model. I developed one based on the assumptions of ideal phase transformation system and endoreversibility. Under such assumptions, a Rankine cycle is a Carnot cycle, which is one of the advantages of this method mentioned in Introduction. Using Newton's law of cooling and simple thermal radiation model, efficiency, power output and frequency were derived analytically. In the resulting formulas, a dimensionless parameter z is identified as an important figure of merit, because it is the only parameter that combines the contributions from electromagnetism, heat transfer and material properties. It was shown that as z approaches to infinity, the efficiency approaches the Carnot efficiency. There exists a critical value of z which gives the Curzon-Ahlborn efficiency and maximum power output. In symmetric heat transfer cycles, this critical value is 1. Solving the power maximization problem gives the "matching condition" between the device (z) and the working condition ($\tau_{\pm}$).

5.2 Future work

The predictions given in Chapter 3 and 4 need to be confirmed by experiments. To do those experiments, we need to design an apparatus which can work with various heating and cooling methods, as well as a way to quantitatively measure the efficiency and power output. These will be tasks of future work.

The method presented in Chapter 2 represents one of several ways multiferroics can be used as new kinds of energy conversion devices. Using the caloric effects in

multiferroic materials to convert energy between heat and electricity stretches back to 1800's, as reviewed in Introduction, Sect. 1.3. We present a summary in Table 5.1. Some of them have been demonstrated for refrigeration, but few for electricity generation. For all these cases one must pay due attention to reversibility and low hysteresis, so these terms are omitted from the last column. Some of these cases are obvious. Others are more subtle. While the present alloy uses a big difference in magnetization of the two phases, this is not essential. One could have a transformation between phases having nearly the same magnetization, but quite different magnetic anisotropy, as in the alloy Ni_2MnGa: in Ni_2MnGa the austenite is cubic with anisotropy constants K_1 near 4000 J/m^3 and $K_2 = -9K_1/4$, while the martensite is uniaxial with $K_u = 2.45 \times 10^5$ J/m^3, but the magnetization changes by a factor of only 7/8. In that case a carefully tuned applied field would easily rotate the magnetization in one phase (austenite, in Ni_2MnGa) but not in the other, leading to an effective large change of the magnetic moment during transformation. Ferroelectrics can be used like ferromagnetics in many ways, Table 5.1, but have the additional flexibility of being able to directly move free charges. As an opposite of ferroelectric to dielectric transformation, metal-insulator transition can be used in the same way. That is because the metal phase has an ultra-high (infinite in theory) value of permittivity while the insulator or semi-conducting phase has a finite value of it. An interesting possibility revealed by the presence of the second peaks in Figure 2.2(c) is that the quite sharp drop at the Curie temperature can also induce a significant voltage. In fact, this possibility was noticed long ago by Tesla [18]. We have concentrated on simple mechanisms in Table 5.1. Given a suitable material exhibiting two or more effects, more sophisticated devices are possible.

	Phase 1	Phase 2	Physics	Notes
1.	Ferromagnetic	Nonmagnetic	Faraday's law	Biasing by a permanent magnet; external coil
2.	Ferroelectric	Nonferroelectric	Ohm's law	Biasing by a capacitor; polarization-induced current
3.	Ferromagnetic; high anisotropy	Ferromagnetic; low anisotropy	Faraday's law	Biasing by a permanent magnet, external coil intermediate magnetic field;
4.	Ferroelectric; high permittivity	Ferroelectric; low permittivity	Ohm's law	Biasing by a capacitor, intermediate electric field; polarization-induced current
5.	Ferromagnetic; large M_s near T_c	Nonmagnetic	Faraday's law	Second-order transition; biasing by a permanent magnet [18]
6.	Ferroelectric; large P_s near T_c	Nonpolar	Ohm's law	Second-order transition; biasing by a capacitor
7.	Metal	Insulator or Semiconductor	Ohm's law	Biasing by a capacitor; polarization-induced current
8.	Nonpolar; nonmagnetic	Nonpolar; nonmagnetic	Stress-induced transformation; Faraday's law	Shape-memory engine driving generator; biased by stress [35]

Table 5.1: Methods of conversion of heat to electricity using phase transformations in multiferroics. In all cases the transformation is induced by direct heating and cooling. M_s is the saturation magnetization. P_s the saturation polarization, and T_c the Curie temperature (magnetic or ferroelectric, resp.) (Reproduced with permission [27] ©2011 WILEY.)

References

[1] Wikipedia. Solar Energy Generating Systems — Wikipedia, The Free Encyclopedia (2013). URL http://en.wikipedia.org/wiki/Solar_Energy_Generating_Systems. Online; accessed 27-August-2013.

[2] Lawrence Livermore National Laboratory. URL http://flowcharts.llnl.gov.

[3] Zarnetta, R. *et al.* Identification of quaternary shape memory alloys with near-zero thermal hysteresis and unprecedented functional stability. *Advanced Functional Materials* **20**, 1917–1923 (2010).

[4] Song, Y., Chen, X., Dabade, V., Shield, T. W. & James, R. D. Enhanced reversibility and unusual microstructure in a phase-transforming material. *Nature* (2013). Doi: 10.1038/nature12532.

[5] James, R. D. & Zhang, Z. A way to search for multiferroic materials with "unlikely" combinations of physical properties. In Planes, A., Manosa, L. & Saxena, A. (eds.) *The Interplay of Magnetism and Structure in Functional Materials*, vol. 79, 159 (Springer, New York, 2005).

[6] Chen, X., Srivastava, V., Dabade, V. & James, R. D. Study of the cofactor conditions: conditions of supercompatibility between phases. *Jounral of the Mechanics and Physics of Solids* forthcoming (2013).

[7] Cui, J. *et al.* Combinatorial search of thermoelastic shape-memory alloys with extremely small hysteresis width. *Nature Materials* **5**, 286–290 (2006).

[8] Otsuka, K. & Wayman, C. M. *Shape memory materials* (Cambridge University Press, 1999).

[9] Bhattacharya, K. *Microstructure of martensite : why it forms and how it gives rise to the shape-memory effect* (Oxford University Press, Oxford, 2003).

[10] Pitteri, M. & Zanzotto, G. *Continuum models for phase transitions and twinning in crystals* (Chapman and Hall/CRC, 2010).

[11] Chadwick, P. *Continuum Mechanics: Concise Theory and Problems* (Dover Publications, Inc., New York, 1976), 2nd corrected and enlarged edn.

[12] Gibbs, J. W. A method of geometrical representation of the thermodynamic properties of substances by means of surfaces. *Transactions of the Connecticut Academy of Arts and Sciences* **2**, 382–404 (1873).

[13] Ball, J. M. & James, R. D. Fine phase mixtures as minimizers of energy. *Archive for Rational Mechanics and Analysis* **100**, 13–52 (1987).

[14] Zhang, Z., James, R. D. & Müller, S. Energy barriers and hysteresis in martensitic phase transformations. *Acta Materialia* **57**, 4332–4352 (2009).

[15] Wechsler, M. S., Lieberman, D. S. & Read, T. A. On the theory of the formation of martensite. *JOM, Transactions of AIME* (1953).

[16] Srivastava, V., Chen, X. & James, R. D. Hysteresis and unusual magnetic properties in the single Heusler alloy $Ni_{45}Co_5Mn_{40}Sn_{10}$. *Applied Pyhsics Letters* **97**, 014101 (2010).

[17] Warburg, W. Magnetische untersuchungen. *Annalen der Physik (Leipzig)* **13**, 141 (1881).

[18] Tesla, N. Pyromagneto-electric generator (1890). US Patent 428,057.

[19] Kobeko, P. & Kurchatov, I. Dielectric properties of ferroelectrics. *Zeitschrift für Physik* **66**, 192 (1930).

[20] Hegenbarth, E. Studies of the electrocaloric effect of ferroelectric ceramics at low temperatures. *Cryogenics* **1**, 242–243 (1961).

[21] Scott, J. Electrocaloric materials. *Annual Review of Materials Research* **41**, 229–240 (2011).

[22] Clingman, W. H. & Moore Jr., R. G. Application of ferroelectricity to energy conversion processes. *Journal of Applied Physics* **32**, 675 (1961).

[23] Childress, J. D. Application of a ferroelectric material in an energy conversion device. *Journal of Applied Physics* **33**, 1793–1798 (1962).

[24] Hunter, S. R. *et al.* Development of MEMS based pyroelectric thermal energy harvesters. In *SPIE Defense, Security, and Sensing*, 80350V–80350V (International Society for Optics and Photonics, 2011).

[25] Pecharsky, V. K. Effect of alloying on the giant magnetocaloric effect of $Gd_5(Si_2Ge_2)$. *Journal of Magnetism and Magnetic Materials* **167**, L179 (1997).

[26] Mischenko, A., Zhang, Q., Scott, J., Whatmore, R. & Mathur, N. Giant electrocaloric effect in thin-film PbZr0. 95Ti0. 05O3. *Science* **311**, 1270–1271 (2006).

[27] Srivastava, V., Song, Y., Bhatti, K. & James, R. D. The Direct Conversion of Heat to Electricity Using Multiferroic Alloys. *Advanced Energy Materials* **1**, 97–104 (2011).

[28] Gschneidner Jr., K. & Pecharsky, V. Magnetocaloric materials. *Annual Review of Materials Science* **30**, 387–429 (2000).

[29] Brück, E., Tegus, O., Thanh, D. C. & Buschow, K. Magnetocaloric refrigeration near room temperature. *Journal of Magnetism and Magnetic Materials* **310**, 2793–2799 (2007).

[30] Fähler, S. *et al.* Caloric effects in ferroic materials: New concepts for cooling. *Advanced Engineering Materials* **14**, 10–19 (2012).

[31] Valant, M. Electrocaloric materials for future solid-state refrigeration technologies. *Progress in Materials Science* **57**, 980–1009 (2012).

[32] Gómez, J. R., Garcia, R. F., Catoira, A. D. M. & Gómez, M. R. Magnetocaloric effect: A review of the thermodynamic cycles in magnetic refrigeration. *Renewable and Sustainable Energy Reviews* **17**, 74–82 (2013).

[33] Liu, J., Gottschall, T., Skokov, K. P., D., J. & Gutfleisch, M. O. Giant magnetocaloric effect driven by structural transitions. *Nature Materials* **11**, 620–626 (2012).

[34] Cui, J. *et al.* Demonstration of high efficiency elastocaloric cooling with large δt using niti wires. *Applied Physics Letters* **101**, 073904–073904 (2012).

[35] Ginell, W. S., McNichols Jr., J. L. & Cory, J. S. Nitinol heat engines for low-grade thermal energy conversion. *Mechanical Engineering* **101**, 28–33 (1979).

[36] Mott, N. F. *Metal-insulator transitions* (Taylor & Francis London, 1990).

[37] Bhatti, K. P., El-Khatib, S., Srivastava, V., James, R. D. & Leighton, C. Small-angle neutron scattering study of magnetic ordering and inhomogeneity across the martensitic phase transformation in $Ni_{50-x}Co_xMn_{40}Sn_{10}$ alloys. *Physical Review B* **85**, 134450 (2012).

[38] Curzon, F. & Ahlborn, B. Efficiency of a carnot engine at maximum power output. *American Journal of Physics* **43**, 22 (1975).

[39] Spaldin, N. A. & Fiebig, M. The renaissance of magnetoelectric multiferroics. *Science* **309**, 391–392 (2005).

[40] Krenke, T. *et al.* Inverse magnetocaloric effect in ferromagnetic Ni-Mn-Sn alloys. *Nature Materials* **4**, 450–454 (2005).

[41] Krenke, T. *et al.* Martensitic transitions and the nature of ferromagnetism in the austenitic and martensitic states of ni-mn-sn alloys. *Physical Review B* **72**, 014412 (2005).

[42] Kainuma, R. *et al.* Magnetic-field-induced shape recovery by reverse phase transformation. *Nature* **439**, 957–960 (2006).

[43] Ramesh, R. & Spaldin, N. A. Multiferroics: progress and prospects in thin films. *Nature Materials* **6**, 21–29 (2007).

[44] Karaca, H. E. *et al.* Magnetic field-induced phase transformation in nimncoin magnetic shape-memory alloys-a new actuation mechanism with large work output. *Advanced Functional Materials* **19**, 983–998 (2009).

[45] Faran, E. & Shilo, D. Twin motion faster than the speed of sound. *Physical Review Letters* **104**, 155501 (2010).

[46] Krulevitch, P. *et al.* Thin film shape memory alloy microactuators. *Microelectromechanical Systems, Journal of* **5**, 270–282 (1996).

[47] Bhattacharya, K., Conti, S., Zanzotto, G. & Zimmer, J. Crystal symmetry and the reversibility of martensitic transformations. *Nature* **428**, 55–59 (2004).

[48] Gall, K. & Maier, H. Cyclic deformation mechanisms in precipitated niti shape memory alloys. *Acta Materialia* **50**, 4643–4657 (2002).

[49] Lim, T. & McDowell, D. Cyclic thermomechanical behavior of a polycrystalline pseudoelastic shape memory alloy. *Journal of the Mechanics and Physics of Solids* **50**, 651–676 (2002).

[50] Moumni, Z., Van Herpen, A. & Riberty, P. Fatigue analysis of shape memory alloys: energy approach. *Smart Materials and Structures* **14**, S287 (2005).

[51] Delville, R. *et al.* Transmission electron microscopy study of phase compatibility in low hysteresis shape memory alloys. *Philosophical Magazine* **90**, 177–195 (2010).

[52] Song, Y., Bhatti, K., Srivastava, V., Leighton, C. & James, R. D. Thermodynamics of energy conversion via first order phase transformation in low hysteresis magnetic materials. *Energy and Environmental Science* **6**, 1315–1327 (2013).

[53] Navid, A., Vanderpool, D., Bah, A. & Pilon, L. Towards optimization of a pyroelectric energy converter for harvesting waste heat. *International Journal of Heat and Mass Transfer* **53**, 4060–4070 (2010).

[54] Glanz, J. Making a Bigger Chill With Magnets. *Science* **78**, 2045 (1998).

[55] Pecharsky, V. K. & Gschneidner, J., K. A. Magnetocaloric effect and magnetic refrigeration. *Journal of Magnetism and Magnetic Materials* **200**, 44–56 (1999).

[56] Pecharsky, V. K. & Gschneidner, J., K. A. Giant magnetocaloric effect in $Gd_5(Si_2Ge_2)$. *Physical Review Letters* **78**, 4497–4497 (1997).

[57] Tegus, O. *et al.* Magnetic-phase transitions and magnetocaloric effects. *Physica B: Condensed Matter* **319**, 174–192 (2002).

[58] Nikitin, S. *et al.* The magnetocaloric effect in $Fe_{49}Rh_{51}$ compound. *Physical Letters A* **148**, 363–366 (1990).

[59] Provenzano, V., Shapiro, A. J. & Shull, R. D. Reduction of hysteresis losses in the magnetic refrigerant $Gd_5Si_2Ge_2$ by the addition of iron. *Nature* **429**, 853–857 (2004).

[60] Maat, S., Thiele, J. U. & Fullerton, E. E. Temperature and field hysteresis of the antiferromagnetic-to-ferromagnetic phase transition in epitaxial FeRh films. *Physical Review B* **72**, 214432 (2005).

[61] Sokolovskiy, V. *et al.* First-principles investigation of chemical and structural disorder in magnetic $Ni_2Mn_{1+x}Sn_{1-x}$ Heusler alloys. *Physical Review B* **86**, 1–11 (2012).

[62] Snyder, G. J. & Ursell, T. S. Thermoelectric Efficiency and Compatibility. *Physical Review Letters* **91**, 148301 (2003).

[63] Snyder, G. J. & Toberer, E. S. Complex thermoelectric materials. *Nature Matererials* **7**, 105–14 (2008).

[64] Poudel, B. *et al.* High-thermoelectric performance of nanostructured bismuth antimony telluride bulk alloys. *Science* **320**, 634 (2008).

[65] Giguere, A. *et al.* Direct measurement of the "giant" adiabatic temperature change in Gd_ {5} Si_ {2} Ge_ {2}. *Physical Review Letters* **83**, 2262–2265 (1999).

[66] Sun, J. R., Hu, F. X. & Shen, B. G. Comment on "direct measurement of the "giant" adiabatic temperature change in $Gd_5Si_2Ge_2$". *Physical Review Letters* **85**, 4191–4191 (2000).

[67] Pecharsky, V., Gschneidner Jr, K., Pecharsky, A. & Tishin, A. Thermodynamics of the magnetocaloric effect. *Physical Review B* **64**, 144406 (2001).

[68] Chambadal, P. *Les Centrales Nuclaires* (Armand Colin, Paris, 1957). (French).

[69] Novikov, I. I. The efficiency of atomic power stations (a review). *Journal of Nuclear Energy (1954)* **7**, 125–128 (1958).

[70] Rubin, M. Optimal configuration of a class of irreversible heat engines. I. *Physical Review A* **19**, 1272–1276 (1979).

[71] de Vos, A. *Endoreversible thermodynamics of solar energy conversion* (Oxford University Press, Oxford and New York, 1992).

[72] Hoffmann, K. H., Burzler, J. M. & Schubert, S. Review article: Endoreversible thermodynamics. *Journal of Non-Equilibrium Thermodynamics* **22**, 311–355 (1997).

[73] Van den Broeck, C. Thermodynamic efficiency at maximum power. *Physical Review Letters* **95**, 2–4 (2005).

[74] Esposito, M., Lindenberg, K. & Van den Broeck, C. Universality of efficiency at maximum power. *Physical Review Letters* **102**, 1–4 (2009).

[75] Berry, R. S., Kazakov, V. A., Sieniutycz, S., Szwast, Z. & Tsirlin, A. M. *Thermodynamics Optimization of Finite-Time Processes* (Wiley, Chichester, 2000).

[76] Hoffmann, K. H., Burzler, J., Fischer, A., Schaller, M. & Schubert, S. Optimal process paths for endoreversible systems. *Journal of Non-Equilibrium Thermodynamics* **28**, 233–268 (2003).

[77] Yan, H. & Guo, H. Efficiency and its bounds for thermal engines at maximum power using Newton's law of cooling. *Physical Review E* **85**, 5–9 (2012).

[78] Khachaturyan, A., Shapiro, S. & Semenovskaya, S. Adaptive phase formation in martensitic transformation. *Physical Review B* **43**, 10832 (1991).

[79] Jin, Y., Wang, Y., Khachaturyan, A., Li, J. & Viehland, D. Conformal miniaturization of domains with low domain-wall energy: Monoclinic ferroelectric states near the morphotropic phase boundaries. *Physical Review Letters* **91**, 197601 (2003).

[80] Kaufmann, S. *et al.* Adaptive modulations of martensites. *Physical Review Letters* **104**, 145702 (2010).

[81] Culity, B. D. & Graham, C. D. *Introduction to Magnetic Materials*. Monographs on selected topics in solid state physics (John Wiley & Sons, Inc., Hoboken, New Jersey, 2009), 2nd edn.

[82] Terman, F. *Radio Engineers' Handbook* (McGraw-Hill, New York, 1943).

[83] Lorenz, L. Über die Fortpflanzung der Elektrizität. *Annalen der Physik* **VII**, 161 – 193 (1879).

[84] Kutateladze, S. S. & Borishanskii, V. M. *A Concise Encyclopedia of Heat Transfer* (Pergamon Press, 1966).